UNIVERSITY OF BERGAMO

School of Doctoral Studies

Doctoral Degree in Technology, Innovation and Management

XXIII Cycle

SSD: ING-IND/14

QUASI-STATIC AND FATIGUE CHARACTERIZATION OF COMPONENTS MADE OF TITANIUM AND ALUMINUM ALLOYS: CONTRIBUTION OF ENVIRONMENTS AND DEPOSITION OF PVD COATINGS

Advisor

Chiar.mo Prof. Sergio Baragetti

Doctoral Thesis

Emanuele Vincenzo Arcieri

Student ID 1020904

Academic year 2019/20

Acknowledgements

Thanks to Prof. S. Baragetti
for his precious teaching and advice.

Thanks to Prof. Z. Bozic, A.K. Vasudevan and Prof. R. Kumar
for their insightful suggestions.

Thanks to the Reviewers, Prof. F.M.H. Aliabadi and Prof. F. Vivio,
for their comments which improve the quality of my thesis.

Thanks to my family and my friends
for encouraging me.

Thanks to all the people who supported me.

Abstract

The favorable strength-to-weight ratio typical of light alloys helps to manufacture lightweight components, which are highly performing and eco-friendly. The lower the weight, the lower the inertia and therefore the lower the fuel and energy consumption. Light alloys are commonly adopted in the aeronautical, naval and racing fields. These engineering sectors are very innovative and for this reason a thorough characterization of light alloys is mandatory. This thesis characterizes two of the most common light alloys, Ti-6Al-4V titanium and 7075 aluminum alloys. The behavior of these alloys under quasi-static and fatigue loads in different environments is described. In addition, the contribution of the deposition of coatings on the fatigue strength of light alloy components is also presented. The poor resistance to corrosion and wear of these alloys can indeed be improved by applying coatings. However, even though these coatings can induce compression on the surface of components, their contribution to fatigue strength is questionable. The entire study also takes into account the presence of damage in the components, evaluating the induced variations in strength. The characterization of these alloys and the study of these coatings will be useful to introduce innovative components characterized by a low mass and a good strength in any environment, under any load, and in the presence of defects, which unfortunately always exist.

In detail, the thesis is divided into three parts: (i) quasi-static characterization of Ti-6Al-4V; (ii) study of the fatigue strength of DLC-coated specimens made of 7075-T6; (iii) study of the influence of damages on uncoated 7075-T6 specimens. The whole study was conducted using experimental tests and numerical models. The combination of these two research approaches allowed to verify the results and to fully understand the behaviors observed.

The first part describes the results of the quasi-static tests conducted on Ti-6Al-4V samples not treated and over-aged. Without this treatment, a reduction in the cost of components could be obtained. Various geometries were tested in inert and harsh environments. The immersion in methanol and the presence of sharp notches induced

dangerous effects, with a notable reduction in the strength. Contamination with moisture reduced the effects of methanol. Crack nucleation was induced at the notches by methanol and steep stress gradients. The analysis revealed the biphasic nature of the alloy, with an intermediate ductile/brittle behavior. The strength of the alloy was affected by stress rate and immersion time in aggressive environments.

The second section of the thesis analyzes the effects of the deposition of these coatings on the fatigue strength of 7075-T6. Rotating bending fatigue tests were used to assess the strength of uncoated and coated specimens. A high scatter of results was detected for the coated specimens, as a consequence of defects in the coating, incomplete adhesion to the substrate or spallation. A finite element model was created to assess the stress state generated by the bending moment. The stresses induced by the moment were combined with the stresses generated by the process of coating deposition. The maximum stress was found under the specimen surface. Consequently, crack initiation is likely to be below the surface of coated specimens if uniform defect distribution is assumed. The cracks nucleated at the surface in uncoated samples.

The third part of the thesis deals with the finite element analyses conducted to assess the stress state generated by the collisions of a steel sphere on 7075-T6 hourglass samples. The impacts tested took place at the minimum cross section of the specimen. Two impacts were simulated: (i) normal; (ii) oblique with a small angle. The impact speed was 100 m/s. The impact angle in the oblique impact was 10°. The outcomes showed that the oblique impact induces higher axial tensile stresses. The specimens were then considered tested with a rotating bending test, bending moment of 1.5 Nm. Adding the axial stresses induced by the impact to the bending stresses helped identify areas where the crack nucleation is likely in the minimum cross section of the sample. These areas lie between the crater generated by the impact and the direction normal to the impact speed (maximum axial stresses) and on the edge of the crater rim (high axial stresses + maximum relative tangential displacements). Overall, the maximum total stresses reached in both normal and oblique impacts are very high, which is why the fatigue life of the specimens is low.

Contents

List of figures

List of tables

1. Introduction

The continuous search for performance in many engineering sectors and the common desire for eco-friendly machines make light alloys very attractive. These materials are in fact characterized by a favorable strength-to-weight ratio, which allows to reduce the overall mass of the system. The lower the weight, the lower the inertia and therefore the lower the fuel or energy consumption. However, the high specific strength must be ensured in different loading conditions and in different environments. For this reason, a thorough characterization of light alloys is necessary. The following lines highlight the great effort of the scientific community to study the behavior of two of the most common light alloys, titanium Ti-6Al-4V and aluminum 7075. Starting from the results in the literature, this thesis aims to improve the knowledge on the behavior of Ti-6Al-4V and 7075 studying their strength in various loading conditions and environments.

The first alloy analyzed in this thesis is Ti-6Al-4V, which is used in the aerospace, automotive and naval sectors [1]. Its biocompatibility and positive interaction with the body environment make this alloy also used in the biomedical sector [2-3]. The superplastic behavior of Ti-6Al-4V is well known [4]. Ti-6Al-4V is generally resistant to a huge spectrum of corrosive environments thanks to the quick creation of a TiO2 surface oxide [5]. Unfortunately, the passivation by this layer can be negatively influenced by its non-adhesion, by the application of loads varying over time and by the interaction with aggressive media [6-8].

Numerous studies on the fatigue behavior of Ti-6Al-4V are available in the literature. Morrisey et al. [9] determined the fatigue strength of Ti-6Al-4V specimens under ultrasonic fatigue load in air environment. The comparison between the results of these tests and the same ones conducted with a frequency of 60 Hz did not reveal any contribution of frequency on the very high cycle fatigue strength. Lanning et al. [10] investigated the influence of stress concentration on the fatigue life of Ti-6Al-4V. Bellows et al. [11] validated the step loading method on smooth specimens, obtaining a high scatter of the results for $R = 0.1$. Peters et al. [12] analyzed the effects induced by Foreign Object Damage (FOD) on the fatigue strength of a Ti-6Al-4V turbine subjected to high cycle fatigue. Over time, additive manufacturing is becoming a technology of increasing interest because it allows the manufacturing of components with internal voids, with consequent reduction in mass. However, the porosity associated with additive manufacturing dramatically reduces the fatigue life of the Ti-6Al-4V components, as demonstrated by Leuders et al. [13]. A reduction in fatigue strength was also noted by Van Hooreweder et al. [14] for samples produced by selective laser melting. This decrease in performance is attributable to the microstructural anisotropy that the adopted technology induces. As known, the microstructure influences the fatigue strength of materials. Nalla et al. [15] compared the high cycle fatigue behavior of a fine-grained equiaxial bimodal structure and a coarser lamellar structure, obtaining a better performance for the latter. The combination of additive manufacturing and other technologies could be useful in achieving the goal of producing low-weight, high-strength components which can guarantee good performance in any environment and under any type of load. Seifi et al. [16] found that hot isostatic pressing on Ti-6Al-4V specimens produced by electron beam melting can induce fatigue strength generally comparable to that of cast and wrought material. The tensile strain rate influences the strength of the alloy, as underlined by Wojtaszek et al. [17]. Zhou and Chew [18] showed that the higher the strain rate, the higher the strength and the lower the ductility of Ti-6Al-4V in ambient environment. This behavior is due to the modification of the plastic deformation mechanism from dislocation slip to twinning. For low strain rates, the influence of strain rate progressively decreases during plastic strain. On the other hand, it is fairly constant for most plastic deformation for high strain rates.

Regarding the corrosion resistance, although titanium does not suffer Stress Corrosion Cracking (SCC) in saline environments, its alloy can. As it is well known [19-20], SCC does not appear under compressive but under tensile stress states. The reason is that tensile stresses open the crack and allow the substrate to interact with the environment. SCC is typical of alloys which produce a passivation layer, like TiO2 oxide for Ti-6Al-4V. Barella et al. [21] observed that in synthetic seawater SCC appears for very slow strain rates and high sodium chloride concentrations. The authors also pointed out that in order to fully understand the behavior of the alloy in seawater, other aspects should be involved in the experiments, like the existence of natural species, thermal loads and motion. SCC can be modelled with a slip-dissolution mechanism: (i) plastic strain at the tip of the crack locally destroys the oxide; (ii) a small part of the substrate is now exposed to the environment; (iii) the exposed part of the metal acts as the anode, the oxide as the cathode; (iv) as a result of the circulation of current generated, the material little by little dissolves. Therefore, the fundamental parameters from a SCC point of view are strain rate, repassivation rate and combination of material and environment [22-23].

Methanol is one of the most aggressive environments for Ti-6Al-4V, as demonstrated by Johnston et al. [24] and Johnson et al. [25] in their studies on the Apollo pressurized fuel tanks. Johnston et al. [24] highlighted the susceptibility to SCC reached by Ti-6Al-4V after solution treatment and aging in the presence of notches. However, Johnston et al. [24] state that even 1% of moisture or cathodic protection can inhibit SCC. The aggressiveness of methanol can be enhanced by the addition of hydrochloric acid, as noted by Sanderson et al. [26]. Dawson and Pelloux [27] identified three trends for crack propagation in Ti-6Al-4V depending on the environment: in air or in vacuum and in media with corrosion inhibitors, crack propagation does not depend on the frequency of the applied load; in methanol the higher the frequency, the lower the propagation rate because the time between two successive peaks of load and the consequent time for corrosion attacks is reduced; in saline and potassium bromide solutions the crack propagation reverses its trend for a determined value of stress intensity factor range as a consequence of the combined action of repassivation process and frequency. Dawson and Pelloux [27] also pointed out the effects induced by the shape of the applied load on the fatigue strength: sine-wave loads are preferable from the point of view of corrosion fatigue compared to rectangular ones because, in the first case, time for corrosion attacks is lower. The preparation of the material and the treatment adopted for surface passivation influence the corrosion performance of Ti-6Al-4V. For instance, in Hank's ethylene diamine tetra-acetic solution, the oxide generated by heat treatment in air is very protective. Brazing induces better corrosion resistance than as-polished condition in the case of acid-passivation or water-aging surface treatments [28]. The crack size influences the corrosion fatigue behavior of the materials [29]. When short cracks propagate, the size of the plastic zone near the tips is generally similar to the length of the defect. Thus, linear elastic fracture mechanics cannot be useful for describing the behavior and an elastic-plastic approach is needed. Wang et al. [30] proposed a model that uses an elastic-plastic approach and considers the Kitagawa effect, i.e. the cyclic stress range influences the short crack propagation rate. This model was successfully applied to short fatigue crack propagation in Ti-6Al-4V.

Ti-6Al-4V is characterized by high coefficient of friction and low wear resistance. The deposition of coatings on Ti-6Al-4V substrates previously treated by oxygen plasma [31], nitrogen plasma [32], micro-arc oxidation [33] and nitriding [34] can improve the tribological properties. Ti-6Al-4V is susceptible to fretting corrosion. If an implant becomes loose, the protective oxide can be torn by the movement of the bone or debris. Implantation of iridium could prevent corrosion [35]. Above 650°C, Ti-6Al-4V subjected to solution treatment and aging and following annealing produces a surface oxide which is porous and marginally adherent. As a consequence of the formation of this layer, the alloy exhibits bad corrosion and erosion performance in air environment [36].

The chemical and mechanical driving forces involved in the corrosion fatigue process on Ti-6Al-4V were identified in the last years by the research group of the Structural Mechanics Laboratory (SMLab) of the University of Bergamo, headed by Prof. Sergio Baragetti [37-41]. The author of this thesis has been part of this research group for three years. This PhD thesis is a continuation of this activity, which is summarized here for this reason. The contribution of variable loads was separated from that of the environment by performing SCC and fatigue tests and comparing the results obtained. The alloy was tested in the classic Solution Treatment and Over-Aging (STOA) condition, i.e. after a 1 hour solution treatment at 925°C and subsequent over-aging induced with a 2 hours vacuum annealing at 700°C. Crack initiation and propagation were studied with the help of the replica method: small strips of acetate softened in acetone were placed on the surface of the specimen in correspondence of the crack every predetermined number of cycles, with an increase in the frequency of application of the strips after crack nucleation. During application, the acetate penetrates the crack and reproduces its geometry. In this experimental campaign, various environments were tested: ambient air, paraffin oil, beeswax, 3.5% wt. salt-water solution and methanol at different concentrations by weight. Air, paraffin oil and beeswax were used to study the behavior of the alloy in inert environments. The results in terms of fatigue life in inert environments are almost the same, with a better performance obtained by the paraffin oil in case of severe notches. Based on the results, the saline solution tested, which simulates marine conditions, is responsible for an approximately 20% reduction in fatigue strength compared to ambient air. This reduction is due to the higher crack propagation rate measured. Microscopic observations show that the higher the stress concentration, the smoother the surface. This behavior can be explained as follows: (i) high stress concentrations induce high stresses on the notch tip but small stress gradients distant from the notch; (ii) stress gradients are responsible for crack propagation; (iii) therefore, small gradients induce low crack propagation rates. The high propagation rate mitigates the action of the environment. Tests in air, paraffin oil and saline solution showed the existence of a threshold of the stress concentration factor (K_t): log (K_t) = 8-9. For K_t values higher than this threshold, the stress at failure is constant. A similar result was also found by Frost and Dugdale [42] for mild steel. In this case the threshold found is log (K_t) = 3-4. The difference in the threshold value can be due to a higher crack propagation rate in Ti-6Al-4V than in steel [39]. As stated in the previous lines, Ti-6Al-4V loses its interesting mechanical properties when it comes into contact with methanol. This substance is part of the fuel of aircrafts and rockets and is responsible for the damage of the tanks [24-25]. Part of the characterization of the Ti-6Al-4V behavior in methanol has been already performed by the SMLab research group. Methanol was found to be aggressive even for small concentrations: 5% methanol induces a 24% reduction in fatigue strength. For 25% the reduction is 36%, for 50% it is 45% and for 95% it is 56%. High concentrations of methanol can be associated with high probabilities of corrosion of the component/specimen and for this reason the higher the concentration of methanol, the lower the scatter of results. The tests described take into account both the environment, which represents the chemical driving force, and the variable load, which represents the mechanical driving force. For this reason, the Ti-6Al-4V samples were tested quasi-statically at different concentrations of methanol. The contribution of methanol on mechanical properties is only detectable for methanol concentrations above 90%, with a maximum reduction of 25% obtained in correspondence with commercially pure methanol. Therefore, variable loads and high concentrations of methanol are detrimental to the performance of Ti-6Al-4V.

In addition to titanium alloys, aluminum alloys are used in high performance sectors. Indeed, aluminum alloys are commonly used in aerospace, marine and automotive applications [43-46]. 7075 is one of the most common Aluminum-Zinc alloys. It exhibits adequate machinability, high fracture toughness, low fatigue crack growth rate and the greatest strength of any aluminum compound [47-50]. It is commonly subjected to T6 temper, which consists in solution and artificial aging. This treatment is helpful for increasing the strength of the material thanks to the induced grain refinement, precipitation hardening and dislocation hardening [51]. In 7075, cracks can nucleate at inclusions or intermetallic phases located close to the surface [52-54]. In 7000 aluminum alloys, iron and silicon are the typical impurities which can form inclusions that affect fracture toughness and fatigue behavior [55]. 7075 is also sensitive to corrosion degradation [6, 56-58]. The combination of varying stresses and harsh environments is detrimental to this alloy. In severe media, cracks initiate at the corrosion pits [59]. A possible solution to prevent corrosion of the alloy could be anodization or deposition of surface layers, which also helps to increase hardness and improve wear resistance. These processes can worsen the fatigue strength of the alloy because they introduce flaws, which may be possible crack nucleation sites, as in the case of sulfuric acid anodizing which reduces the fatigue strength of 7075-T73 by 60% [60]. The changes in the corrosion fatigue behavior of aluminum alloys induced by coatings deposited with Physical Vapor Deposition (PVD) technique are described in the literature [61-65]. In some cases, a post-deposition heat treatment is recommended to rebuild the strength [66]. In TiN films deposited on aluminum, there may be voids and pinholes which can induce corrosion and increase the roughness of the base material [67-70]. In addition, TiN coatings oxidize at high temperatures, reducing the surface hardness [71]. PVD and cathodic cage plasma nitriding increase surface hardness and wear resistance [72].

A decrease in the temperature process can improve the wear resistance of the alloy without greatly influencing the material properties of the substrate. The temperatures reached during the deposition of Diamond-Like Carbon (DLC) coatings, for instance, are low. This coating exhibits a high modulus of elasticity, extraordinary hardness, high corrosion and wear resistance, good semiconductor properties, and the ability to stick to a wide range of materials. These properties make the DLC coating commonly deposited on tools and other machine elements [73-80]. DLC layers can be created with various techniques: for instance, magnetron sputtering [81], filtered cathodic vacuum arc [82], laser ablation [83], plasma beam source [84], plasma enhanced chemical vapor deposition [85] and chemical vapor deposition. The last one is common, although the process temperatures during PVD are generally lower than those of chemical vapor deposition. Substrate modifications are therefore different [86-88]. DLC is a metastable structure of amorphous carbon with sp2 and sp3 bonding and various amounts of hydrogen, which is adsorbed. Its mechanical and tribological properties are influenced by the chemical composition, i.e. sp2-to-sp3 bonding ratio and hydrogen and dopant content [75-76, 89-94]. For instance, hydrogen can decrease the outstanding adhesion between diamond surfaces and aluminum [95] and titanium, chromium and tungsten improve it [96-97]. High temperatures reduce the mechanical properties of DLC films [98-99]. By applying DLC coatings, it is possible to improve the tribocorrosion performance of a component immersed in aggressive environments containing water [100-103]. When applying DLC coatings, a multilayer architecture should be preferred in order to limit the action of the defects induced by the deposition of the coating [104-107]. Applying a suitable multilayer DLC film can increase the corrosion resistance and tribological properties of plasma nitrided steel. The inclusion of pure chromium layers increases the fatigue life [108]. Regarding the fatigue behavior, DLC coatings were found to induce a residual surface compression, of the order of 1 GPa, which is favorable from a fatigue point of view [109]. For example, for carbon coated austenitic steel, a huge improvement in resistance to cyclic loading at small strain amplitudes was observed [110]. The residual stresses are induced by a mismatch of the coefficient of thermal expansion, a structural mismatch and a mismatch of the modulus of elasticity between the substrate and the coating [111]. However, the residual compressive stresses introduced on the surface may not be sufficient to increase the fatigue life of the components on which the coatings are deposited. A study on the fatigue strength induced by the deposition of a DLC coating is required and is the second goal of this thesis.

The strength of a omponent must be ensured in the presence of defects. As it is known, all structural components exhibit defects which may propagate due to accidental loads, overloads or aggressive environments. For this reason, the characterization of the materials should also include the behavior in the presence of flaws. Defects can be induced by technological processes, but also by the impact of objects. In the aviation industry, FOD indicates the damage related to the collision of particles on parts of the aircraft engine. These particles can enter the engine during takeoff, taxiing and landing and they are typically debris and sand. In the literature, a huge quantity of studies on FOD on components made of titanium and not of aluminum is present, as shown in the following lines. For this reason, this thesis aims to investigate the strength of 7075 specimens affected by FOD. The impact can cause nicks, scratches and craters that can alter the fatigue behavior of the components [112-113]. Regarding the fatigue behavior, fundamentally three variables influence life: (i) the generation of microcracks and microstructural damages; (ii) the introduction of stress concentrations; (iii) the introduction of residual stress fields.

Frequently the fatigue strength of components after FOD is influenced by the microscale structure. According to Peters and Ritchie [114] , the microstructural damage depends on the impact speed. High speed collisions, i.e. impact speeds of 300 m/s, induce material pile-up at the crater rim. The material plastic flow makes micronotches and microcracks appear. These defects influence fatigue strength. On the other hand, low speed impacts induce effects which are less appreciable. Therefore, even a quasi-static approach can only be adopted in the latter case, while dynamic models are needed for collisions at high speeds. The shape of the impacting particle affects the shape of the crater. Ding et al. [115] analyzed the collision of a cube made of hardened steel on a flat sample made of Ti-6Al-4V. An edge of the cube was the first part to impact the sample. The indented area was observed with a scanning electron microscope which revealed rounded corners and irregular sides for the indent instead of the expected V shape. The irregularities observed are due to a combined effect of deformation experienced by the cube and the relaxation of Ti-6Al-4V. FOD can induce Loss of Material (LOM). According to Martinez et al. [116], the generation of sharp edges, the folding, and maybe the relief of compressive stresses associated with LOM are actually responsible for a reduction in fatigue strength. In addition, LOM creates sites for crack initiation [116]. The notches and craters generated by FOD induce local stress concentrations which are unfavorable from a fatigue point of view. Chen [117] studied the residual stress field produced by the impact of a particle on the leading edge of a turbine blade. The study was performed with the aid of a numerical model. In detail, he simulated the impact of a rigid sphere on the edge of a plate in the normal direction. The plate was characterized by a rectangular cross section. Its thickness was much smaller than the other dimensions. An elastic perfectly plastic material behavior was assigned to the plane. The plastic pile-up at the crater rim was considered negligible. According to the results obtained, the depth of the crater mainly affects the stress concentration. The greater the penetration, the greater the stress concentration at the base of the crater. At this point, the K_t found by Chen [117] was always greater than 1. Consequently, the stress concentration is primarily the driving force for crack initiation in this area. At the bulge tip, the K_t found decreased and it was less than 1. Responsible for this is the expansion of the material in the lateral direction, which releases the stress. For this reason, the crack nucleation at the bulge tip can be induced by factors other than the stress concentration.

Finite Element (FE) analyzes are commonly used to assess FOD-induced stresses, although they provide overestimated values [118]. The reasons for this overestimation can be traced to the lack of implementation of some material properties. For example, the models do not consider the nucleation of microcracks and the generation of shear bands, which are typical of impact problems. In addition, FE models rarely take creep effects into account at room temperature which can be responsible for reducing stress. Finally, the material models implemented adopt extrapolated and non-validated data. Often the implemented properties refer to the static behavior, as the literature does not present an adequate collection of experimental data at high strain rates.

The residual stresses induced by the collision of a steel ball against a flat sample of Ti-6Al-4V were evaluated by FE analysis in [119]. The state of the residual stresses in the circumferential direction highlights a large compression region directly under the crater generated by the impact. Two regions of residual tensile stresses can be identified. The first, small but intense, is located on the edge of the crater; the other, more extended, is placed at a distance equal to about one radius of the crater from the surface of the crater itself. If the residual stresses are compressive, they can prevent nucleation of fatigue cracks. Comparison of the fatigue strength of Ti-6Al-4V plates subjected to FOD and of the same plates subjected to FOD and subsequent stress relief show that post-treatment can degrade component performance under cyclic loading. The reason may be the cancellation of the compressive stresses beneath the crater, which prevent the propagation of the cracks. The stress relief treatment can be ineffective with respect to the fatigue in the case of impacts involving high energy exchanges, for example the impact of 2 mm spheres fired at a speed of 305 m/s [120]. This huge amount of impact energy can cause fractures in the sample resulting in LOM. The plastic strain produced in these cases are negligible and for this reason the induced residual stresses are very low. In other cases, stress relief is helpful in removing FOD-induced tensile stresses, resulting in a noticeable improvement in fatigue life.

This thesis aims at amplifying the characterization of Ti-6Al-4V and 7075 regarding the aspects mentioned above. This characterization is useful for introducing components that combine light masses with high sustainability and appreciable performance in any environment, under any load, and in the presence of defects, that always exist. These needs are typical of the nautical, racing and aeronautical sectors but can affect all sectors of mechanics. The thesis is divided into three parts: (i) quasi-static characterization of Ti-6Al-4V; (ii) study of the fatigue strength of DLC-coated specimens made of 7075-T6; (iii) study of the influence of FOD on uncoated 7075-T6 specimens. For each part, the materials and methods applied, the results obtained and some remarks are reported.

Chapter 0 deals with the part (i) of the work. The thesis provides a quasi-static characterization of Ti-6Al-4V not subjected to STOA, considering different environments and stress concentrations induced by different notch geometries. Notch-induced stress concentrations are evaluated using FE modeling. Samples without STOA are studied because the lack of this treatment could reduce the manufacturing cost of the components. The analysis of the fracture surfaces of the tested specimens clarifies the failure mechanism.

Afterwards, the experimental test campaign on some specimens coated with DLC by PVD is presented in the part (ii), Chapter 3. Coatings are able to improve tribological properties and corrosion resistance. This campaign aims at determining the contribution of the coating deposition of the fatigue strength of aluminum components. The tests were carried out in air environment with a rotating bending load. The fatigue strength was determined at various number of cycles within the range of $2 \cdot 10^5$-10^7. The results obtained with the DLC-coated samples were compared with those obtained with uncoated specimens. The fracture surface and the stress analyses were adopted to investigate the specimen failure mechanism. In detail, the stress analysis was performed by adding the residual stresses induced by the deposition of the coating with those induced by the bending moment. The results helped determine the sites of crack initiation.

As 7075-T6 is popular in aerospace and aeronautical sectors, components made of this alloy can be subject to FOD. This thesis describes in part (iii), Chapter 4, a preliminary FE model created to assess the stress distribution in a 7075-T6 hourglass specimen that is tested with a rotating bending fatigue load after being subject to FOD. Two different damages were investigated: the first one was induced by the normal impact of a steel sphere, the other by an oblique impact with a small angle of the same sphere. Both damages are in correspondence of the minimum cross section. The stresses induced by the impacts were superposed with the stresses induced by the fatigue test. This method allows to identify the regions unfavorable from a fatigue point of view, at which crack nucleation is expected, if a uniform defect distribution is assumed.

2. Quasi-static tests on Ti-6Al-4V

The following paragraphs describe the experiments carried out with the aim of evaluating the strength of Ti-6Al-4V not subjected to STOA under static loads. Characterization was performed in various environments, inert and aggressive. The work was presented in various conferences [121-122] and described in several papers [123-126].

2.1. Materials and methods

The tested samples were obtained from a Ti-6Al-4V raw plate supply. The alloy was not subjected to STOA. If this treatment was not carried out, the total cost of the mechanical component would be reduced. For this reason, it is necessary to determine the strength of the alloy in this condition. The mechanical properties of Ti-6Al-4V without and with STOA are shown in Table 1 [123].

Table 1 Mechanical properties of Ti-6Al-4V without and with STOA [123].

STOA	Ultimate Tensile Strength (UTS) [MPa]	Yield Tensile Strength (YS) [MPa]	Young's modulus (E) [MPa]	Elongation at break (A%) [-]
No	1000-1100	958-1050	110000	16
Yes	947-990	900-945		

The combination of environment and stress concentration was analyzed. As regards the corrosion resistance, the tested environments are: air, paraffin oil and methanol. Air and paraffin oil are inert environments, with paraffin oil which was used to study the behavior of the alloy in vacuum conditions. The contribution of stress concentration was assessed using the different sample geometries shown in Figure 1 [123]: smooth (S, Figure 1a), notched (N, Figure 1b) and sharply notched (SN, Figure 1c). As it can be seen, the specimens had a variable cross-section, which was necessary to limit the extent of the area where failure could occur. Generally, the maximum stresses are obtained in the minimum cross section, if there are no defects in the specimen. The extent of the minimum section of the specimen had to be small due to the high strength of the alloy tested. In this way, the failure of the specimen was induced with axial loads which were admissible for the testing equipment adopted, described in the following lines. To get this small area the two fillets present in the geometry were needed. It was not possible to introduce only one fillet because of the difficulty of machining titanium alloys. The high chemical reactivity, the high cutting temperature, the low thermal conductivity, the high strength and the low elastic modulus make titanium alloys difficult to manufacture [127]. The notches placed on the two lateral sides of the specimen N were introduced by Electro Discharge Machining (EDM). The geometry of the SN specimen was created by introducing two further notches, one on each side, on the notches made with EDM. The two further notches were introduced with the aid of a sharp knife. The shape of the notches introduced by EDM and EDM & sharp knife can be seen in Figure 2 [123], where the measured notch radii are shown. Stresses during setup and experimental tests were monitored with the aid of strain gauges, shown in blue in Figure 1, on the front and back of the specimen. The monitoring of the stress field in the specimen also during setup was carried out to avoid the introduction of prestress states. In the case of tests in an aggressive environment, the strain gauges were not positioned in correspondence of the minimum section to avoid contamination. The load applied during the test was measured by a load cell. The values of local K_t for the three geometries tested were determined by linear elastic FE analysis in Abaqus 6.14 [128]. Only a quarter of the longitudinal section of the sample was modeled. The symmetry conditions were implemented on the symmetry planes. The mesh was made up of plane stress elements. A kinematic coupling constraint connected the nodes on the upper edge of the sample. The master point of this constraint was placed on the symmetry plane. An arbitrary load of 100 N was applied to the master point. Due to the symmetry of the problem analyzed, the applied load corresponds to 200 N applied to the whole specimen. The K_t value was calculated using the maximum principal stress σ_I as parameter. The stress distributions near the minimum cross section for the three tested geometries are shown in Figure 3 [125]. In the figure, the stresses are normalized with respect to the nominal stress (expected) in the minimum cross section of the specimen, σ_{nom,min_sect}. Table 2 [123] shows the results obtained.

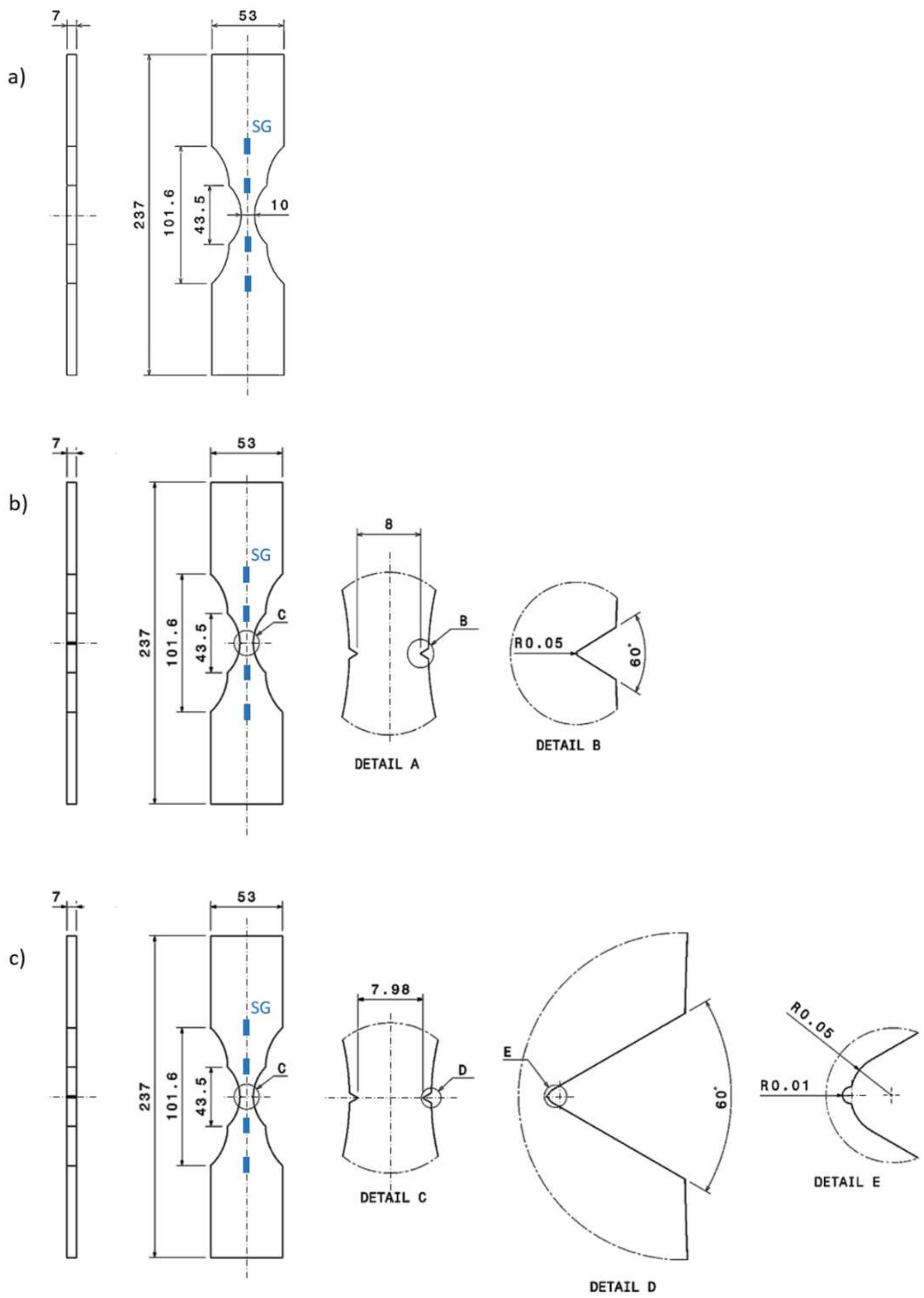

Figure 1 Geometry of the tested specimens (dimensions in mm): a) S, b) N, c) SN [123].

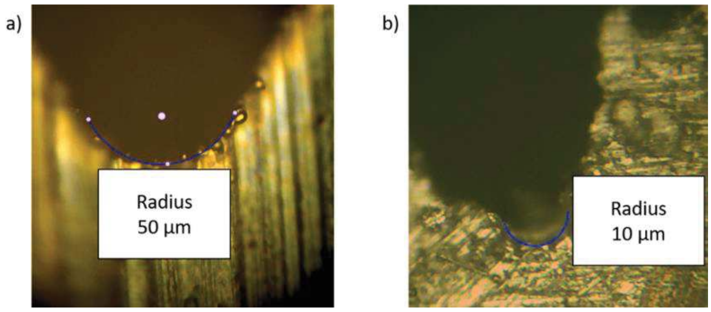

Figure 2 Radius of the notches: a) N, b) SN [123].

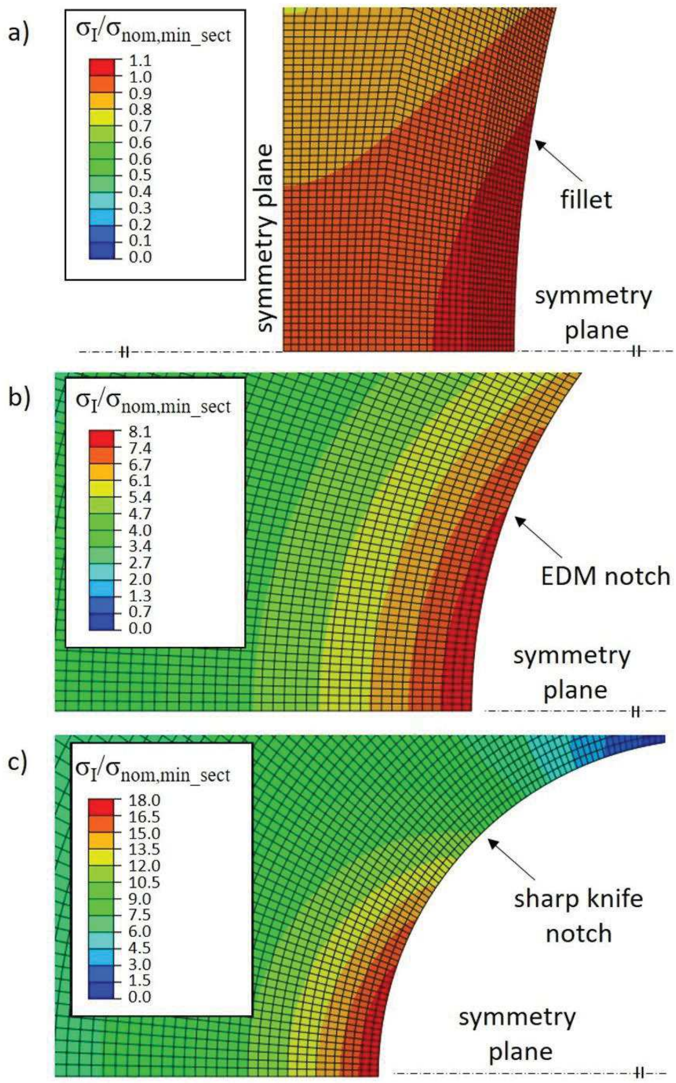

Figure 3 K_t evaluation: a) S; b) N; c) SN [125].

Table 2 K_t for the geometries tested [123].

Geometry	K_t
UN	1.1
N	8.1
SN	18.0

The surface of the central part of the sample was polished with grit paper from 600 to 1200 grit and with 3 µm diamond paste. The area was then cleaned with acetone. Abrasive blasting was performed on the gripping points in order to obtain greater friction between the specimen and the testing machine and to prevent the specimen from sliding. The placed pieces of aluminum tape shown in Figure 4 act as a gasket to enhance this effect [123].

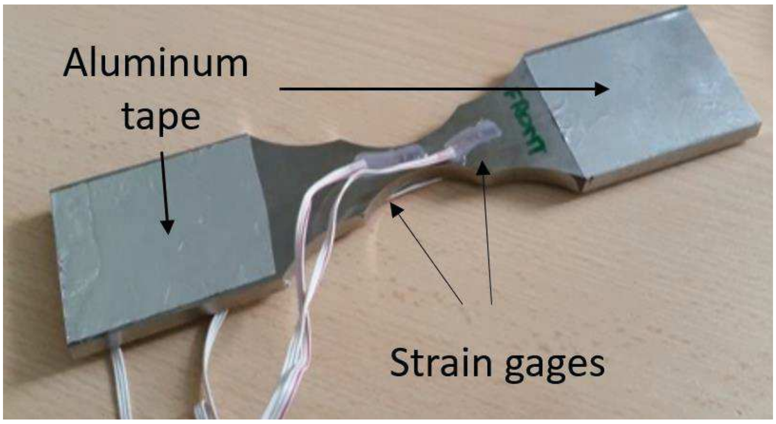

Figure 4 Sample ready to be mounted in the test machine [123].

The specimens were stressed with an axial load. The testing machine adopted for the tests was specially designed in the past by SMLab researchers. It is shown in Figure 5 [123] and consists of a threaded rod tensile system. The two rolling bearing hinge grips avoid parasite bending stresses on the sample during the test. The plate placed behind the specimen is an anti-torsion device which prevents stressing the specimen during setup operations and is removed before the start of the experiments. The testing machine was modified from the one designed in the past. The previous version is shown in Figure 5a, the modified one in Figure 5b. The modified components are marked with a red rectangle in Figure 5a. These modifications allow to test samples with a wider length range. A hydraulic jack applied the load on the specimen.

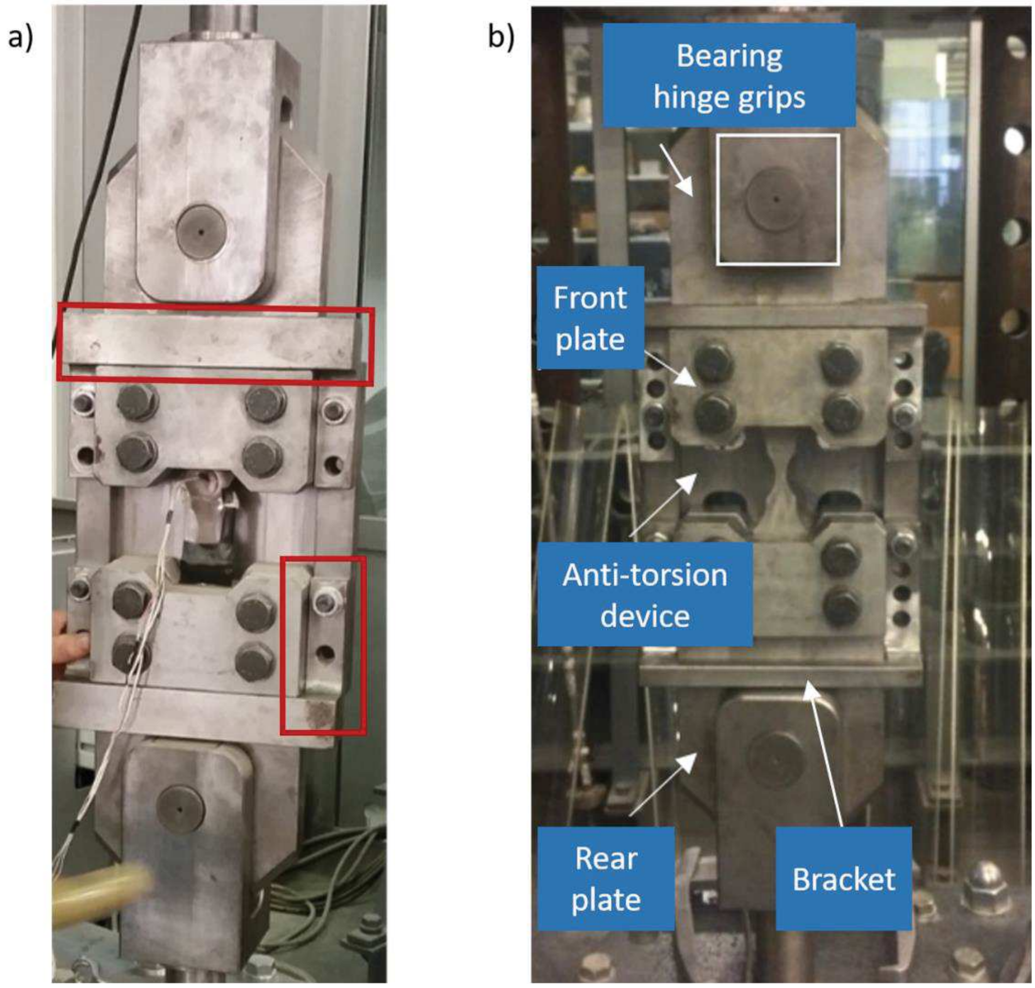

Figure 5 Testing machine for quasi-static tests [123].

The samples were tested with different load histories, described in the Section 2.2. The starting point for each test was far from UTS/K_t, taking also into account the aggressiveness of the environment. The length of the loading steps and the increase in load were influenced by the time available. These tests take very long time. Furthermore, the tests described were performed manually, without automation. For these reasons, some pauses were necessary concurrently with the night closure of the laboratory and other commitments.

Macroscopic fracture surface analysis at various magnification levels was used to investigate the failure mechanism. The analysis was performed using a trinocular 7x-45x zoom stereo microscope ZENITH SZM-4500, an extra lens 2x ST-087 2x for 14x - 90x zoom, a variable double LED illuminator ZENITH CL-31 and a double self-supporting articulated arm. A USB micro-video camera OPTIKAM B-3 was used to take pictures.

2.2. Results

2.2.1. S specimen in air environment

The first experimental test was performed on a S specimen in air to characterize the alloy in an inert environment. The axial stress experienced by the minimum cross section of the specimen over time is shown in Figure 6 [124]. The strain rate adopted for each test is low, as it can be seen in the following figures for each test. The strain rate $\dot{\varepsilon}$ was calculated as reported in Equation 1, where $\Delta\sigma$ is the variation of the axial stress in the minimum cross section, E indicates Young's modulus of the material and Δt is the duration of the step.

$$\dot{\varepsilon} = \frac{\Delta\sigma}{\mathrm{E}\Delta t} \quad (1)$$

The starting load was 600 MPa, the maximum strain rate was $7.26\cdot10^{-7}$ s^{-1}. The failure of the specimen occurred at a stress of 1083 MPa, which is approximately equal to UTS of Ti-6Al-4V without STOA. The failure occurred without appreciable strain of the specimen. The test took 19 hrs 35 mins in total.

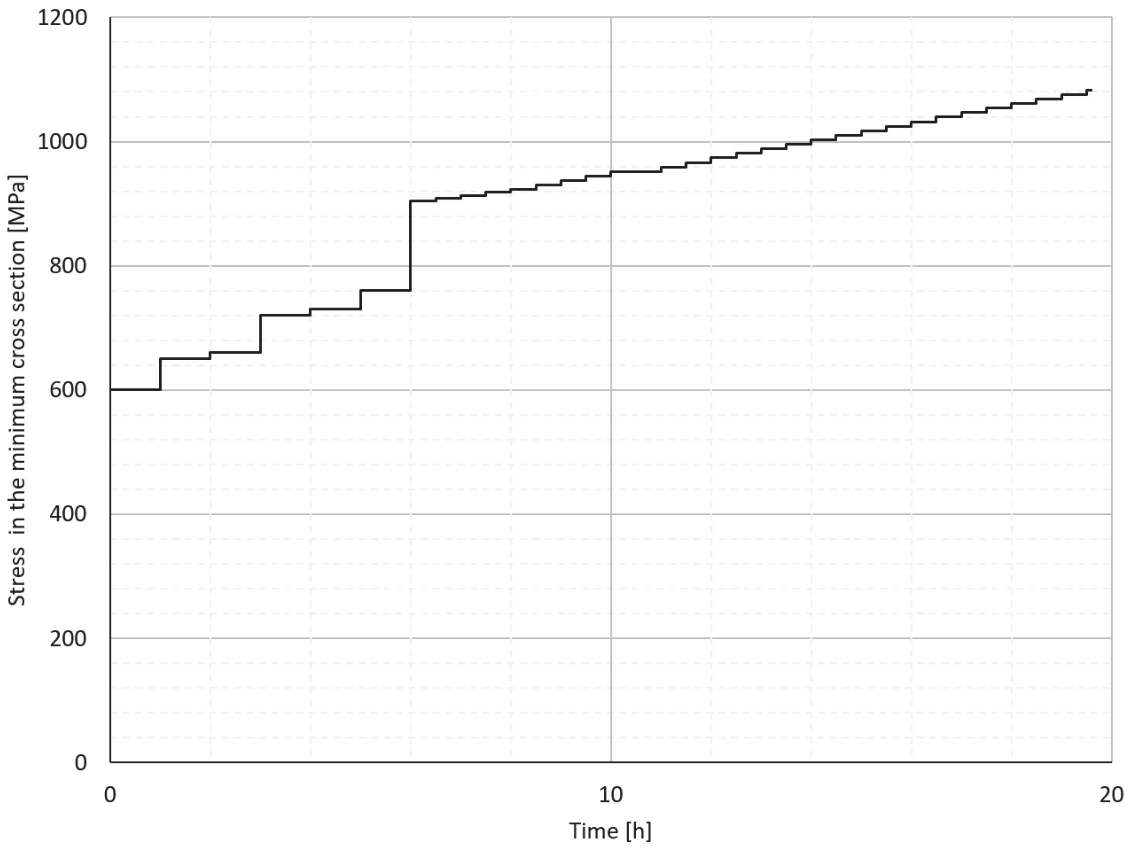

Figure 6 S specimen in air: loading history in the minimum cross section [124].

2.2.2. N specimen in paraffin oil

This second test was performed to evaluate exclusively the possible concentration of the stresses induced by the EDM notch. Paraffin oil was used to investigate the behavior of the alloy under vacuum conditions. A drop of this liquid was placed on the sample at the two notches. The loading history in the minimum cross section is shown in Figure 7 [124]. The starting load was 100 MPa, the maximum strain rate was $3.22 \cdot 10^{-7}\ s^{-1}$. The failure of the specimen occurred at a stress of 1025 MPa, which is approximately equal to UTS of Ti-6Al-4V without STOA. The failure occurred without appreciable strain of the specimen. The test took 40 hrs 30 mins in total. The sample was tested in air environment so corrosion process was very low. Therefore, the environment did not affect the test duration. The longer duration of the test compared to the previous one is due only to the smaller strain rates adopted.

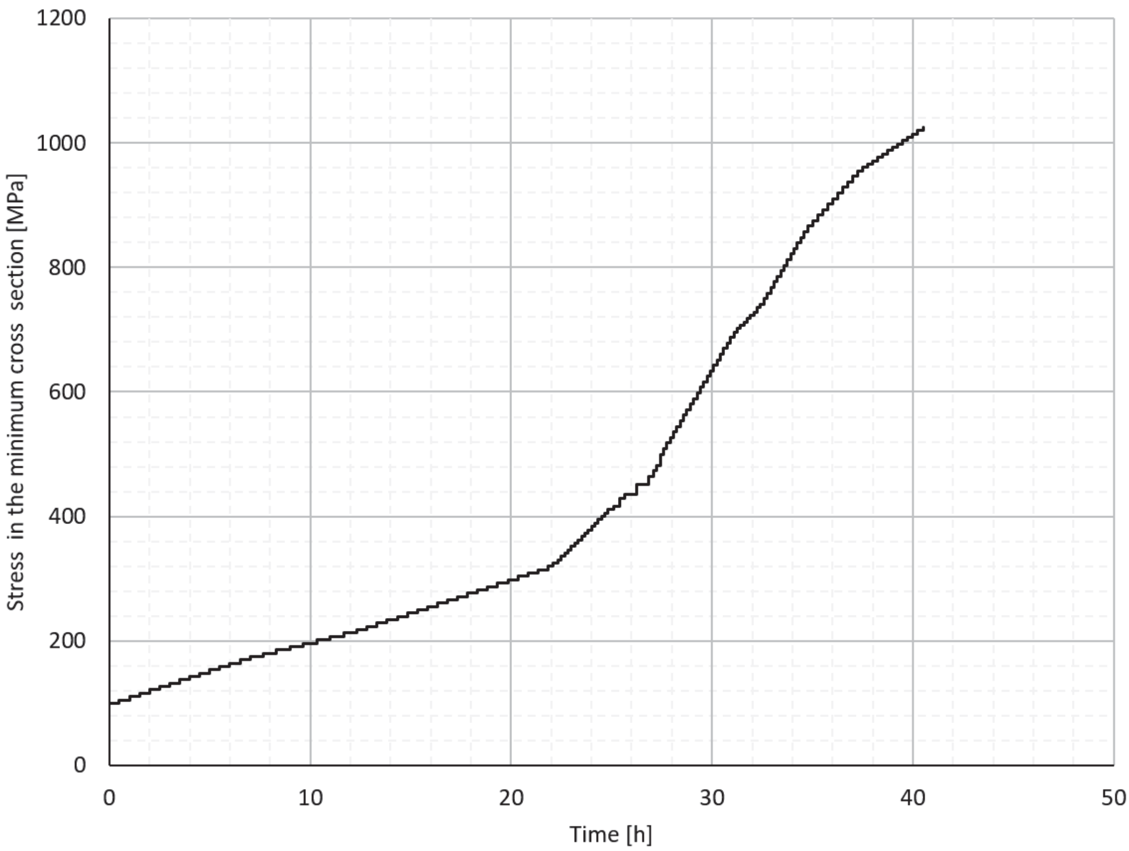

Figure 7 N specimen in paraffin oil: loading history in the minimum cross section [124].

2.2.3. N specimen in methanol

This case studies the behavior of Ti-6Al-4V without STOA in a highly aggressive environment. This test consisted of two steps. In the first one, the methanol was contained in a tank composed of two pieces of polyvinyl chloride. The two parts were coupled by silicone (Silicone I). When an axial stress of 800 MPa was reached, contamination of the methanol with the silicone of the tank was seen. It was thought that this contamination could be responsible for a lower aggressiveness of methanol. For this reason, the tank was changed. In this second tank, the two parts in polyvinyl chloride were connected by bolts. A new kind of sealant not able to interact with methanol (Silicone II) was used. The two tanks adopted in this experimental test are visible in Figure 8 [123]. Figure 8a shows the first tank adopted, Figure 8b the tank used in the second step. The load history and strain rate are shown in Figure 9 [124]. The tank was emptied of methanol every time the test was interrupted in order not to accelerate corrosion. Since its high volatility, the methanol was refilled on restart and topped up when its quantity decreased by an appreciable level. The starting load of the first step was 100 MPa, the maximum strain rate in this step was $9.02 \cdot 10^{-8}$ s^{-1}. The second step started at 400 MPa, the maximum strain rate was less than $2.80 \cdot 10^{-7}$ s^{-1}. Specimen failure occurred when a stress of 689 MPa was reached in the minimum cross section. The failure occurred without appreciable strain of the specimen. The test took a total time of 23 hrs 5 mins.

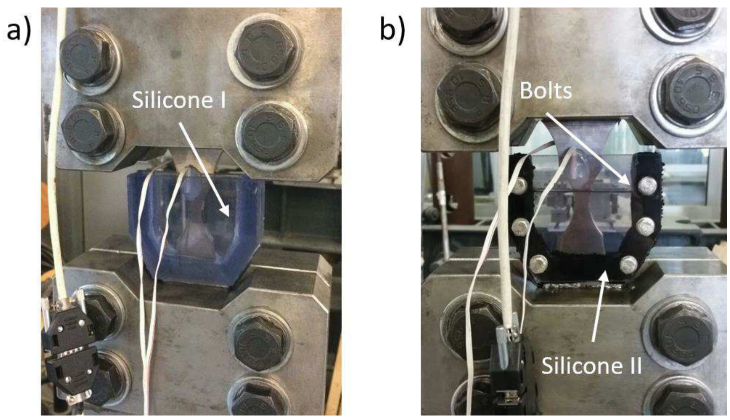

Figure 8 N specimen in methanol: a) tank of the I step; b) tank of the II step [123].

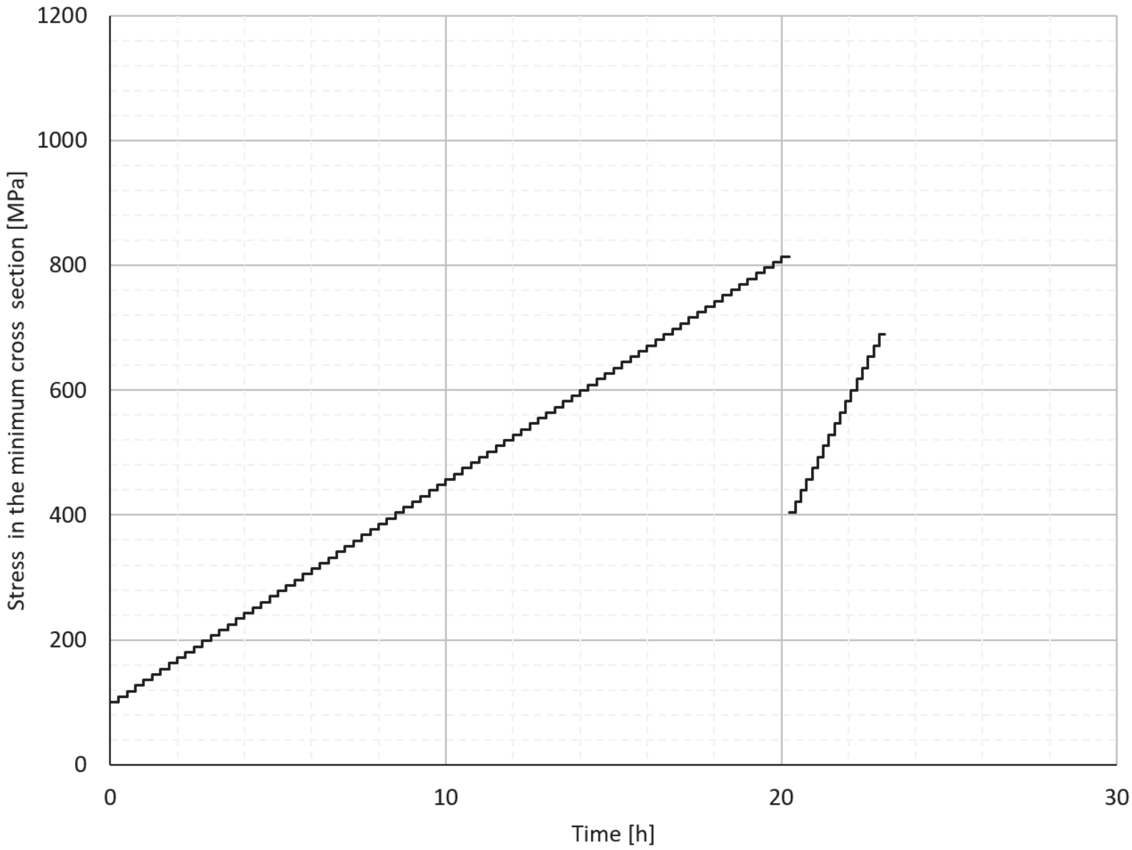

Figure 9 N specimen in methanol: loading history in the minimum cross section [124].

2.2.4. S specimen in methanol

During the test of the S specimen in methanol, the fluid was topped up. The methanol was left in the tank during stops of the experiment. During the stops, the specimen was subject to a very small load, corresponding to 10 MPa in the minimum cross section. Figure 10 [124] summarizes the applied load and the strain rate. The starting load was 100 MPa, the maximum strain rate was $2.89 \cdot 10^{-7}$ s^{-1}. The failure of the specimen occurred at a stress of 1042 MPa, which is approximately equal to UTS of Ti-6Al-4V without STOA. The failure occurred without appreciable strain of the specimen. The test took 73 hrs 45 mins in total.

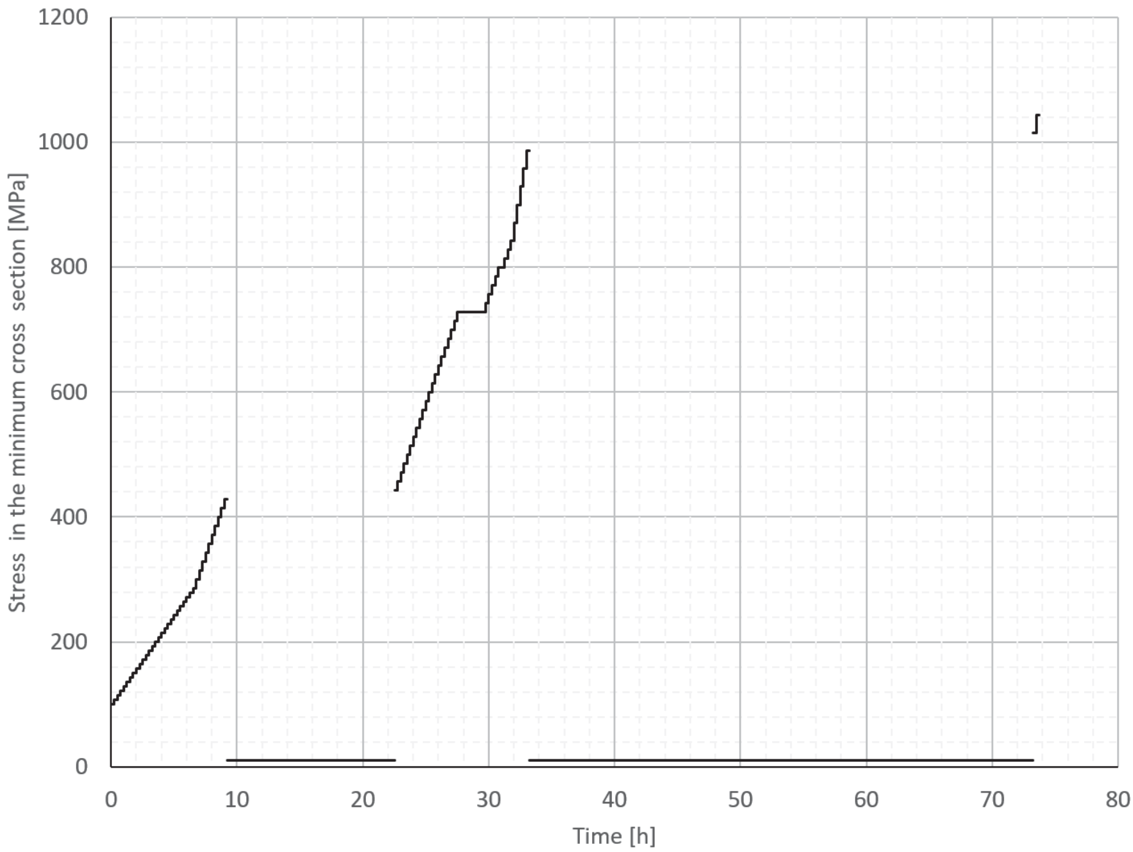

Figure 10 S specimen in methanol: loading history in the minimum cross section [124].

2.2.5. SN specimen in methanol

A fully sealed tank was adopted for the test of the SN specimen in methanol. The tank was also filled completely with methanol to roughly cancel the humidity in the tank. As indicated by Johnston et al. [24], moisture could contaminate the solution and reduce the aggressiveness of methanol. With the new experimental setup, the external environment could not influence the results. Figure 11 [124] reports the loading history. The starting load was 300 MPa, applied after a few minutes of immersion in methanol. The maximum strain rate was $1.59 \cdot 10^{-7}$ s^{-1}. In the last load block, an axial stress of 345 MPa was applied to the minimum cross section. The last step should have taken 1 hr 15 mins. However, after this time the load read by the load cell was 0 N. It was tried to increase the stress but immediately the sample failed. The test took 2 hrs 20 mins in total.

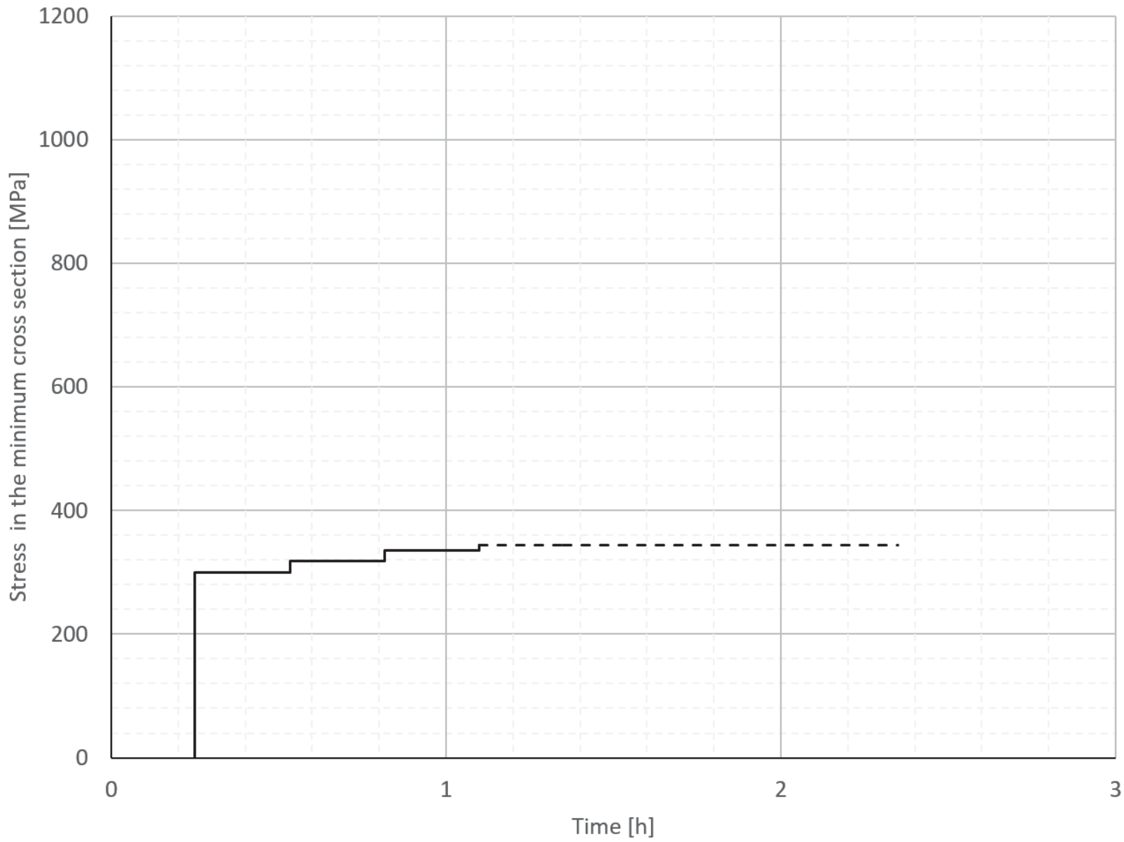

Figure 11 SN specimen in methanol: loading history in the minimum cross section [124].

2.2.6. N specimen in methanol (further test)

This section describes a further test conducted on a N sample immersed in methanol. The aim is to compare previous results and to better understand the influence of strain rate, immersion time and moisture contamination. The results of the previous tests suggested that the time the sample is immersed in methanol affects alloy strength. The reason for this behavior is that a longer immersion time is associated with a greater likelihood of corrosion attacks and a longer duration of the corrosion process itself. Furthermore, methanol appears to become less aggressive in the presence of contamination from air humidity or other chemical substances, such as the constituents of the sealant used to connect the two parts of the tank. Strain rate is also an important parameter, as described in the literature. The failure of the test described in 2.2.5 of the SN specimen in methanol occurred at low strain rate. This could confirm the preliminary considerations made. In this experiment, the tank was completely filled and sealed. The stress and the strain rate in the minimum cross section of the sample are shown in Figure 12 [124]. Each load block generally took 15 mins. The 520 MPa load block took 14 hrs and 20 mins and corresponds to the immersion of the central part of the specimen overnight. The load actually read the next morning was 440 MPa. The 720 MPa load block took 35 mins and the 760 MPa load block took 2 hrs and 30 mins. These variations in the duration of the load blocks are due to concurrent commitments of the author of the thesis. After these 2 hrs 30 mins, the sample failed. Therefore, the specimen failed at a load corresponding to 760 MPa in the minimum cross section after a total time of 31 hrs. The maximum strain rate in the test was $1.01 \cdot 10^{-7}$ s^{-1}. The stress to failure is comparable to that obtained with the other N specimen in methanol, described in 2.2.3. The time to failure is longer. The reason for this discrepancy could be that the test tank described in 2.2.3 was modified during the experiment. During the time it took to change the tank, the specimen was not cleaned. For this reason, the specimen and in particular the notches could have been in contact with a layer of methanol which carried on the corrosion process. Unfortunately, the time required to change the tank was not measured and only qualitative considerations can be made on the time to failure. Finally, the specimen failed in a very long loading block.

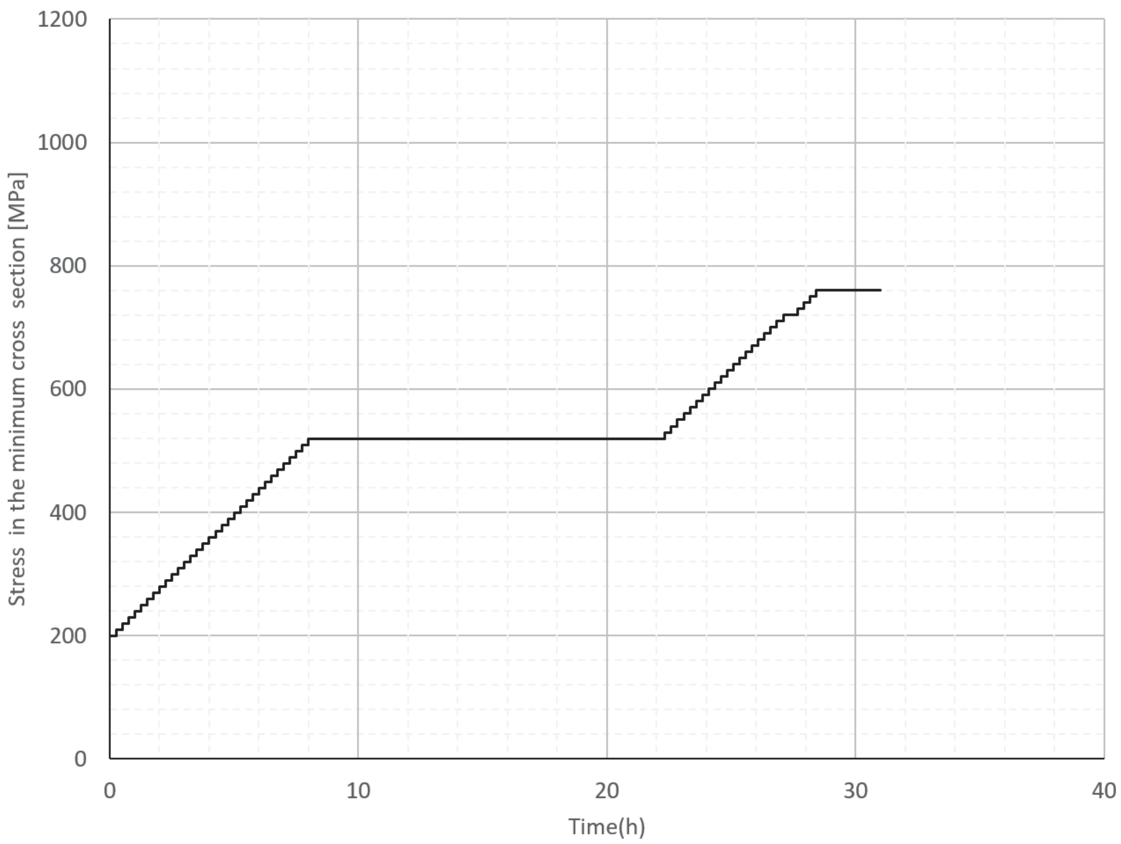

Figure 12 N specimen in methanol: loading history in the minimum cross section [124].

2.3. Analysis of the fracture surfaces

The fracture surface of the S specimen tested in air environment (Figure 13, [125]) is wavy and shows teared edges (Figure 13a) and small deep cracks (Figure 13b). Figure 14 [125] refers to the N specimen in paraffin oil. It shows short lines of metallic color in some areas. They could be evidence of the biphasic nature of the Ti-6Al-4V alloy. The small dimples found indicate the presence of a ductile phase. The manner in which the failure occurred and the fracture surface obtained indicate the intermediate ductile/brittle behavior of the alloy. Figure 15 [125] shows the fracture surface of the N specimen tested in methanol. The cracks initiated at the notches (Figure 15a), where the stresses were highly concentrated. The very steep stress gradient near the notches favored crack propagation. Furthermore, the aggressiveness of the environment could have stimulated the nucleation of cracks. The final surface looks like an asymmetric hourglass (Figure 15b). The geometry of the deformed section reveals that necking occurred. The separation at the notches (Figure 15c) and the sliding in the other areas of the section (Figure 15d) made the specimen fail. In Figure 16 [125] the surface of the S specimen in methanol can be seen. The methanol attacks the edges of the specimen (Figure 16a). A brittle surface can be seen in the proximity of the edges (Figure 16b). The fracture surface of the SN specimen tested in methanol (Figure 17) shows many lacerations, which are parallel to the longest side of the section. The coalescence of these lacerations may have caused the specimen failure, which occurred silently when it was tried to increase the load on the specimen. The lacerations reduced the resistant area and induced stress concentrations which were responsible for sample failure at very small load. The fracture surface of the additional N specimen tested in methanol was also observed (Figure 18, [126]). The surface morphology is similar to that of the first sample tested in methanol (Figure 15): it has an hourglass shape (Figure 18a) generated by the necking, the crack nucleation sites are in correspondence with the notches (Figure 18b) and it is possible to clearly identify failure areas by sliding and by separation (Figure 18a and Figure 18c respectively).

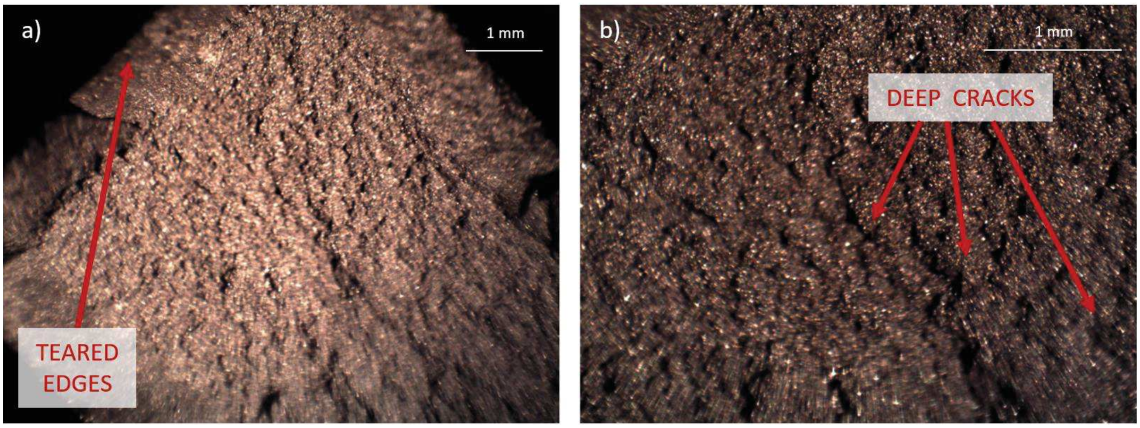

Figure 13 Fracture surface of S specimen in air environment: a) teared edges; b) deep cracks [125].

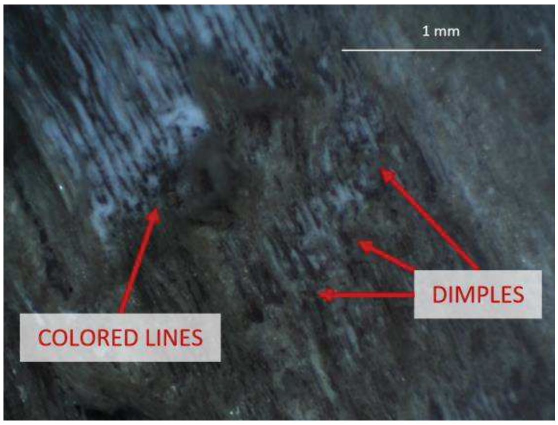

Figure 14 Fracture surface of N specimen in paraffin oil [125].

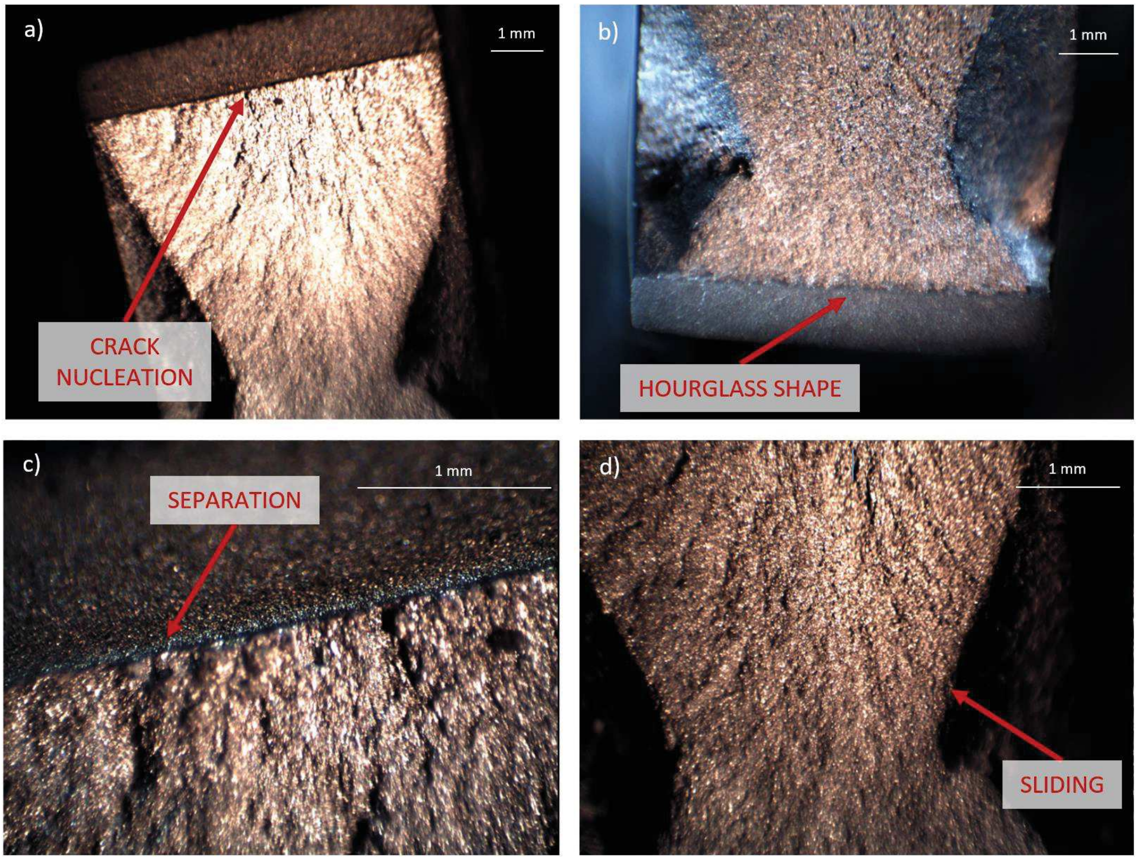

Figure 15 Fracture surface of N specimen in methanol: a) crack nucleation; b) hourglass shape; c) separation at notches; d) sliding in other regions [125].

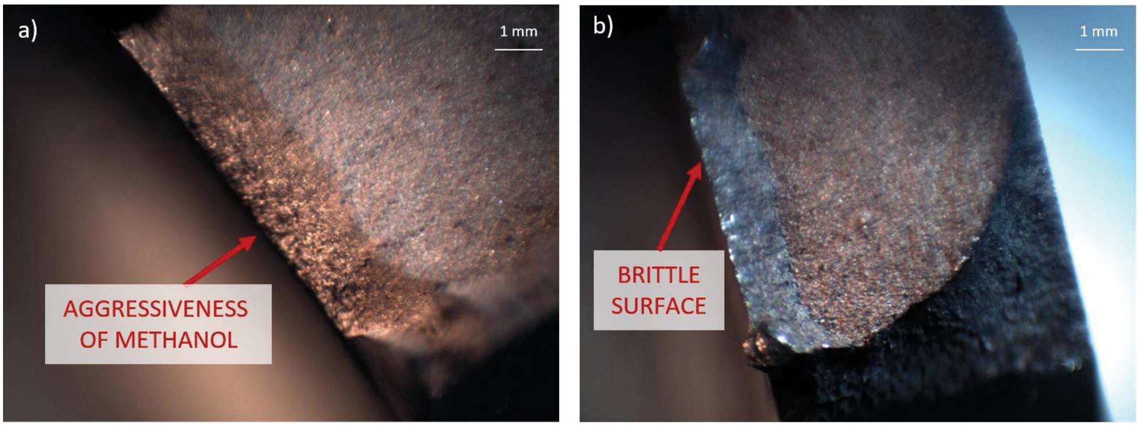

Figure 16 Fracture surface of S specimen in methanol: a) aggressiveness of methanol; b) brittle surface [125].

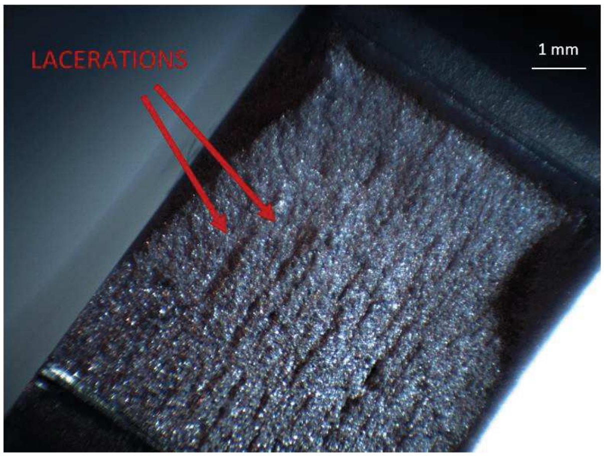

Figure 17 Fracture surface of SN specimen in methanol [125].

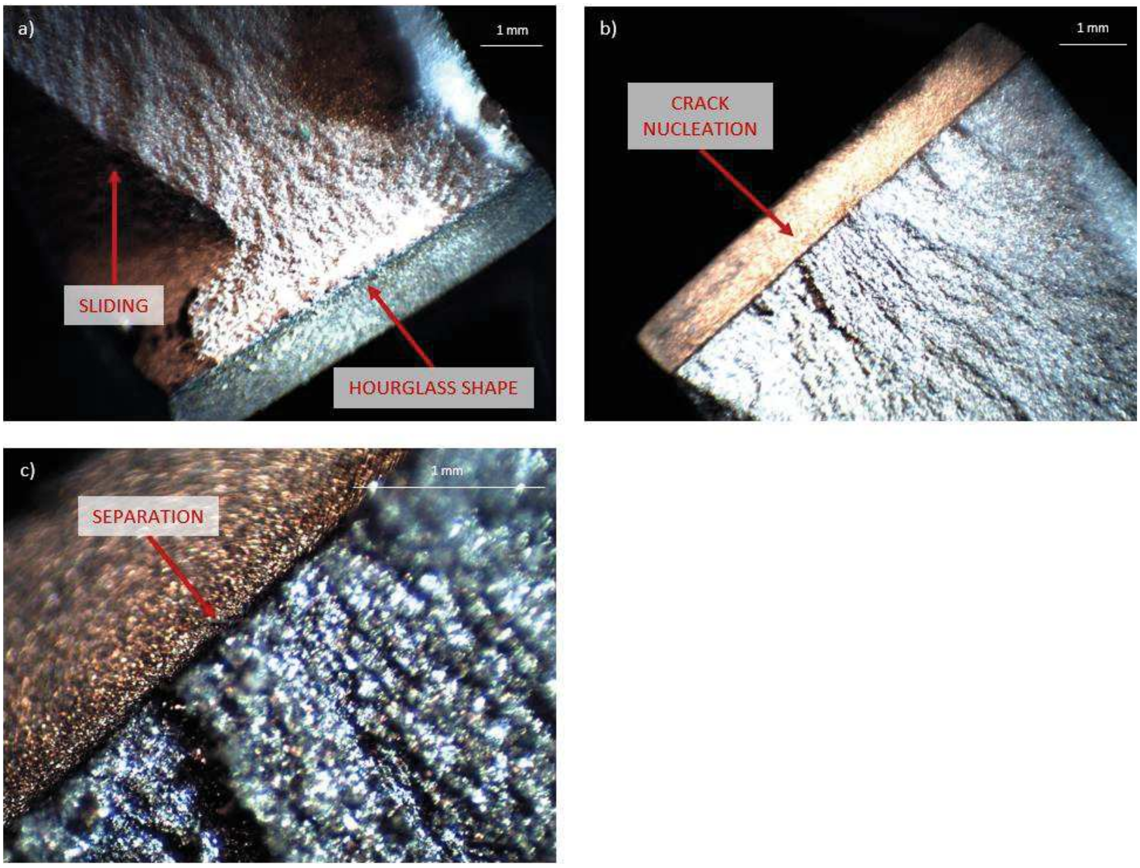

Figure 18 Fracture surface of the further N specimen in methanol: a) hourglass shape and sliding; b) crack nucleation; c) separation at the notches [126].

2.4. Remarks

Figure 19 [124] shows the stress and time to failure obtained with the quasi-static tests described in this chapter of the thesis. It could be argued that no substantial differences were found for the S and N samples tested in inert environment. The effects of methanol on the behavior of smooth samples in Ti-6Al-4V not subjected to STOA are negligible in terms of stress to failure. In [37], an appreciable reduction was observed for smooth sample of Ti-6Al-4V in methanol. Therefore, methanol appears to be less aggressive for the alloy without STOA. A drastic reduction of stress to failure was detected in the presence of sharp notches and aggressive environments, as demonstrated by the results of the experimental test with the SN specimen in methanol. In this case, the failure of the specimen occurred with a mechanism similar to that of the ductile metallic alloys, while in the other cases the failure occurred *ex abrupto*, with a mechanism similar to the brittle fracture. Ti-6Al-4V appears therefore to have an intermediate ductile/brittle behavior.

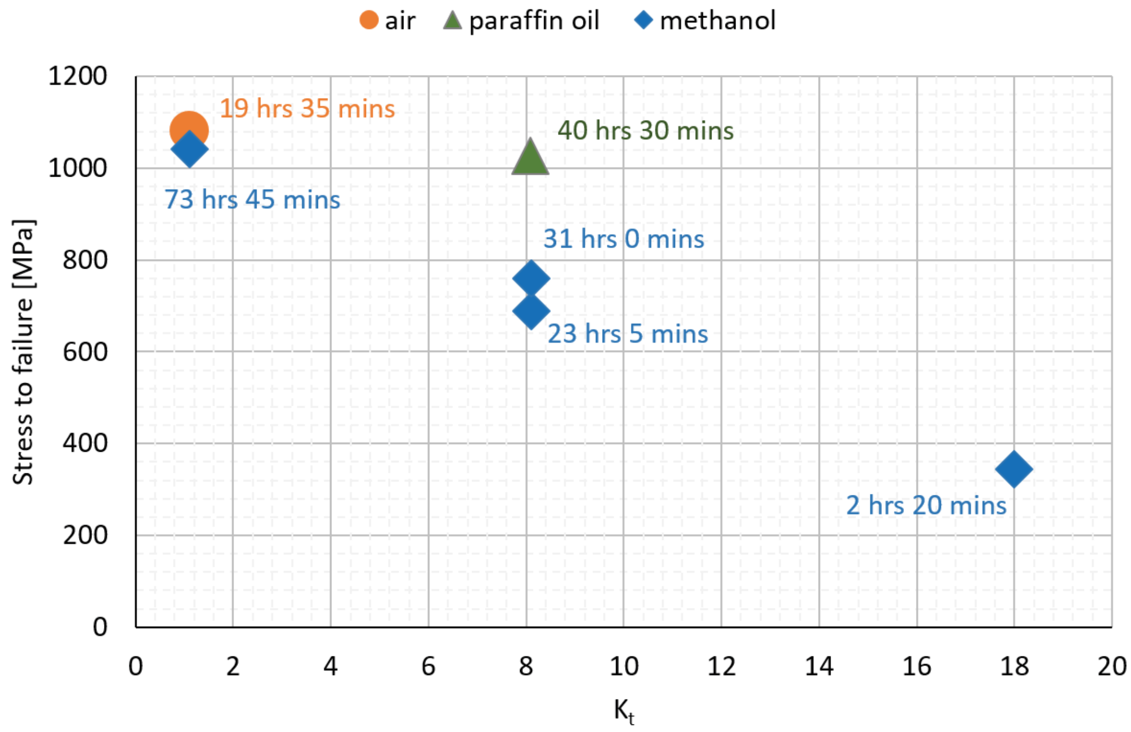

Figure 19 Results of quasi-static tests on Ti-6Al-4V without STOA: stress and time to failure [123-124].

In analyzing the results, there are some important aspects to consider. The experiments were not performed with the same strain rate and took different times. For this reason, the central parts of the tested samples were immersed in methanol for dissimilar times and the methanol had dissimilar times to attack the alloy. Also, the methanol used in the tests of the S and N specimens may have been contaminated with the humidity of the laboratory air. The lack of a complete seal of the tank could be responsible for this contamination.

The third test could be affected by these two aspects: at the end of the first step the load read by the load cell corresponded to an axial stress in the minimum cross section higher than 800 MPa; after the changes of the tank a stress to failure of about 700 MPa was obtained. An additional N specimen was tested in methanol in a completely filled and sealed tank. Compared to the result of the previous test with N specimen in methanol, a similar stress to failure was found (760 MPa vs 689 MPa). The time to failure is different. This may be due to the different total time of exposure to the corrosive environment. When the tank was replaced, the sample was not cleaned, so a small amount of methanol remained on the sample and may have interacted with it. The results seem to confirm the influence of strain rate and immersion time on the strength of Ti-6Al-4V without STOA. In detail, the moisture can contaminate the methanol and reduce its aggressiveness.

Macroscopic fracture surface analysis helped identify the contributions of the chemical and mechanical driving forces. The chemical force is associated with the type of environment in which the alloy is immersed; the mechanical driving force consists in the stress concentrations induced by the notches. The analysis revealed that methanol is very harmful at the edges of the sample. The steep stress gradients induced by sharp notches are responsible for the initiation of the cracks. In general, the biphasic nature of the alloy emerged also from the analysis of the fracture surfaces, which confirmed its intermediate brittle/ductile behavior.

3. Fatigue strength of 7075-T6 coated by PVD

This Section reports the experimental fatigue tests conducted on uncoated and coated 7075-T6 specimens. The coating was deposited by PVD. The aim is to identify the influence of the coating on the fatigue strength of the components. The analysis was carried out by means of experimental tests, fracture surface analysis and FE modelling. The work was object of various conference presentations [129-131] and reported in various papers [132-135].

3.1. Materials and methods

An experimental fatigue test campaign was conducted over some uncoated and DLC-coated 7075-T6 samples in order to evaluate their strength. The material properties of the tested aluminum alloy are reported in Table 3 [62,136]. The geometry of the samples, shown in Figure 20 [132-135] was designed according to ISO 1143 [137]. Figure 20a illustrates the 2D CAD of the samples, highlighting the grip points. Figure 20b and Figure 20c show the appearance of an uncoated sample and of a DLC-coated respectively. The specimens surface preparation consisted of the following steps: (i) polishing with 600 to 1200 grit paper; (ii) polishing with 3-micron diamond paste; (iii) cleaning with acetone. In line with ISO 1143 [137], polishing operations were carried out along the sample axis. The technique adopted for the coating deposition was magnetron sputtering [138], with a maximum process temperature of 180°C. The applied thermal load prevented huge changes in the mechanical properties of the bulk material, as its annealing temperature is 415°C, its solution temperature is 466°C–482°C, and its ageing temperature is 121°C [136]. Indeed, the coating application process does not change the crystallographic structure of the 7075-T6. The deposited DLC coating was amorphous and 2 μm thick. It featured a bi-layer architecture that improves stick properties. The first layer, closest to the bulk material and 1 μm thick, was columnar because of its initial growth; its composition was as follows: 55.2 wt.% carbon, 31.2 wt.% tungsten, 10.0 wt.% of aluminum, 2.8% wt.% chromium, and 0.75% wt.% titanium. The other layer was also 1 μm thick and contained the following elements: 81.9 wt.% carbon, 15.6 wt.% tungsten, 2.0 wt.% aluminum and 0.5 wt.% chromium [109]. The coating generated was very hard and stiff. It was characterized by a much greater elastic recovery than the bulk material, as shown in Table 4, which reports the outcomes of the nanoindentation tests conducted in [109]. The load applied in the experiments was 4 mN. However, the deposition process induced small hillocks on the surface of the coating. The surface roughness was measured with the aid of a Talysurf profilometer. The average roughness measured before the deposition was 0.034 μm; the average roughness after the process was 0.045 μm.

A rotating bending moment was applied to the sample. Generally, if the distribution of flaws is uniform (or zero) in the specimen, the size of the region where crack initiation is possible is limited. As known, a linear distribution of axial stresses is induced by a bending moment in the cross section of the sample. The maximum bending stress is reached on the sample surface. The high tensile stresses drive the nucleation of the cracks and therefore the crack initiation is expected in radial positions far from the center. In these areas the highest stresses are obtained. The experiments were conducted with an ItalSigma X2TM412 test machine. The rotational speed applied was 3000 rpm.

Table 3 7075-T6 chemical composition and material properties [62,136].

Chemical composition [wt.%]								
Al	Zn	Mg	Cu	Fe	Si	Cr	Mn	Ti
Bal.	5.60	2.55	1.75	0.32	0.25	0.22	0.20	0.12

Mechanical properties				
Tensile strength UTS [MPa]	Yield strength YS [MPa]	Poisson's ratio ν	Elastic modulus E [MPa]	Density ρ [kg/m^3]
650	598	0.33	71700	2810

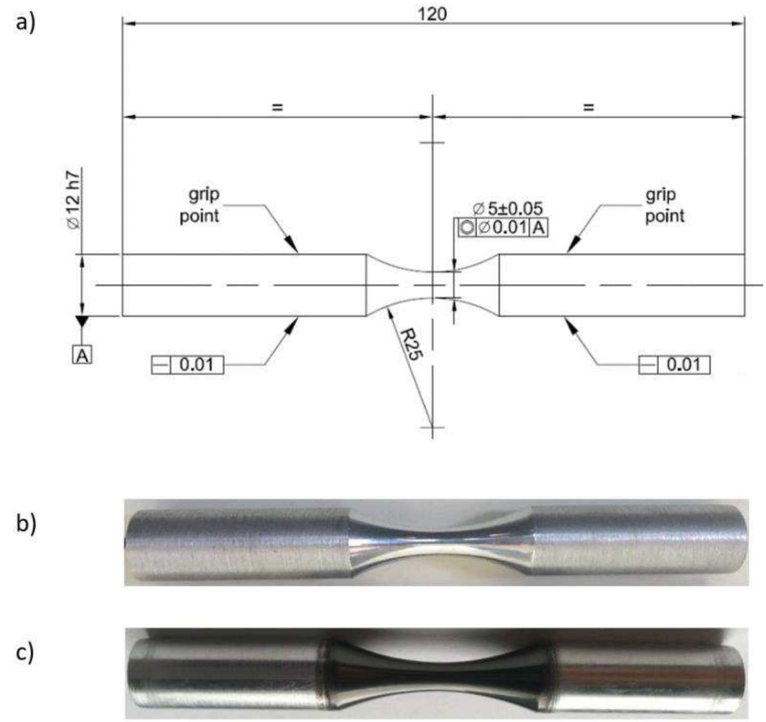

Figure 20 Specimens tested: a) 2D CAD; b) uncoated; c) with DLC [132-135].

Table 4 Results of the nanoindentation tests, applied load equal to 4 mN [109].

Property		DLC coating	7075-T6 substrate
Hardness	[GPa]	15.8 ± 1.4	1.95 ± 0.05
Reduced modulus	[GPa]	162 ± 14	82.6 ± 2.2
Maximum penetration depth	[nm]	80	252
Contact depth	[nm]	45	229

The stress to failure σ_{max} at a number of cycles N_{cycles} was calculated using a step test method [11,139-140]. This method can be used to identify the points on the σ_{max} vs N_{cycles} diagrams of the materials that are not subject to coaxing (other name: under-stressing) [140]. This phenomenon depends on the history of the applied load and it is the alteration of the alloy lattice that induces the improvement of the fatigue life of the component when it is subjected to a stress lower than the fatigue limit [11] . The following lines summarize the experimental procedure adopted:

(i) A single specimen was tested with a rotating bending moment that induced a maximum stress in the sample's minimum cross section which corresponded to 70%-80% of the probable fatigue strength; the calculated bending moment stressed the specimen for a block of cycles N_{cycles};

(ii) If the specimen did not failed in this block, the moment was increased by an amount corresponding to an increase $\Delta\sigma$ of the maximum stress in the minimum cross section of the sample; the new moment was applied for a block of cycles N_{cycles};

(iii) Step (ii) was repeated until the specimen failed; the specimen failed at a number of cycles $N_{failure}$, less than or equal to N_{cycles};

(iv) Once the failure occurred, the fatigue strength σ_{max} was calculated using Equation 2, which is the linear interpolation between the last two load blocks. In detail, the two stresses used for the interpolation are: the bending stress σ_{prior} applied in the minimum cross section in the last unfailed load block, which is prior to the failed load block, and the final stress $\sigma_{final} = \sigma_{prior} + \Delta\sigma$, at which the specimen failed:

$$\sigma_{max} = \sigma_{prior} + \frac{N_{failure}}{N_{cycles}}\Delta\sigma = \sigma_{prior} + \frac{N_{failure}}{N_{cycles}}\left(\sigma_{final} - \sigma_{prior}\right) \tag{2}$$

The step test technique can be adopted with the conventional σ_{max} vs N_{cycles} curve tests to remove run-outs, viz. the samples did not fail. Run-outs occur in traditional fatigue tests and they are hard to treat statistically. The step method also saves time. This technique can be used with increased load ratios and a constant mean stress to calculate the fatigue behavior for a particular mean stress [11].

The experiments were conducted in an air environment. The technique provides results within the statistical limits of the typical σ_{max} vs N_{cycles} curves. Two specimens are sufficient to determine the point on the curve. The first sample was tested to assess the stress to failure σ_{max} at the number of cycles N_{cycles}; the other one was the confirmation sample. A moment corresponding to the σ_{max} obtained with the first sample was applied to the second specimen. The specimen would have failed roughly at N_{cycles}. If the specimen did not fail, the step method was repeated, considering the one just completed as the first load block. Six uncoated specimens and eight DLC-coated specimens were tested. Half of the tested specimens are used as confirmation. The moment applied to the specimens was within the range 2.45 Nm – 3.45 Nm. Therefore, the maximum bending stresses obtained in the specimens were within the range 200 MPa – 281 MPa. Section 3.2 provides more information on the experiments. The results were fitted with two regression models in order to identify which was best.

A FE calculation was conducted to assess the stress distribution caused by the application of the bending moment. The FE outcomes and the fracture surface analysis were used to identify the mechanisms of fatigue crack initiation and propagation that caused the sample to fail. The FE calculation was performed with Dassault Systémes FE Abaqus 2017 software [128]. Abaqus/Standard was adopted. Thus, an implicit integration scheme was used. The model built for the calculation included the whole specimen. The constitutive law adopted was isotropic linear elastic. The mechanical properties of Table 3 were implemented. The mesh created is visible in Figure 21 [130,135] and it is the consequence of a convergence study. It was made of C3D8 elements. These elements are general purpose linear 8-node brick elements, with 2x2x2 integration points. Each element has zero rotational degrees of freedom and three translational degrees of freedom per node. Thus, an element has 8 x 3 = 24 degrees of freedom. Correspondingly, the shape function of the C3D8 elements is linear along the three directions and has 24 coefficients. Figure 21 shows only a quarter section along the three planes parallel to the Cartesian ones in order to appreciate the mesh built. The three symmetry planes that can be identified on the unloaded specimen are indicated in the figure. Only the boundary condition on the Symmetry plane 2 of Figure 21 was implemented. This is consistent with the loading condition, i.e. the application of a bending moment. The moment was implemented as two concentrated forces applied to each end of the sample. The magnitude of the forces was equal; the direction was opposite. The two forces lied on the Symmetry plane 3 which was then a symmetry plane even in the deformed configuration. However, no boundary conditions were set on this plane because they were not strictly needed for the calculation.

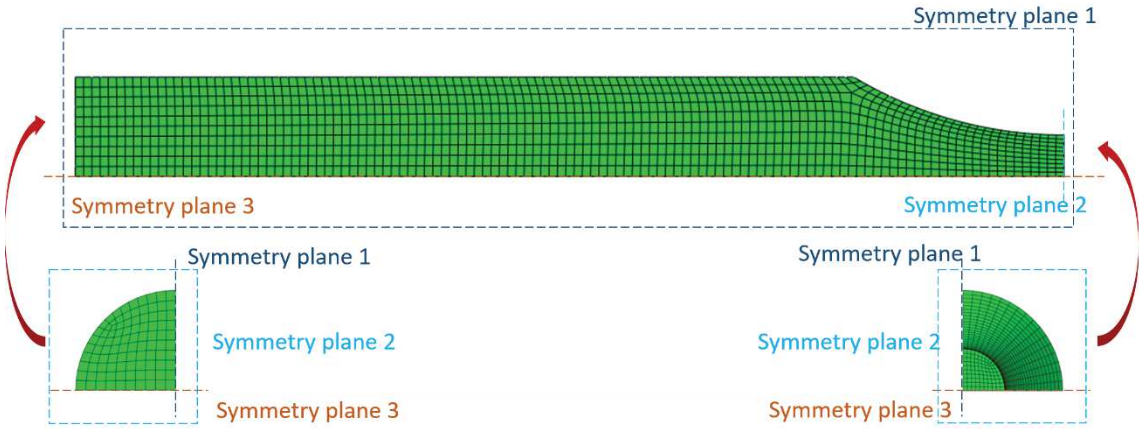

Figure 21 FE model for assessing the stress distribution [130,135].

The stress results obtained with the FE analysis in the minimum cross section were graphically superposed on the fracture surface obtained. By adding the bending stresses to the residual stress state generated by the coating deposition process, an estimation of the real stress state of the section was found. The final stress distribution obtained made it possible to identify the regions of the section that suffered the greatest stresses. In these regions crack initiation is likely, if the defect distribution in the sample is uniform.

3.2. Results

3.2.1. Stress – number of cycles diagram

Table 5 shows the method adopted to calculate the points of the $\sigma_{max} - N_{cycles}$ diagram of Figure 22 [129-135]. In detail, the table indicates:

- The name that identifies the sample tested ("U" refers to an uncoated sample; "D" to a DLC-coated sample);
- Whether the coating was applied or not;
- Whether the sample was used to confirm the result;
- The number of cycles N_{cycles} at which it was desired to determine the fatigue strength;
- The number of cycles $N_{failure}$ in which the sample failed;
- The stress σ_{final} at which the sample failed;
- The calculated value of fatigue strength σ_{max} for the single sample;
- The stress value plotted in the diagram, that is the average stress value obtained with the two specimens tested to determine the fatigue strength at N_{cycles}.

With regard to the fatigue strength of the uncoated samples determined at $5 \cdot 10^5$ cycles, the failure of the confirmation sample occurred at a number of cycles which was very close to N_{cycles}. The value of $N_{failure}$ obtained is greater than N_{cycles}. This result may be due to the inertia. Since $\frac{507355}{500000} = 1.015 \sim 1$, the fatigue strength at $5 \cdot 10^5$ can be directly assumed to be 248 MPa, neglecting the stress obtained with the other sample, 251 MPa. To guarantee a standardized method for determining the points of the graph, an average stress value was calculated considering σ_{max} for the sample U2 equal to σ_{final}, $\sigma_{max}(U2) = \sigma_{final}(U2)$. Anyhow, the error made is almost nil, $\frac{249.5\ MPa - 248\ MPa}{248\ MPa} < 1\%$.

The circles and squares in Figure 22 are the mean values of stress to failure determined in Table 5 for the uncoated and DLC-coated samples, respectively. The values of σ_{max} calculated for each sample tested are designated with horizontal lines. The white markers refer to results presented elsewhere [141]. Coating deposition seems to induce a general decrease in 7075-T6 fatigue strength in the range $2 \cdot 10^5 - 10^7$ cycles. This reduction is noteworthy for the lowest number of cycles, from $2 \cdot 10^5$ to 10^6. The maximum decrement in fatigue stress was found at $2 \cdot 10^5$ cycles and was equal to –15%. It is mainly due to the thermal load suffered by the sample during the deposition process, as stated in [142]. In this paper, it was found that the fatigue strength of uncoated samples which underwent the same thermal load applied during the deposition process was almost the same as that of DLC-coated samples. The small thermal load and the induced surface compression state [61,109,134] could explain the small variation in fatigue strength within the range of cycles studied, $2 \cdot 10^5 - 10^7$cycles. At about 10^7 cycles the fatigue strengths of the uncoated and DLC-coated sample are comparable. In addition, it seems that the fatigue strength of the uncoated samples is lower than that of coated at 10^7 cycles. If this trend is confirmed, it will imply a better performance of the coated components at high number of cycles. The coating will improve the fatigue, as well as wear resistance [105]. It would be fascinating to assess the fatigue strength of uncoated and coated samples at greater numbers of cycles. Unfortunately, ultrasonic testing machines will be needed to assess the fatigue strength in this regime within acceptable times.

The data obtained were fitted with two regression models in Excel 2016. The regression models adopted are linear and piecewise linear. Further regressions models can be used to fit the data. One of these is for example the polynomial one. It is clear that the higher the polynomial degree, the better the curve fits the points in the diagram. Polynomials could lead to troubles, returning fatigue strength at high numbers of cycles bigger than that at small numbers, since they are not monotonous at all times. The suggested piecewise linear regression is made of three parts. The first and the third parts are constant functions, the second is a decreasing function. The first and third pieces of the curve contain the first and the last point, respectively. The second part is the linear interpolation of the remaining data points. The third part of the piecewise regression is used only to estimate the fatigue strength at the end of the investigated region. As it is known, aluminum alloys have no fatigue limits and therefore the fatigue strength continues to decrease with the increase in the number of cycles. When the fatigue strength at numbers of cycles greater than 10^7 is evaluated, an in-depth analysis on the regression models will be possible. Figure 22 shows the trend line equation and the coefficient of determination R^2 of the studied regression models. These parameters help identify which line best fits the experimental results. In the equations, x and y denote $\log_{10}(N_{cycles})$ and σ_{max} respectively. The coefficients are rounded to the nearest first decimal. For the piecewise linear regression, only the equation of the second part is reported. As shown in Figure 22, the two suggested regression models could describe the behavior of the samples without DLC: R^2 is very close to 1, 0.96 for linear and 0.94 for piecewise linear regression. It is difficult to appreciate notable differences between the two curves. For this reason, a linear regression is suitable in the range of cycles $2 \cdot 10^5 - 10^7$cycles. With regard to the behavior of the coated specimens, a substantial scatter of data is visible. This scatter is also due to the very high difference in the stresses obtained at $N_{cycles}=3 \cdot 10^5$ and $N_{cycles}=5 \cdot 10^5$ cycles with the two tested specimens. As indicated in ISO 12107 [143], scattering usually appears in fatigue tests even if the experiments are conducted carefully. This behavior may derive from the possible different chemical composition and heat treatment among the specimens. In addition, small cracks can initiate and grow in test media. As for the coated samples, it is possible that DLC had not totally adhered to the aluminum, there could have been defects in the coating and the high surface compressive stresses could have induced spallation. This high scatter is highlighted by the small values of R^2 found: 0.53 for the linear and 0.49 for the linear piecewise regression. Further tests could help to understand the trend.

Table 5 Stresses resulting from the tests and calculation of the graph points [129-135].

Name	Coating	Confirmation	N_{cycles}	$N_{failure}$	σ_{final} [MPa]	σ_{max} [MPa]	Mean value [MPa]
U1	No	No	500000	101123	255.0	251.0	249.5
U2	No	Yes		507355	248.0	248.0	
U3	No	No	1000000	74007	275.0	251.9	252.2
U4	No	Yes		79160	260.0	252.5	
U5	No	No	2000000	1606118	240.0	238.0	237.1
U6	No	Yes		550038	239.0	236.1	
D1	Yes	No	300000	48543	290.0	273.2	247.2
D2	Yes	Yes		167638	230.0	221.2	
D3	Yes	No	500000	32049	245.0	240.3	236.8
D4	Yes	Yes		325728	235.0	233.3	
D5	Yes	No	2000000	1830631	230.0	229.2	232.3
D6	Yes	Yes		1083723	240.0	235.4	
D7	Yes	No	5000000	433929	250.0	240.9	225.7
D8	Yes	Yes		223033	220.0	210.5	

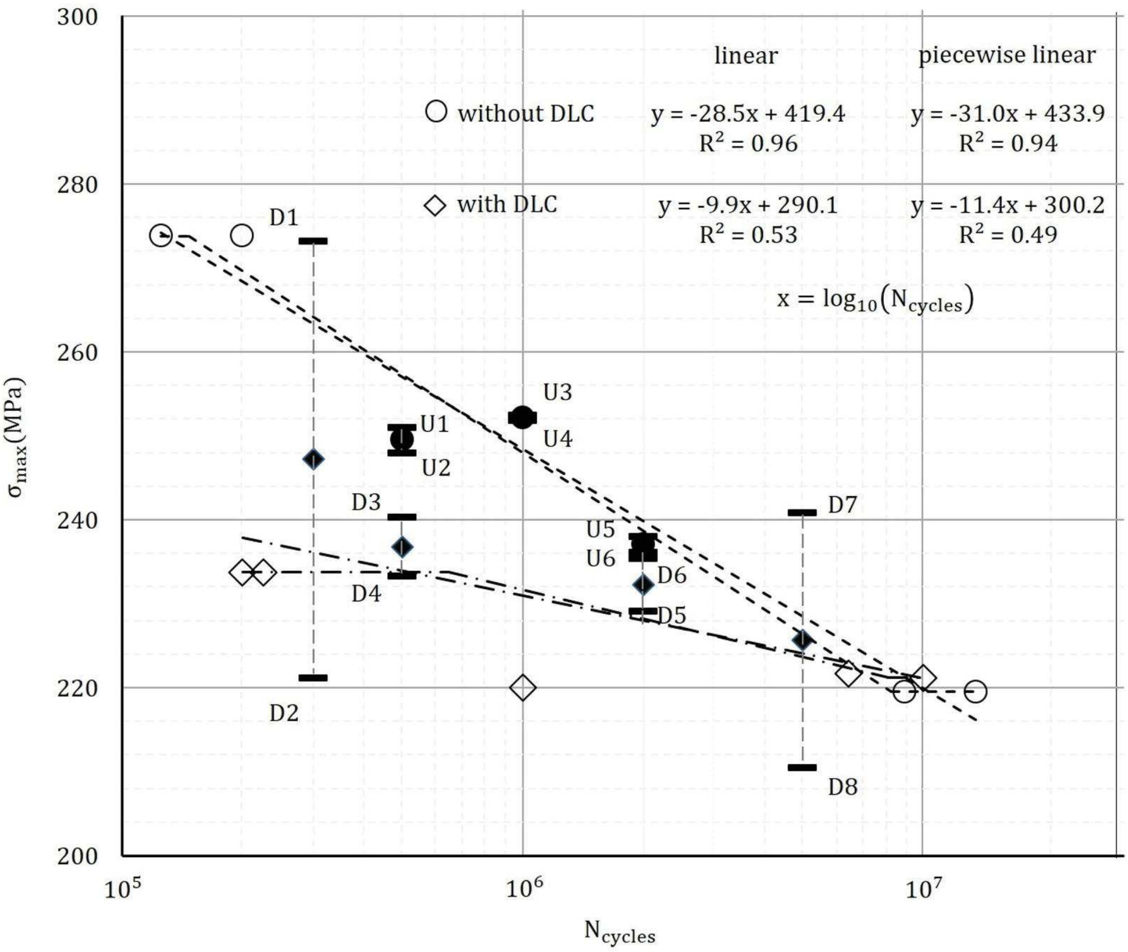

Figure 22 Experimental results of rotating bending fatigue tests on 7075-T6 samples [129-135]. In the equations, y= σ_{max} and x=$\log_{10}(N_{cycles})$. Only the equation of the second part of the piecewise linear function is reported. The white points refer to [141].

3.2.2. Analysis of the fracture surfaces

Figure 23 [129-134] shows the fracture surfaces of some tested specimens: Figure 23a refers to an uncoated specimen; Figure 23b-g refer to some DLC-coated specimens. The surfaces of the DLC-coated specimens are reported in the order of σ_{final}: D8 (σ_{final}=220 MPa, Figure 23b), D5 (σ_{final}=230 MPa, Figure 23c), D4 (σ_{final}=235 MPa, Figure 23d), D6 (σ_{final}=240 MPa, Figure 23e), D7 (σ_{final}=250 MPa, Figure 23f) and D1 (σ_{final}=290 MPa, Figure 23g). The characteristic fracture surfaces of cylindrical samples tested with rotating bending loads show one or more crack nucleation points and two areas [55,144], Figure 24. The first is the crack propagation area, the other one is the final overload failure area. Beach marks appear in the crack growth area. These lines can be seen by the naked eye. Their width and density are related to the applied load and the number of cycles. Each mark corresponds to a cycle package. Typically, small-amplitude stresses induce the initiation of a single crack, high-amplitude stresses and stress concentrations induce the nucleation of multiple cracks. In case of applied stresses of high amplitude, the final overload failure is larger than the growth area. In a rotating bending test, all points of the sample surface are stressed equally. Therefore, cracks can nucleate at the weakest point subjected to tensile stresses. The nucleation point, the propagation area and the final failure area are denoted as n, p and f respectively in Figure 23. In U1, a single crack nucleation is detected on the specimen surface (Figure 23a). The nucleation could be induced by the steep stress gradient generated by the bending moment and by any defects caused by the polishing operations. As for the coated samples, it appears that a single crack initiates beneath the surface of the samples in Figure 23b-f. It is probable that multiple cracks nucleate in the specimen failed at the greatest stress, 290 MPa, Figure 23g. The reduced magnification does not allow to identify the nucleation points and the growth area, which is much smaller. The purpose of this analysis is not to recognize these regions in detail, but to assess which are the main parameters which influence the nucleation and the growth of the cracks. Consequently, the final failure area simply is marked in Figure 23g. This surface is typical with high amplitudes of load [55,144]. The flake shown in Figure 23g points out the important plastic strain undergone by the sample prior to failure. The tests were run uninterruptedly and then a single cycle package was applied. For this reason, beach marks are not visible on the fracture surfaces. As for the mechanism, the fatigue process begins with sliding back and forth on crystallographic planes to produce a band [145], Figure 25. In these bands the cavities appear and come together to generate microcracks, that grow and merge creating macrocracks. Subsequently, the propagation of the cracks is induced by normal stresses and no more by shear stresses. The cracks propagate on a plane perpendicular to the applied load. The stress concentration forms two plastic areas at the crack tip. If one assumes a compression state as the initial situation, the crack opens and propagates in the next traction state. A new state of compression induces the micro crack to close again. Striations are generated by this mechanism. Only scanning electron microscopy can detect their presence. In the later stages, the crack propagates and the frontal ligament is reduced. In any case, fatigue becomes low cycle fatigue and shear stress is again the driving force for crack propagation. The crack propagates along a direction that forms a 45-degree angle with the maximum stress direction. Finally, after an adequate number of cycles, the ligament declines to failure [55,144].

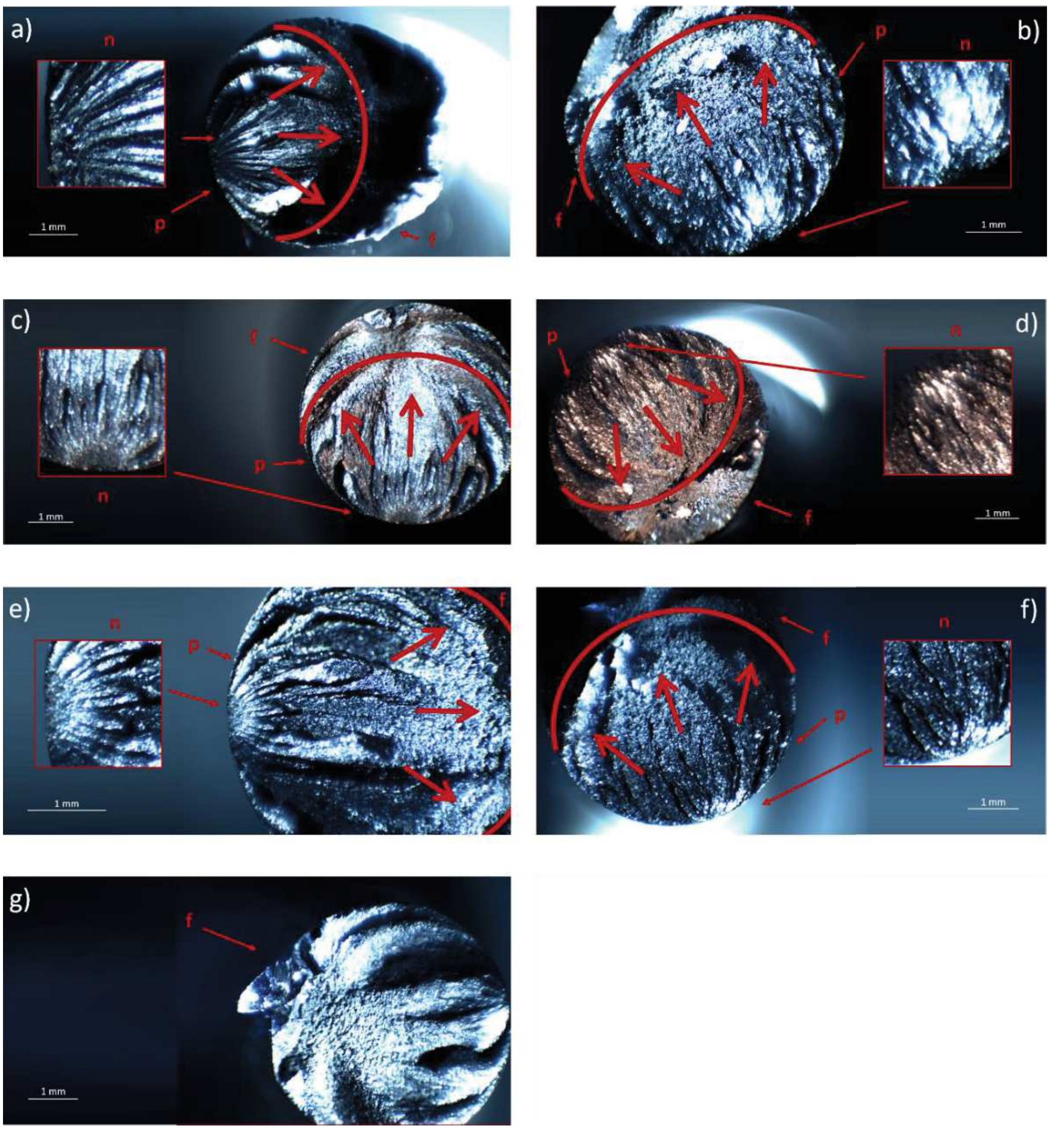

Figure 23 Fracture surfaces a) U1; b) D8; c) D5; d) D4; e) D6; f) D7; g) D1[129-135].

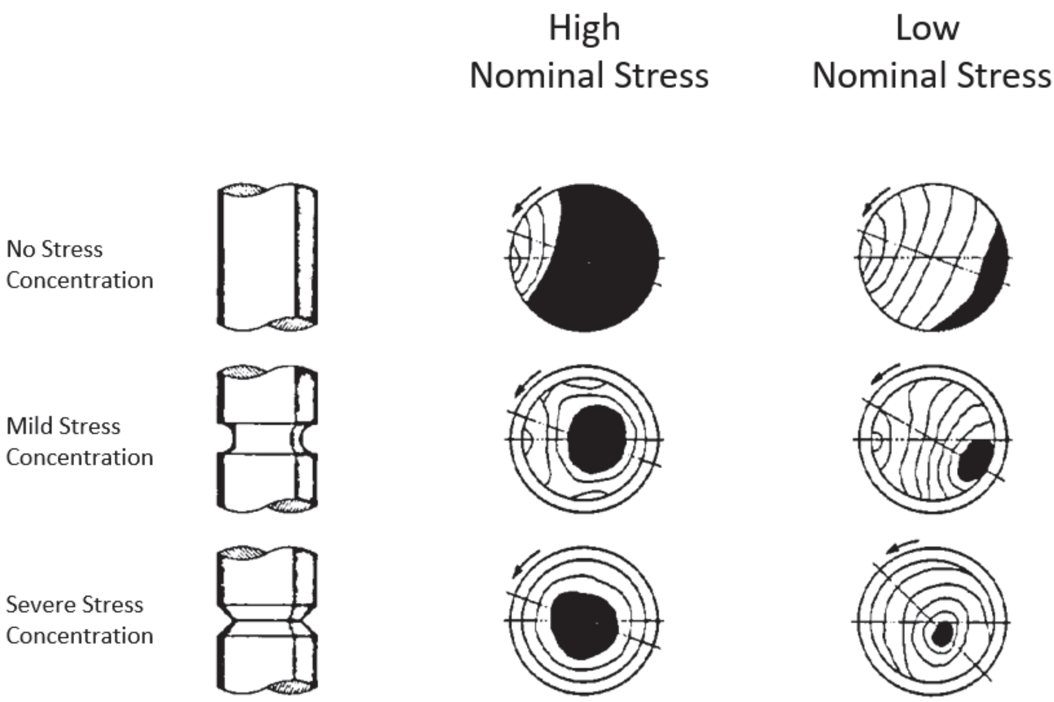

Figure 24 Typical fracture surfaces under rotating bending stresses [55,144].

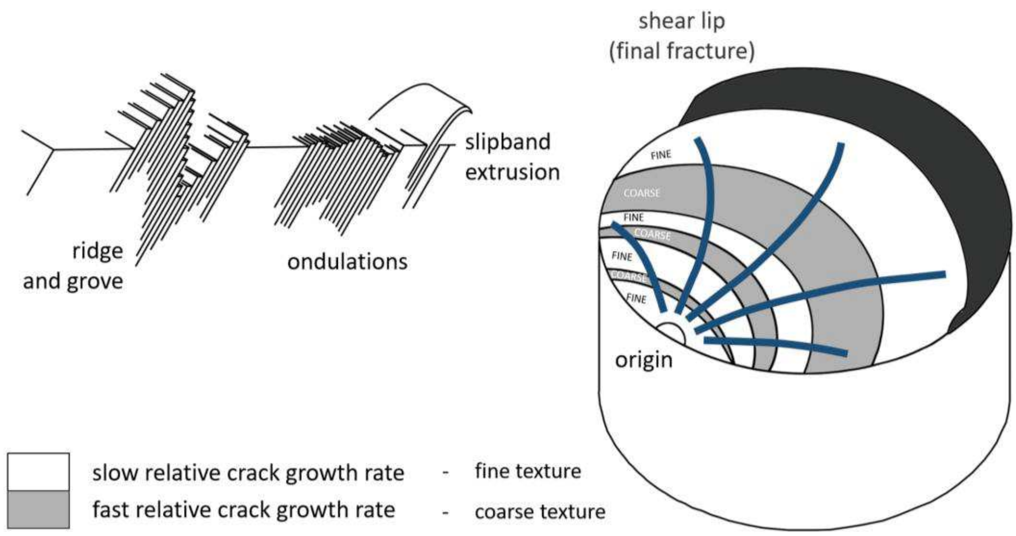

Figure 25 Failure mechanism [145].

3.2.3. Stress analysis

The possible crack nucleation areas were identified by superposing the bending stresses obtained from the finite element calculation with the residual stresses induced by the coating deposition process. Due to the small size of the specimen and the relatively low velocity (3000 rpm), the stresses induced by the rotational speed are obviously very small and their contribution to the stress field in the specimen during the fatigue test can be neglected.

The study was conducted on two samples, D8 and D1, which failed at 220 MPa and 290 MPa respectively. The analyses for the two samples are shown in Figure 26 and Figure 27 [134]. The stress field induced by the deposition of the coating was added to the bending stress. In both figures, the distribution of maximum principal stresses, detected with the FE analysis, superposes the fracture surface. The diagrams in the figures show the residual stresses, the bending stresses and their sum in the area z=2.0-2.5 mm respectively in blue, orange and red. The residual stress distribution was adapted from [146]. This paper provides the residual stresses in the longitudinal direction of a prismatic block coated by PVD. The geometries of the hourglass sample studied in this thesis and of the prismatic block of [146] were considered comparable, such as the distribution of induced stresses. What is important in this study is the compressive stress state induced by the deposition of the coating on the sample surface. The residual stress state is in equilibrium and therefore there is a maximum tensile stress under the surface of the specimen. Residual stresses are zero away from the surface. In Figure 26 and Figure 27 the colors from red to blue correspond to the bending stress values of the attached legends. The bending stress in the minimum cross section of the sample was assumed as a linear function of the z position. For D8, the maximum principal stress was 87.78 z, Figure 27. The superposition of the stresses gives a value of −1281 MPa, compressive in nature, on the sample surface, and a maximum value of 576 MPa, tensile in nature, at z approximately equal to 2.4 mm. For D1, the maximum principal stress was equal to 115.71 z, Figure 27. The superposition of the stresses gives a value of −1210 MPa, compressive in nature, on the sample surface, and a maximum value of 643 MPa, tensile in nature, at z approximately equal to 2.4 mm. In both cases, the surface of the sample is subjected to compression since the amount of residual stresses on the surface is much higher than that of the bending stresses. These considerations can be extended to all coated samples, as the bending stresses are much less than the residual stress on the surface. As a consequence of the results, it is very likely that cracks nucleate under the sample surface, where the greatest tensile stresses are obtained, if the distribution of flaws in the specimen is uniform or zero. Conversely, the high residual compressive stresses on the surface can induce spallation of the coating.

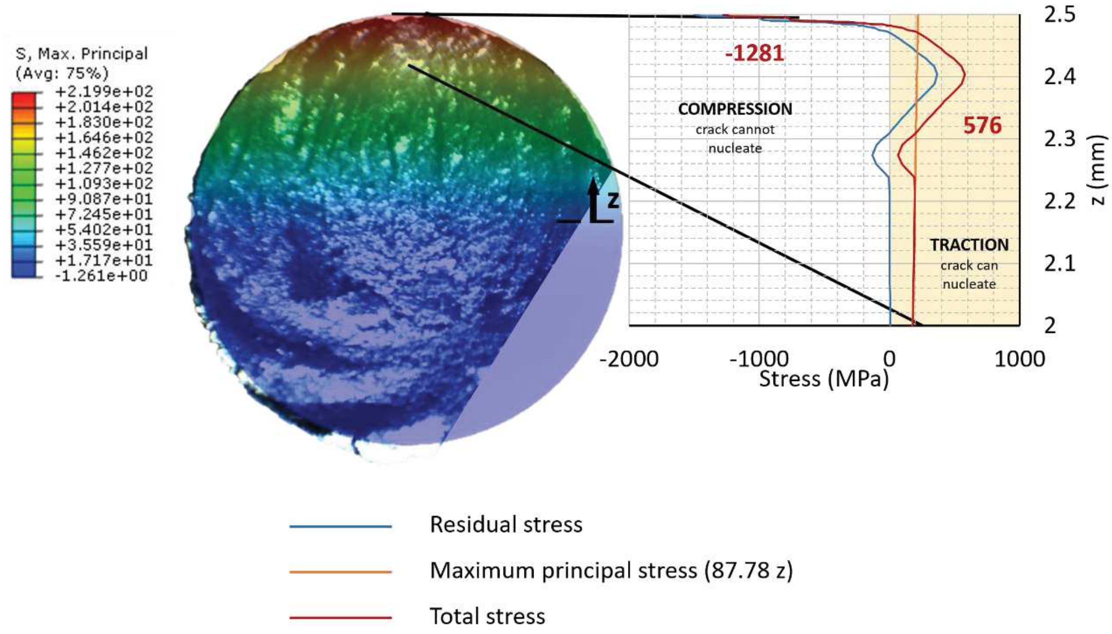

Figure 26 Superposition of stresses [MPa] on fracture surface of D8 [134].

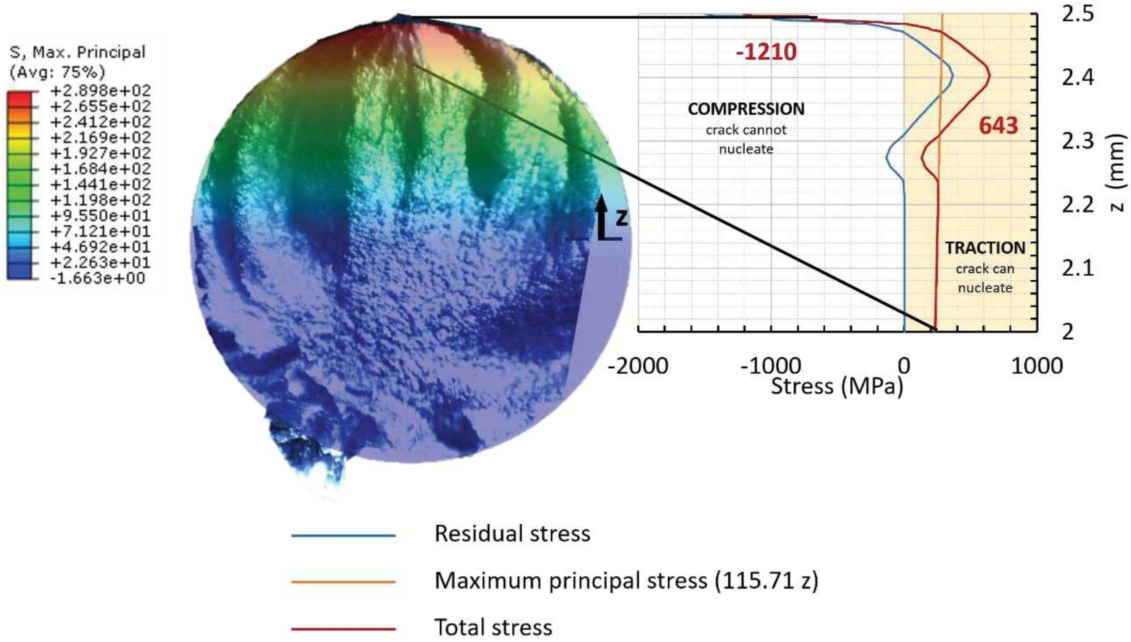

Figure 27 Superposition of stresses [MPa] on fracture surface of D1 [134].

Hydrostatic stresses, or "equivalent pressure stresses" as they are called in the Abaqus software, were assessed in the minimum cross section of the sample. Equivalent pressure stress is defined by Equation 3 as minus one third of the stress tensor trace:

$$p = -\frac{1}{3} trace(\bar{\bar{\boldsymbol{\sigma}}}) \tag{3}$$

Knowing the distribution of the hydrostatic stresses, an assessment of the hydrogen embrittlement process is possible, as stated in [141,147]. The increase in the hydrogen content at the tip of the crack is indeed influenced by hydrostatic stress. This stress changes the material lattice. High hydrostatic stresses induce high concentrations of hydrogen. A high hydrogen content may generate restrictive reversed plasticity and cause the nucleation and propagation of fatigue cracks.

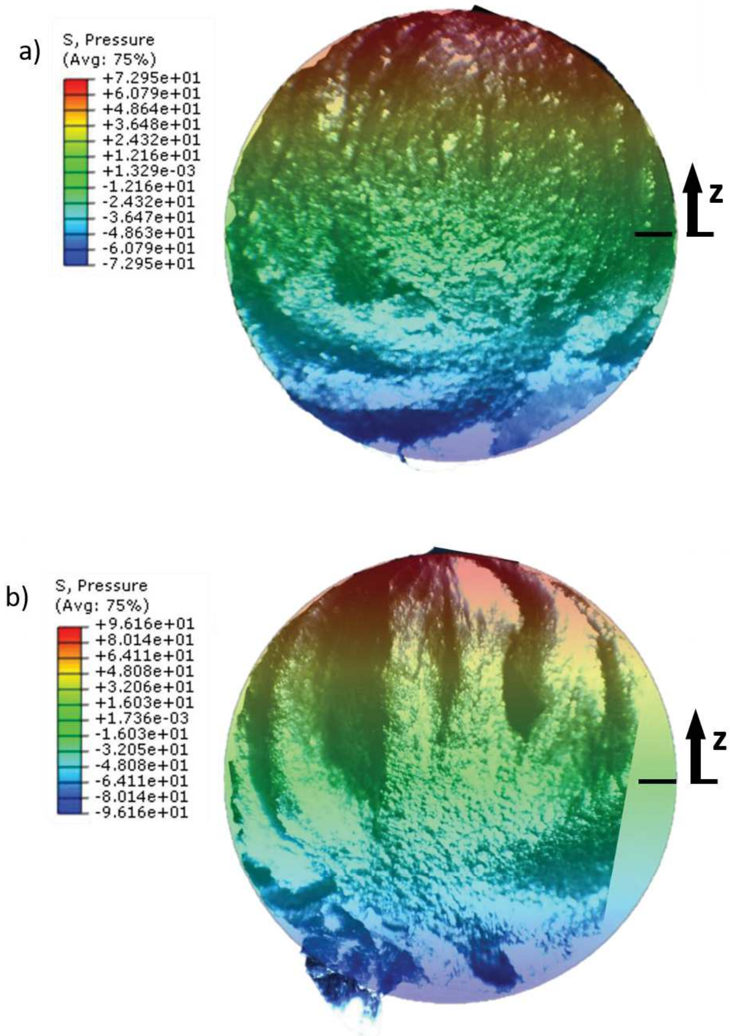

Figure 28 Equivalent pressure stress [MPa]: a) D8; b) D1 [134].

Figure 28 [134] illustrates the equivalent pressure stress fields in the minimum cross sections of the sample when the applied bending moments induce a maximum stress of 220 MPa and 290 MPa, which are the σ_{final} values for D8 and D1, respectively. The fields are graphically superposed on the fracture surfaces. A maximum equivalent pressure stress of 73 MPa and a minimum of −73 MPa were obtained at the top and bottom of the minimum cross section for a bending stress of 220 MPa, respectively, as shown in Figure 28a. Figure 28b shows that a bending stress of 290 MPa generates a maximum stress of 96 MPa at the top and a minimum of –96 MPa at the bottom. In both cases, high stresses are obtained near the surface of the sample. Therefore, under the sample surface there are high tensile residual stresses (Figure 26 and Figure 27) and high tensile hydrostatic stresses (Figure 28). Crack nucleation is therefore envisaged in this area.

3.3. Remarks

The experimental campaign on 7075-T6 hourglass specimens, uncoated and coated with DLC, shows that the deposition of DLC induces a significant reduction in fatigue strength in the range $2 \cdot 10^5 - 10^6$ cycles. In the range $2 \cdot 10^6 - 10^7$ cycles, the fatigue strengths of the samples without and with DLC are similar. Two regression models were studied to fit the results obtained for the tested range of number of revolutions. For uncoated specimens, a linear regression may be appropriate. Piecewise linear regression is proposed to define the fatigue behavior of the DLC samples although it is possible to see a high scatter of experimental results. Furthermore, as known, aluminum alloys do not present fatigue limits and for this reason some tests at very high cycles will help to identify the trend of the fatigue behavior for the coated samples. Observation of the fracture surfaces of the DLC-coated specimens shows a single crack initiation in the event of failure at low stress amplitudes. More cracks nucleated in the sample failed at high stress amplitude, 290 MPa. In this case, the extent of the overload failure area is almost the entire surface. The fracture surface obtained is typical of failures under high amplitude stresses. The superposition of the stress induced by the bending moment with the residual stress generated by the deposition of the coating reveals high compressive stresses on the surface. Consequently, crack nucleation is likely beneath the surface of the DLC-coated specimens, where the greatest stresses, tensile in nature, are obtained, as confirmed by the observation on the tested specimens. Crack initiation in the uncoated specimens occurs on the surface due to the steep stress gradient associated with the application of a bending load and any flaws introduced in polishing operations.

4. FOD on 7075-T6

The following paragraphs describe the numerical model developed to evaluate the stress distribution in a 7075-T6 hourglass sample tested with a rotating bending fatigue load after being subject to FOD. The model and its results were presented at the ICSID 2020 conference [148] and in a paper [149].

4.1. Materials and methods

The collision of a steel ball against a 7075-T6 hourglass specimen was simulated numerically. An hourglass sample was considered because of the type of fatigue test chosen to be performed after the impact and to consider a geometry which is more complex than the planar ones commonly present in the literature. The FE analysis was performed in Abaqus 2019 [128]. The problem considered involves an impact. For this type of problem, it is recommended to use an explicit integration method [150-153] and for this reason the calculation was performed with Abaqus Explicit.

The hourglass sample and the sphere were included in the model. Their geometries, the mesh adopted for these components and the implemented boundary conditions can be seen in Figure 29 [149]. A mesh made of 92160 C3D8R elements was adopted for the sample. According to Abaqus terminology, C3D8R elements are general purpose linear brick elements, reduced integrated. A mesh made of 1536 R3D4 elements was adopted for the sphere, considering it non-deformable. This assumption is reasonable because the steel of the sphere is much stiffer than the aluminum of the specimen. R3D4 elements are bilinear quadrilateral rigid elements.

The specimen was assigned a perfectly plastic elastic material. The mechanical properties are the same of Table 3 and they are shown in Figure 29: density ρ of 2810 kg/m^3, Young's modulus E of 71700 MPa, Poisson's ratio ν of 0.33, yield stress R_s of 598 MPa [62,136]. Since the sphere was considered rigid, its mass and moments of inertia were given to the Reference Point (RP). RP was placed in the center of the sphere. The implemented material properties considered a density ρ of 7860 kg/m^3 for steel. Actually, the units of measurement used for the analyses are the following: kg for masses, mm for length, and ms for times. Therefore, the stresses and pressures are expressed in GPa in the figures extrapolated by Abaqus shown in Result section.

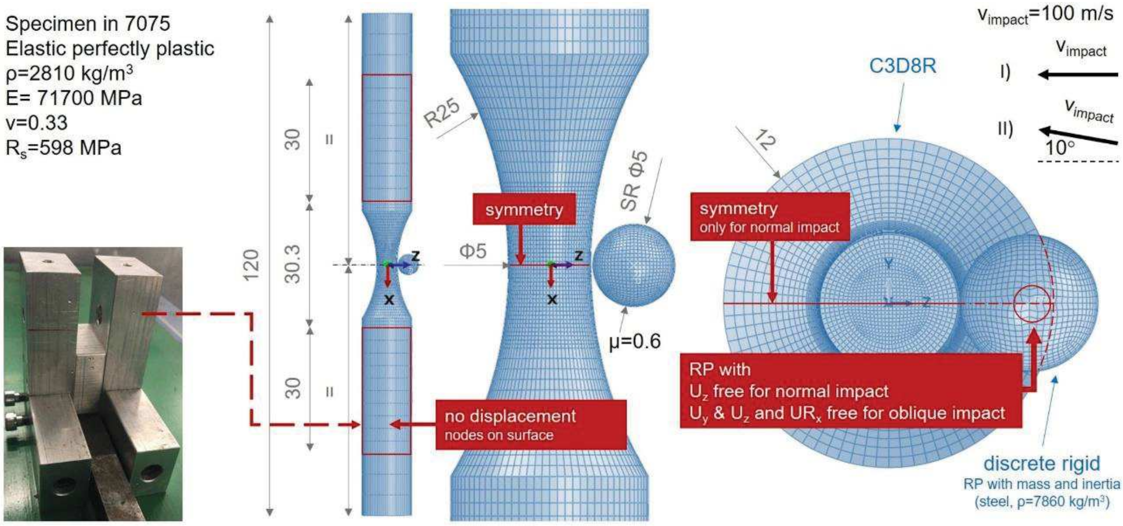

Figure 29 FE model for FOD on 7075-T6, dimensions in mm [149].

The FE model was created to simulate the conditions obtainable with the test rig built by the SMLab research group. This rig will be adopted for future experimental validations. A method which involves theoretical, numerical and experimental approaches is of great help when dealing with engineering problems. A comparison between the results of these three areas allows to validate the results and to understand if any parameter has been neglected. The lower left corner of Figure 29 shows the support where the specimen could be placed. The two cylindrical parts of the sample are accommodated in the through holes of the support. Then set screws tighten the sample. It was assumed that a compressed air-gun setup fired the sphere and that the support was positioned near the gun. As a consequence of the experimental setup, the contribution of air on the movement of the sphere is negligible. The motion of the sphere can be considered linear and not parabolic.

The sphere was then placed close to the collision area, in the proximity of the minimum cross section of the sample. The implemented distance between the sphere and the sample is of 0.1 mm. The x- and y-coordinates of the sphere's RP were the same as the corresponding coordinates of the center of the minimum cross section. Gravity loading was not implemented. These assumptions saved running time of simulations. Two collisions were studied, one normal (case I) and one oblique (case II). In the case I of normal impact, the direction of the initial speed of the sphere coincided with the z axis of the Cartesian coordinate system shown in Figure 29. In the case II of oblique collision, the initial speed of the sphere lay in the yz plane. The angle of impact was 10° and the speed was directed towards the upper part of the specimen (y+). In both the impacts, I and II, the initial sphere's speed was 100 m/s in magnitude. In Abaqus, the initial ball speed was implemented as a predefined field. A coefficient of friction of 0.6 was assigned to the interface between the sample and the sphere.

The implemented boundary conditions correspond to those obtainable with the test rig presented in the previous lines. The displacement of the nodes placed on the part of the cylindrical surface of the sample that interacts with the holes was prevented. Symmetry conditions were applied, reliable with the simulated collision type. In the both cases, I and II, a symmetry condition was implemented on the plane that contained the sample minimum cross section. Only in the case I of normal impact, an additional symmetry condition was set to the sample. In detail, this condition was applied to nodes on the xz plane. Based on the boundary conditions implemented to the sphere, the RP could only translate in the z direction, which was the direction of impact, in the case I of normal impact. In the case II of oblique collision, the RP could translate along the y and z axes and revolve around the x axis.

The results reported in the following paragraphs refer to the situation 7 ms after the start of the movement of the sphere. At this time, it can be assumed that the stresses in the minimum cross section of the specimen are stabilized. In other words, the vibration of the sample as a consequence of the impact can be considered negligible. Stress analysis focused on the central cross section of the sample, where maximum bending stresses can be found since this section is the minimum one already in the non-deformed configuration. It is reasonable to assume that the failure of the specimen will occur in this section, if a uniform (or zero) defect distribution is assumed. Four processors were used for the analysis.

4.2. Results

The effects of normal and oblique collisions were examined at three levels: (i) contact stresses; (ii) induced residual stresses; (iii) stress field in the minimum cross section during the rotating bending fatigue test.

4.2.1. Normal impact

Figure 30 [149] shows the contact stresses and displacements in case I of normal impact. In detail, it illustrates the distributions of von Mises stress (Figure 30a), contact pressure (Figure 30b), displacement (Figure 30c) and displacement in z direction (Figure 30d), which is the direction of impact. The figure refers to the time t= 0.00136 ms. At this time, the sample material is near yielding. Therefore, stresses and displacements can be assumed elastic. The contact stress and pressure and the displacements can be considered symmetric with respect to xz and yz planes. The contact stress and pressure are the highest at the center of the contact region. Here, the magnitude of the displacement is maximum. As a consequence of the implemented boundary conditions, the displacement in the center of the contact area is completely directed along z axis. This result is reasonable due to the physics of the problem. The distributions of stresses and strains are therefore in agreement with the typical distributions obtained with the application of a surface pressure. The best known is the Hertzian distribution.

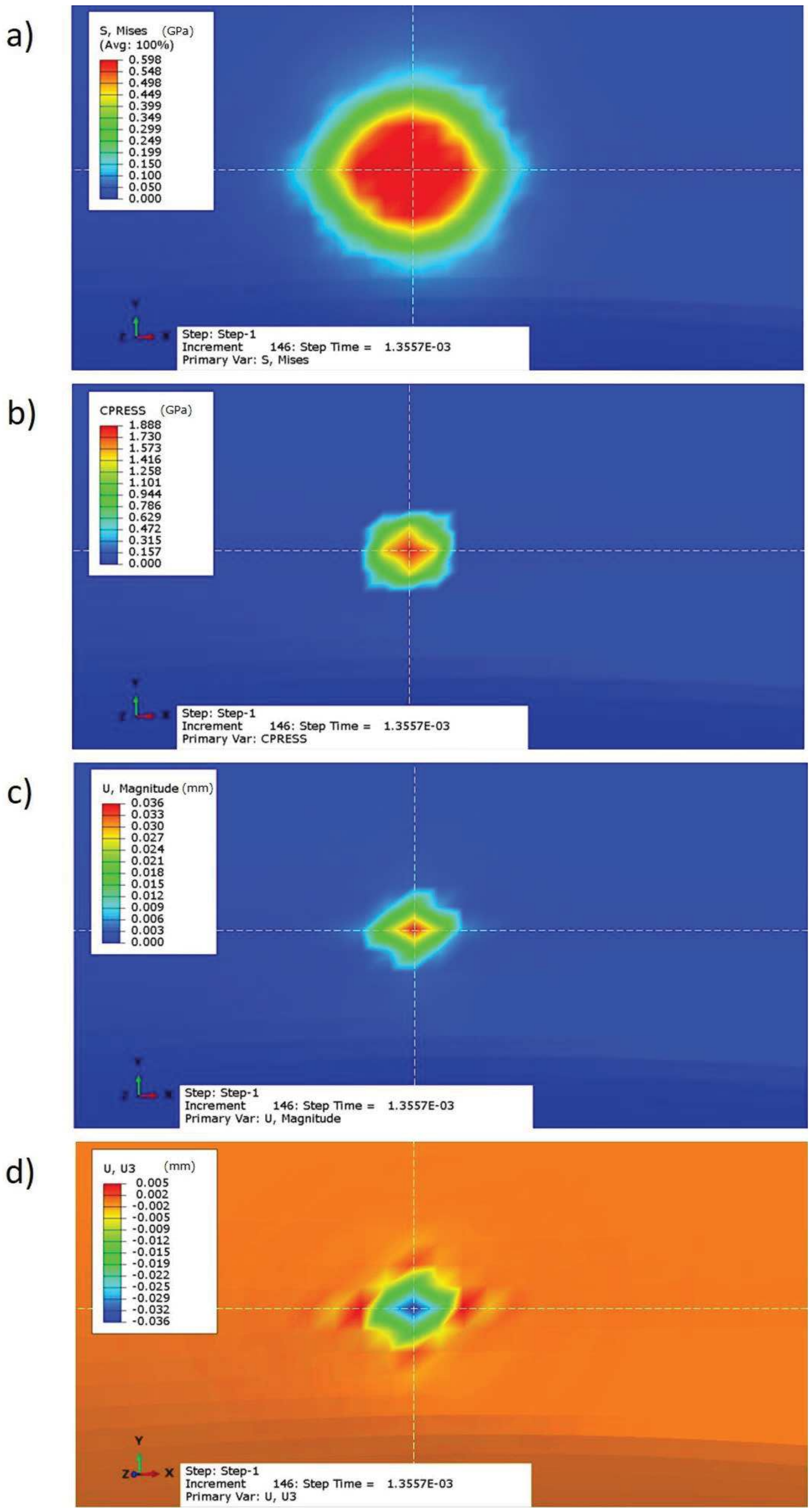

Figure 30 Normal impact – stresses and displacements at 0.00136 ms: a) von Mises; b) pressure; c) total displacement; d) displacement in z direction [149].

Figure 31 [149] shows the stresses and displacements induced by the normal impact in the minimum cross section. The stresses in the x (S11), y (S22), z (S33) directions are respectively displayed in Figure 31a, Figure 31b and Figure 31c. The shear stress in the yz plane (S23) is shown in Figure 31d. The other shear components of the stress tensor are not shown because they are very small. The composition of the stresses gives the von Mises stress field shown in Figure 31e. The total displacement, U, is shown in Figure 31f. The arrows identify the direction of impact. The stress and displacement distributions are symmetrical about the xz plane, as expected. There are only normal stresses near the contact surface, similar to the general elastic solution for stresses originating from a contact pressure [154].

Attention is now focused on the residual axial stresses, S11 in Figure 31. The rotating bending fatigue test performed after the impact induces stresses in this direction which vary over time. The overlap of these two axial stresses provides the final stress state in the minimum cross section of the specimen during the test. For this reason, it is important to identify the most stressed regions of the section.

As shown in Figure 31, modest tensile axial stresses are found in a small area close to the crater rim. The highest axial stresses are located between the crater rim and the direction normal to the impact direction. This area is roughly defined by the angular position $9.0° \leq \theta \leq 45.0°$. The angular position θ is measured from the point with the highest (positive) y coordinate and it is positive counterclockwise. The distribution of the axial stresses found is in agreement with the outcomes presented by Boyce et al. [119]. The axial stresses induced by the normal impact are shown in the graphs of Figure 32 and Figure 33 [149]. In detail, Figure 32 displays the axial stresses in the area $9.0° \leq \theta \leq 45.0°$ while Figure 33 reports the stresses at $\theta=0°$, $\theta=90°$ and in the direction passing through the center of the minimum cross section and the tip of the bulge, $\theta=67.5°$. The region close to this point is very critical because it experiences the highest tangential relative displacements [155-157]. Here the contact pressure is zero and for this reason relative displacement is probable for any coefficient of friction. The diagrams shown in Figure 32 and Figure 33 show the axial stress as a function of r_{final}-to-r ratio, with r_{final} the radial position measured on the deformed section and r the initial radius. It was chosen to use this ratio as independent variable to appreciate the radial deformation of the section. In case of radial expansion, r_{final}-to-r ratio is greater than 1. In Figure 32, the residual stresses plotted refer only to the nodes in the annulus of the minimum section. The maximum residual axial stress is at θ=18.0° and is roughly equal to 185 MPa (Figure 32). Since the considered problem is symmetrical with respect to the xz plane, this value of stress is reached also at θ=162.0°. The maximum residual axial stress on the vertical radius is about 130 MPa, while the maximum stress at θ=67.5° is about 100 MPa (Figure 33). The latter value of stress is also reached at θ=112.5°. The diagram of Figure 33 clearly shows the symmetry of the stresses on the vertical radius with respect to the z axis.

The residual axial stresses induced by the impact were superposed with the typical linear elastic distribution of axial stresses induced by a bending moment. A rotating bending fatigue test was considered. In a rotating bending test, the moment direction changes over time. Therefore, all points of the minimum cross section are subject to varying axial stresses. In general, a fatigue crack is more likely to nucleate where the maximum tensile residual stresses are. The maximum stress in the section during the fatigue test is consequently found when the maximum residual stress overlaps the maximum tensile stress induced by the test. In detail, the stresses plotted in Figure 32 and Figure 33 were superposed with the bending stresses induced by a moment of 1.5 Nm. This value was based on the results of the experiments on smooth hourglass specimens in 7075-T6 described in Section 3 of this thesis, considering in part the contribution of the crater generated by the impact. In a rotating bending test, all points of the sample section undergo a time-varying stress. The maximum value of the total stress in a point of the section is given by the sum of the residual stresses with the bending stresses in magnitude; the minimum value is given by the subtraction of the bending stresses in magnitude from the axial stresses. The result of the superposition of the residual with the bending stresses at the angular positions considered in Figure 32, 9.0°≤θ≤45.0°, are reported in Figure 34 [149]. In order to improve its readability, Figure 34 shows the results for the angular positions corresponding to the three highest stresses, i.e. 13.5°≤θ≤22.5°. The maximum total stress (tensile in nature) in this area is about 305 MPa and lies at θ=18.0° and, by symmetry, at θ=162.0°. Figure 35 [149] shows the result of the superposition of the bending stresses with the residual stresses in the angular positions considered in Figure 33, θ=0.0°, 67.5°, 90.0°. A maximum total stress of about 255 MPa (tensile) is reached on the vertical radius, both in the case of addition and subtraction of stresses. The two curves with square markers, i.e. residual + bending stresses and residual – bending stresses are symmetrical with respect to the ordinate of the diagram of Figure 35. The residual stress curve at θ=0.0° is symmetrical with respect to the ordinate of the diagram. Subtracting the bending stresses on the vertical radius equals adding a stress distribution which is symmetrical with respect to the y axis. Therefore, the two considered curves of Figure 35 can also be obtained as the sum of two symmetrical curves. The result must therefore be symmetrical. A total stress of about 240 MPa (tensile) is found at θ=67.5° and θ=112.5°. As a consequence of the results reported in Figure 34 and Figure 35, it is possible to predict the fatigue crack initiation near the specimen surface, at θ=18.0°, where the maximum stress in the whole section is reached. As a precaution, it can be stated that fatigue cracks could initiate at 13.5°≤θ≤22.5°. This range contains the determined angle θ=18.0° but extends the area of possible nucleation because the results refer to FE analysis and therefore they are approximated. In the outer area corresponding approximately to θ=67.5°, the relative displacement associated with the induced stress concentration may induce crack nucleation.

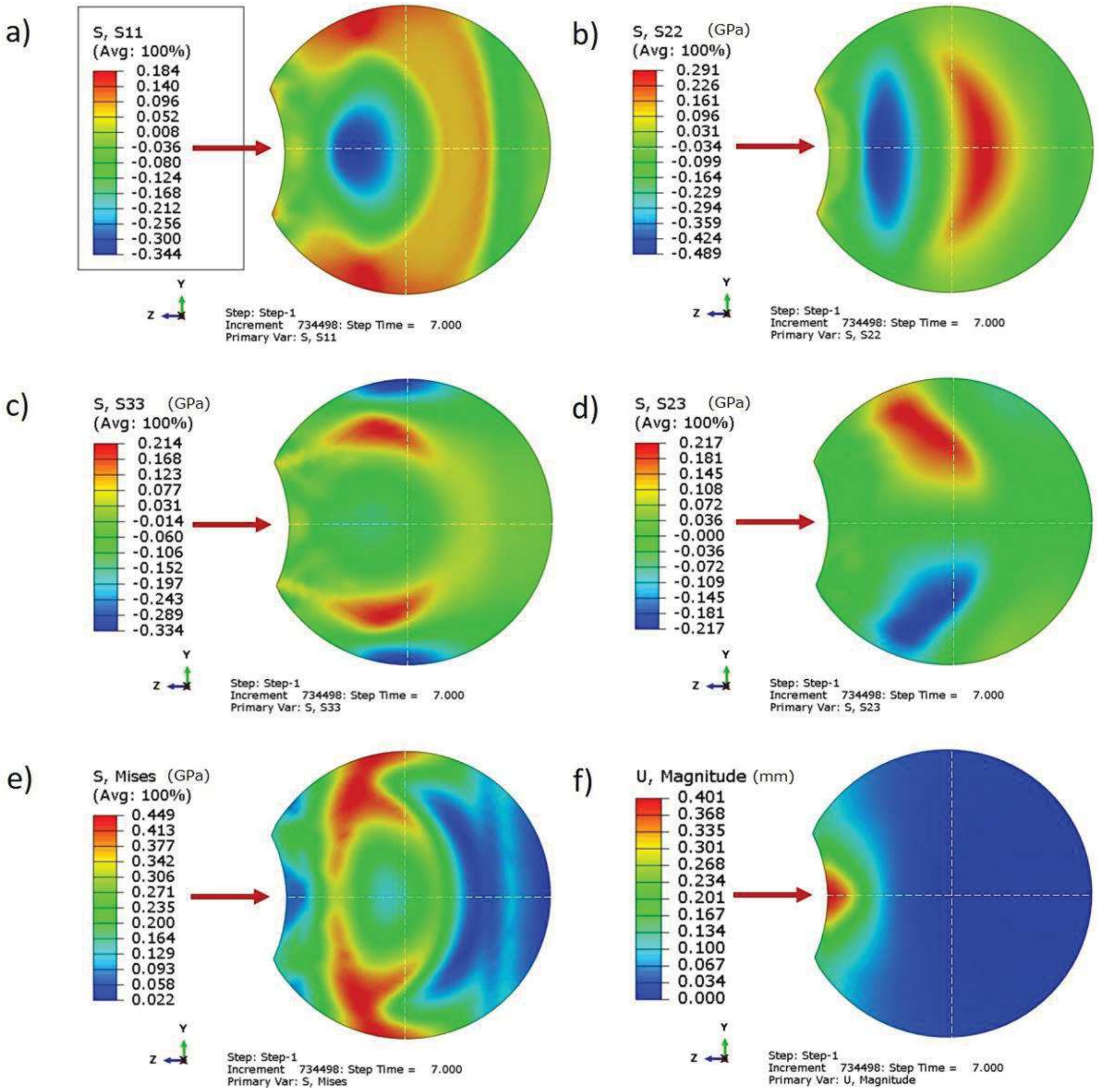

Figure 31 Normal impact – stresses and displacements at 7 ms: a) S11; b) S22; c) S33; d) S23; e) von Mises; f) total displacement [149].

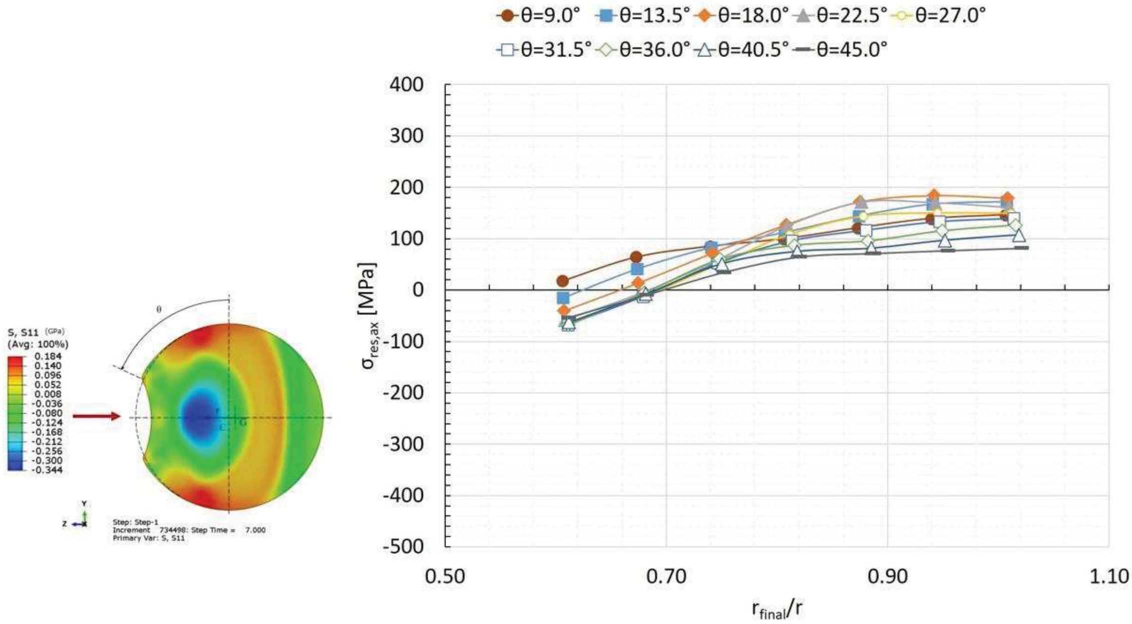

Figure 32 Normal impact – residual axial stresses, 9.0°≤θ≤45.0° [149].

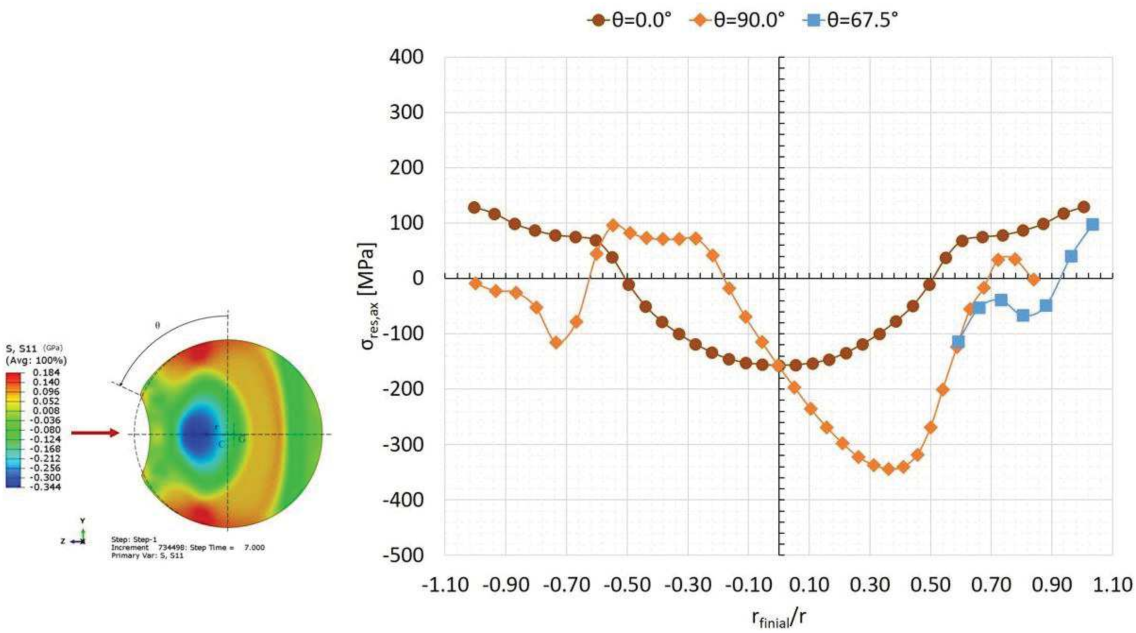

Figure 33 Normal impact – residual axial stresses, θ=0.0°, 67.5°, 90.0° [149].

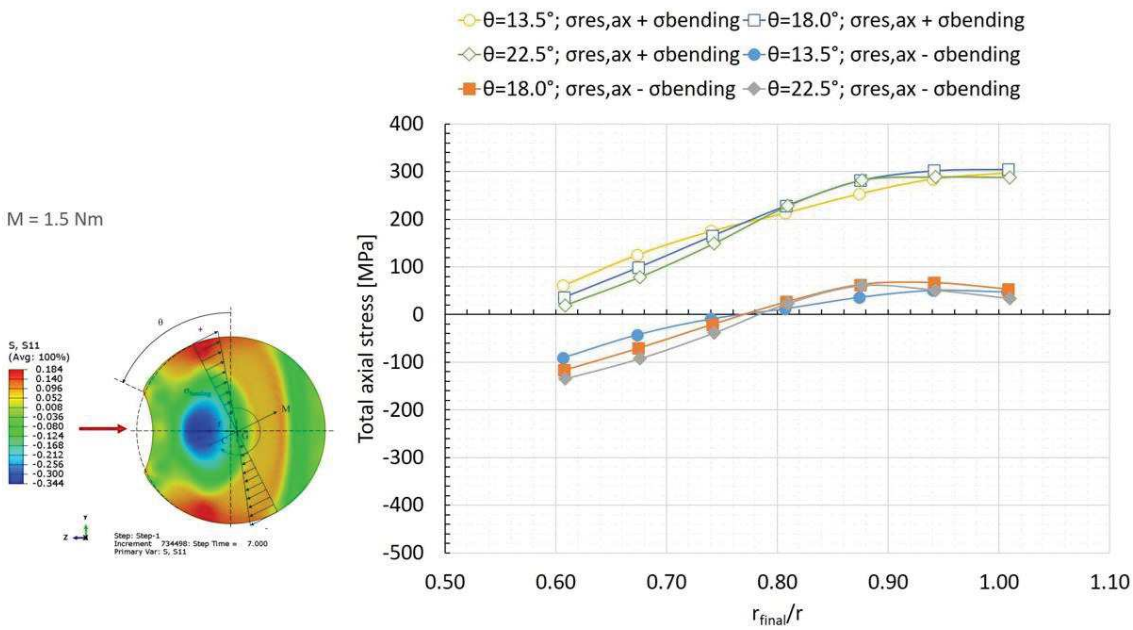

Figure 34 Normal impact – total axial stresses, 13.5°≤θ≤22.5° [149].

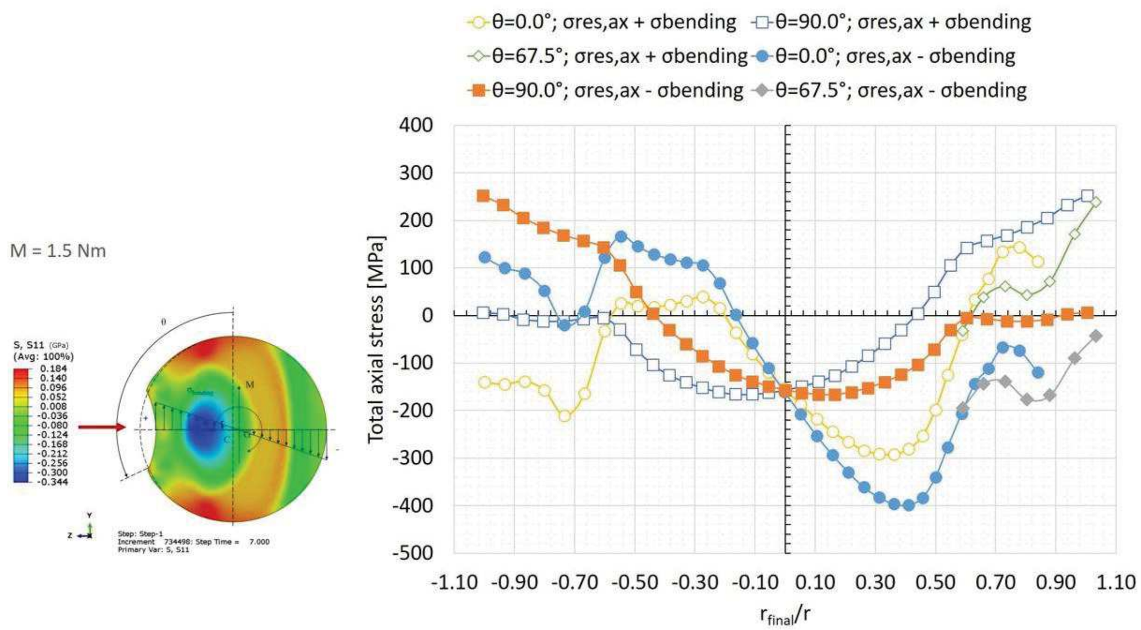

Figure 35 Normal impact – total axial stresses, θ=0.0°, 67.5°, 90.0° [149].

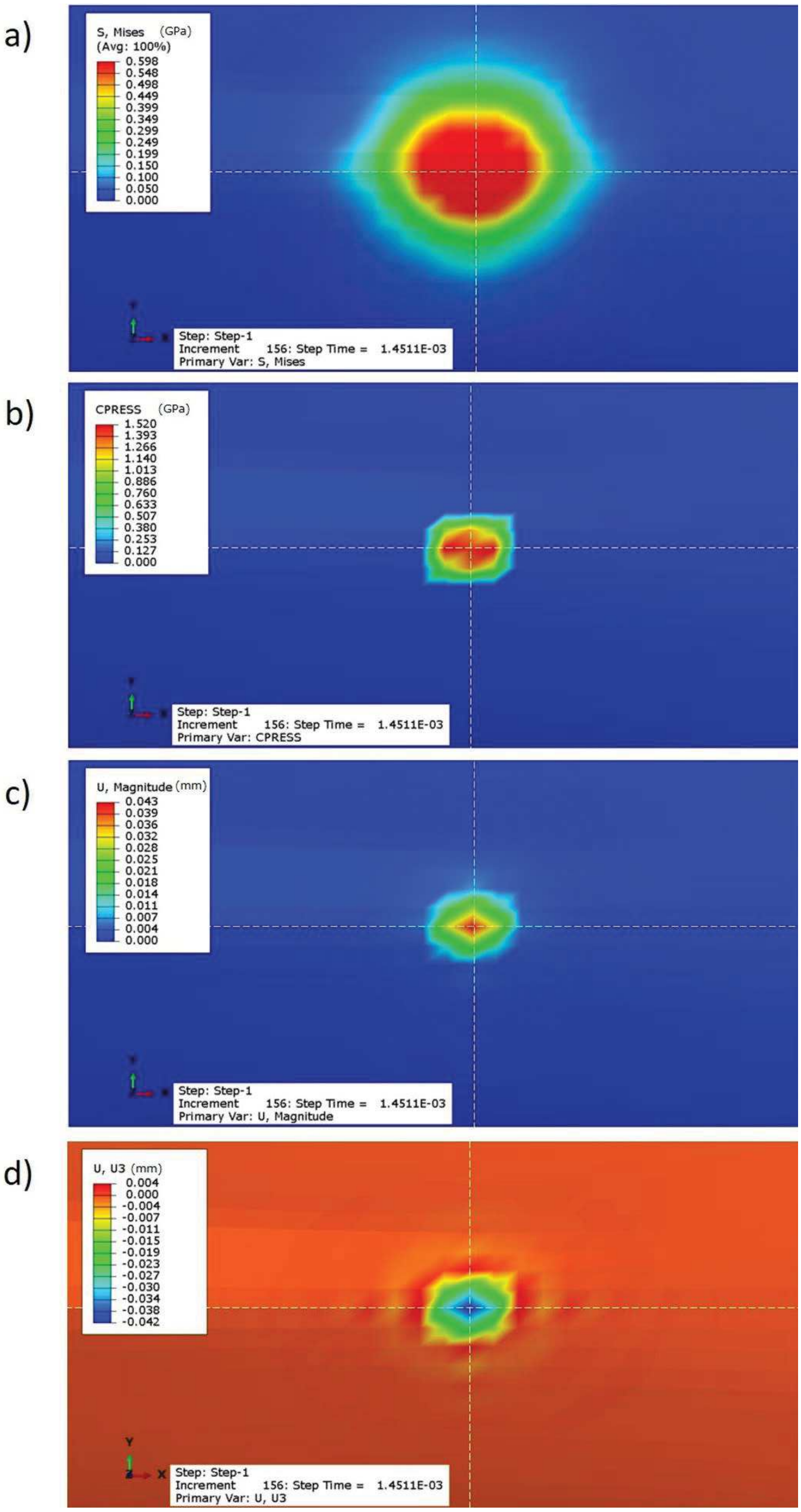

Figure 36 Oblique impact – stresses and displacements at 0.00145 ms: a) von Mises; b) pressure; c) total displacement; d) displacement in z direction [149].

4.2.2. Oblique impact

The same methodology was applied to assess the final stress distribution in the minimum cross section of an hourglass sample subject to oblique impact (case II) and tested by rotating bending.

Figure 36 [149] shows the contact stresses and displacements in this impact case. In detail, it illustrates the distributions of von Mises stress, contact pressure, displacement and displacement in the z direction. The direction of impact speed was on the plane yz. The speed of the sphere had two components, one directed as z, and the other directed as y. The angle of impact was very small, 10°, and for this reason the speed component in the z direction was much higher than the component in the y direction. For this reason, it was chosen to show the displacement in the z direction on the specimen. The figure refers to the time t= 0.00145 ms. At this time, the sample material is near yielding. Therefore, stresses and displacements can be considered elastic. The distributions obtained are symmetric with respect to the yz plane but they are not symmetric with respect to the xz plane. The asymmetry is clearly visible in the von Mises stress distribution, which shows a larger light blue area at the top. Contact stress and pressure are highest near the center of the contact region. Here, the magnitude of the displacement is maximum, as is the displacement in the z direction. The maxima of the fields are reached near the center of the area because the angle of impact was very small and for this reason the difference between the two impacts is not so evident with regards to contact analysis. Figure 36 points out that the maximum total displacement is not completely in the z direction, as expected. These distributions are therefore in agreement with the direction of the impact velocity.

Figure 37 [149] shows the stresses and displacements induced by the oblique impact in the minimum cross section: the stresses in the x (S11), y (S22), z (S33) directions are shown respectively in Figure 37a, Figure 37b and Figure 37c; the shear stress in the yz plane (S23) in Figure 37d; the von Mises stress in Figure 37e and the total displacement, U, in Figure 37f. As in the case I of normal impact, the other shear components of the stress tensor are negligible. The arrows in the figure identify the direction of impact.

According to Figure 37, the stress and displacement fields are not symmetrical with respect to the xz plane. The oblique impact induces a higher maximum stress overall: about 210 MPa versus about 185 MPa obtained in the case of normal impact. Figure 38, Figure 39 and Figure 40 [149] show the residual axial stresses at various angular positions. In detail, Figure 38 refers to $9.0°\leq\theta\leq45.0°$, i.e. the red area of Figure 37 in the upper section of the sample between the vertical radius and the crater. Figure 39 refers to $135.0°\leq\theta\leq171.0°$, i.e. the red area in the lower sample section between the crater and the vertical radius (Figure 37). Figure 40 refers to $\theta=0.0°$, $\theta=90.0°$ and the positions corresponding to the points at the end of the crater, $\theta=67.5°$ and $\theta=112.5°$. As it can be seen in Figure 37, the most stressed area of the upper section is closer to the crater than in the case I of normal impact. The maximum stress in this area, approximately equal to 205 MPa, is at $\theta=27.0°/31.5°$, Figure 38. In the case of normal impact, the most stressed node in the top of the section is at $\theta=18.0°$ and the stress is about 185 MPa (Figure 32). The area close to the crater can be subject to microstructural damage following the impact and it is therefore critical. The maximum stress of the whole section is about 210 MPa and it is reached at $\theta=162.0°$ (Figure 39), as in the case of the normal impact, where the stress is again about 185 MPa (Figure 32). The point of the crater rim in the lowest part of the section, corresponding to an angular position $\theta=112.5°$ is more stressed than the point located in the highest part, Figure 40. The maximum residual stress at $\theta=67.5°$ is about -5 MPa, with the nodes in this direction which are under compression; the maximum axial stress at $\theta=112.5°$ is about 150 MPa, reached on the sample surface.

Figure 41 [149] reports the outcomes of the superposition of the axial residual stresses with the bending stresses in the area $9.0°\leq\theta\leq45.0°$. Actually, the readability of the diagram is improved by plotting the stresses at $27.0°\leq\theta\leq36.0°$. In this area a maximum stress of approximately 335 MPa is reached over the time during the fatigue loading. This stress is 30 MPa more than that obtained in the case I of normal impact. The maximum moment in the considered area is reached in the exact position $\theta=27.0°/31.5°$. In the case of normal impact, the maximum stress is reached at $\theta=18.0°$ (Figure 34).

Figure 42 [149] shows the stresses resulting from the superposition of the FOD-induced stresses with the moment-induced stresses in the area 157.5°≤θ≤166.5°. In the lower part of the section, a maximum stress of about 335 MPa is reached at the position θ=162.0°. In the case of the application of a bending moment of 1.5 Nm, therefore, the two areas considered in the upper and lower part of the section undergo approximately the same maximum total axial stress, equal to about 335 MPa. Figure 43 [149] refers to the superposition of the stresses at θ=0.0°, θ=67.5°, θ=90.0° and θ=112.5°. The maximum total stress in the axial direction is found at θ=112.5° and is approximately 290 MPa.

Consequently, in case II of oblique collision, crack nucleation is probable at θ=27.0°/31.5°, θ=162.0° or at θ=112.5°. In the first two areas, the maximum stress of the entire section was reached over time, approximately 335 MPa. At θ=112.5°, high stress, about 290 MPa and relative displacement can be responsible for crack nucleation.

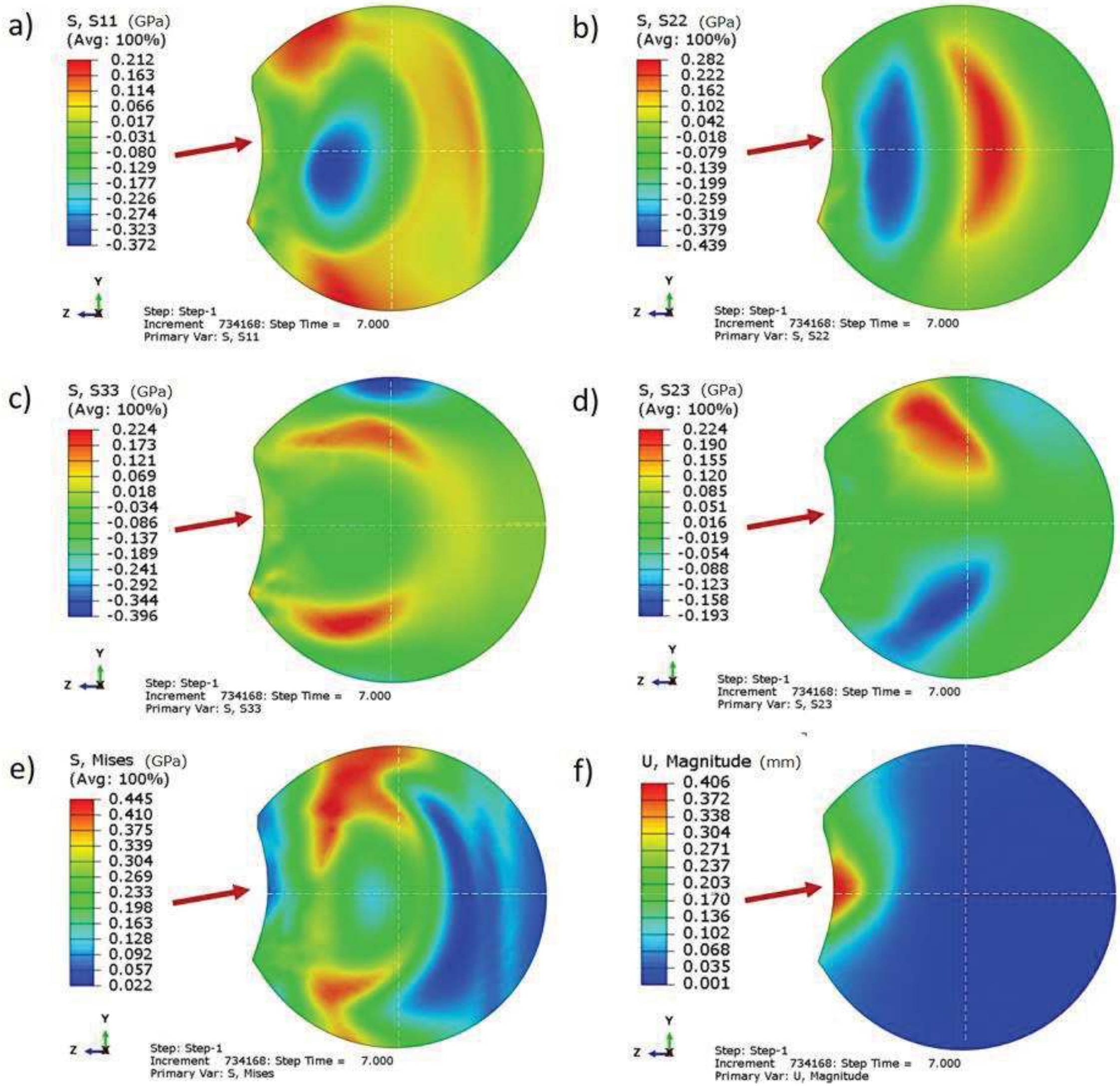

Figure 37 Oblique impact – stresses and displacements at 7 ms: a) S11; b) S22; c) S33; d) S23; e) von Mises; f) total displacement [149].

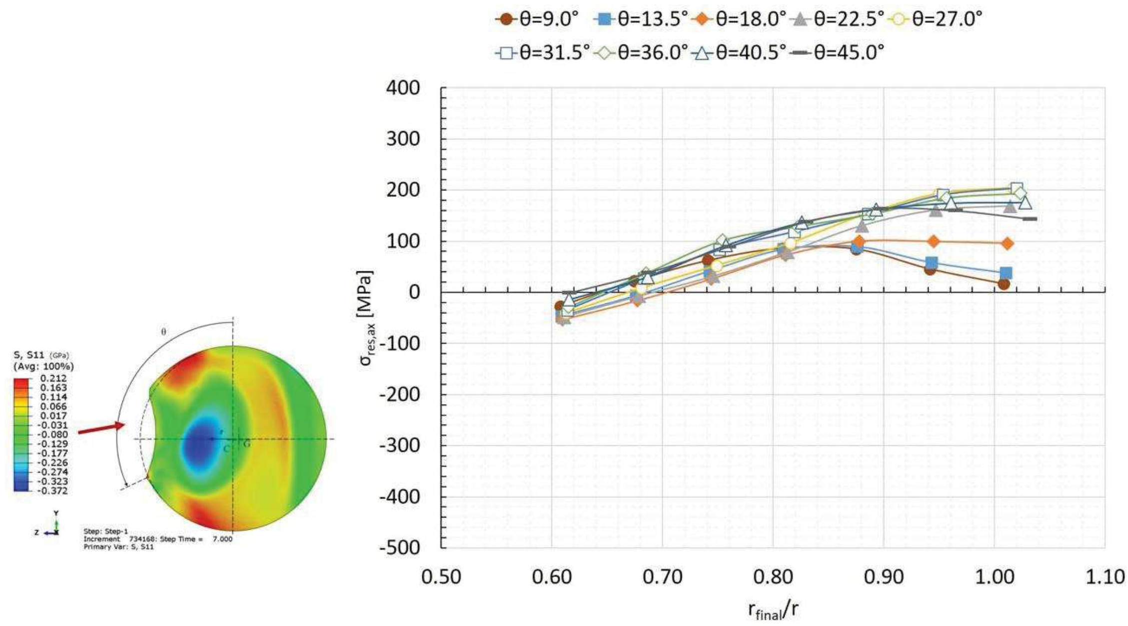

Figure 38 Oblique impact – residual axial stresses, 9.0°≤θ≤45.0° [149].

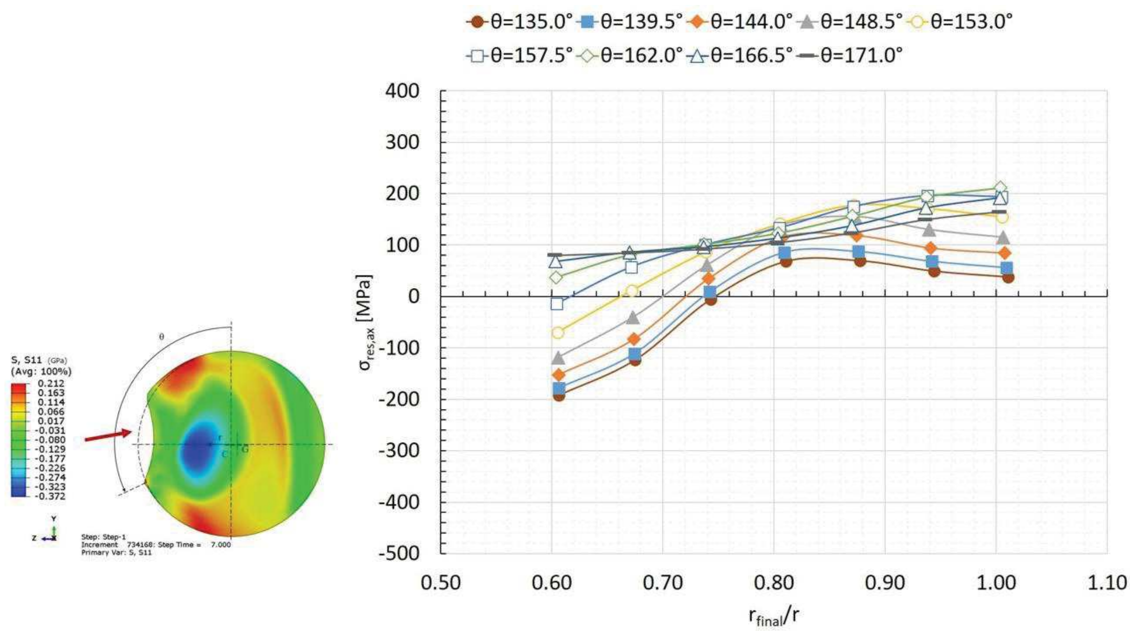

Figure 39 Oblique impact – residual axial stresses, 135.0°≤θ≤171.0° [149].

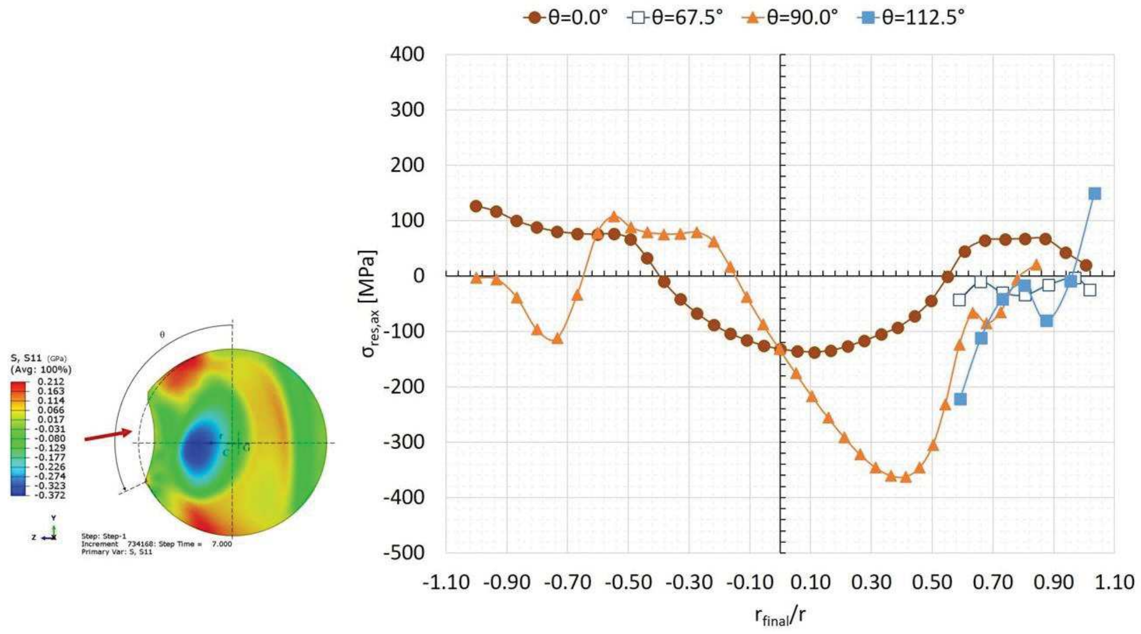

Figure 40 Oblique impact – residual axial stresses, θ=0.0°, 67.5°, 90.0°, 112.5° [149].

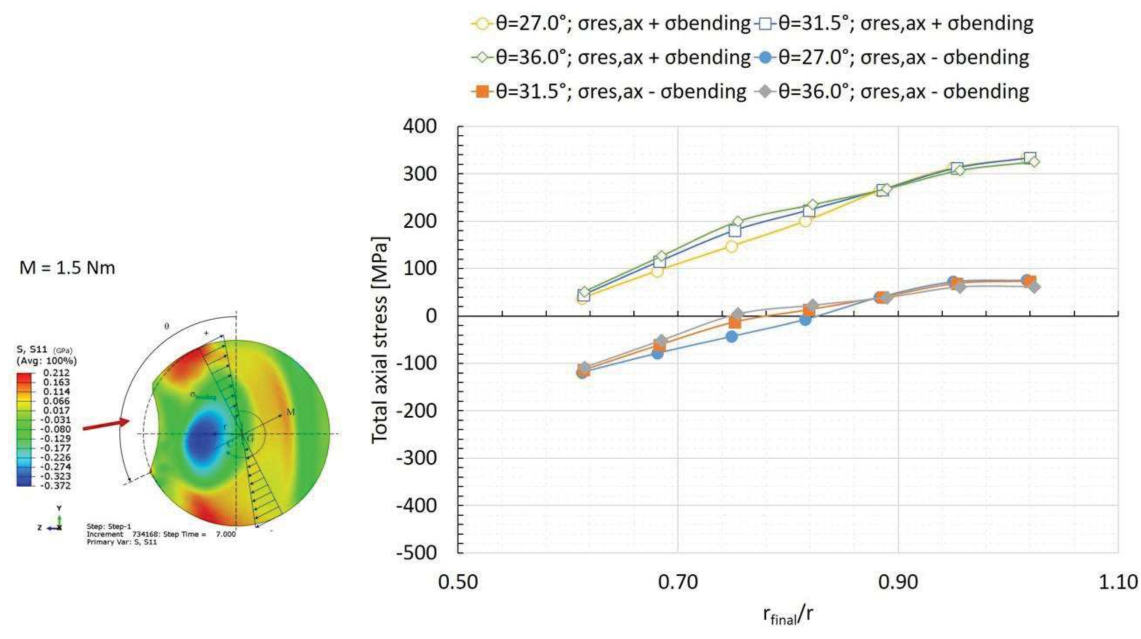

Figure 41 Oblique impact – total axial stresses, 27.0°≤θ≤36.0° [149].

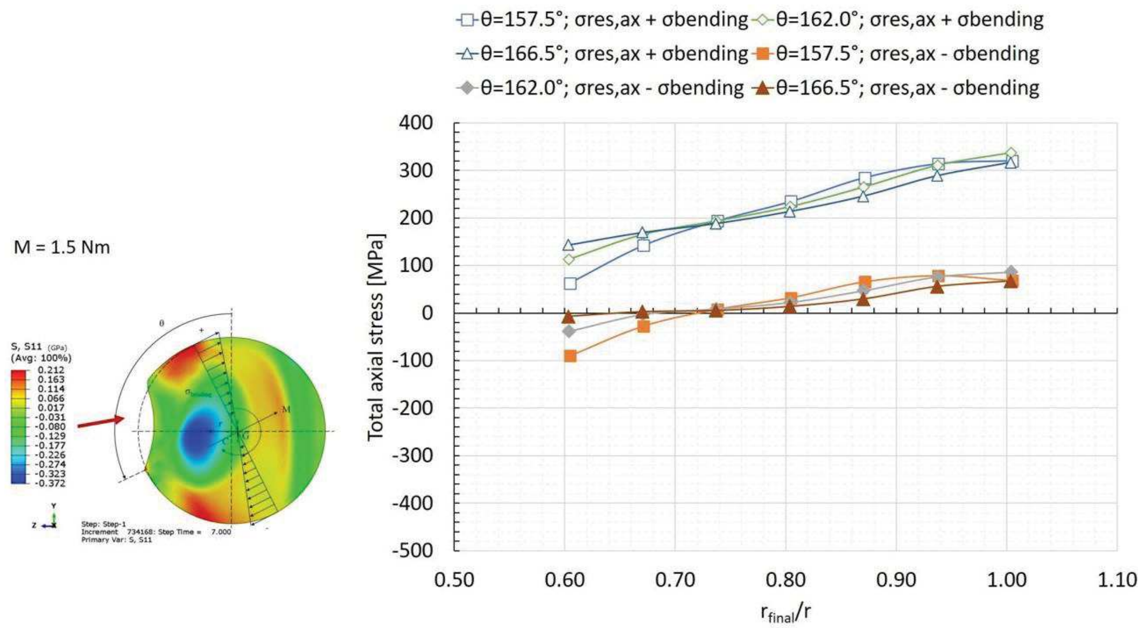

Figure 42 Oblique impact – total axial stresses, 157.5°≤θ≤166.5° [149].

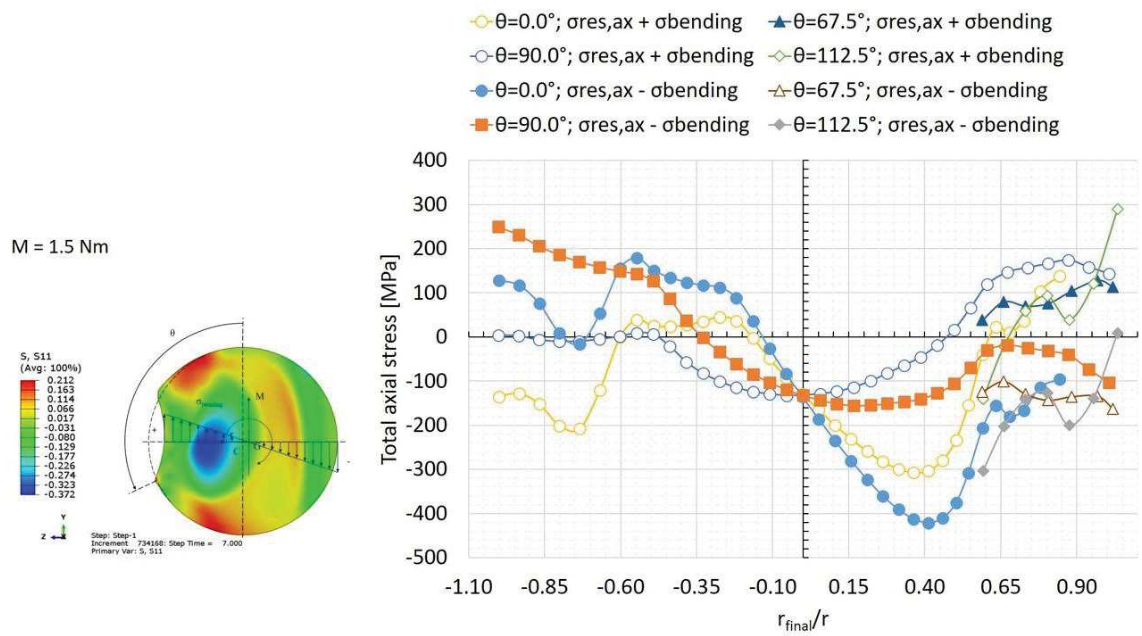

Figure 43 Oblique impact – total axial stresses, θ=0.0°, 67.5°, 90.0°, 112.5° [149].

4.3. Remarks

Table 6 FOD on 7075-T6: axial residual stresses and total stresses [149].

Stress [MPa]		Horizontal axis	Vertical axis	Crater rim		Between crater and vertical radius	
				up	down	up	down
Normal impact							
Axial		95	130	100	100	185	185
(position)		(90.0°)	(0.0°)	(67.5°)	(112.5°)	(18.0°)	(162.0°)
Total stress over time	Sum of stresses	145	250	240	240	305	305
	(position)	(90.0°)	(0.0°)	(67.5°)	(112.5°)	(18.0°)	(162.0°)
	Subtraction of stresses	165	250	-45	-45	65	65
	(position)	(90.0°)	(0.0°)	(67.5°)	(112.5°)	(18.0°)	(162.0°)
Oblique impact							
Axial		110	125	-5	150	205	210
(position)		(90.0°)	(0.0°)	(67.5°)	(112.5°)	(27.0°/31.5°)	(162.0°)
Total stress over time	Sum of stresses	140	175	130	290	335	335
	(position)	(90.0°)	(0.0°)	(67.5°)	(112.5°)	(27.0°/31.5°)	(162.0°)
	Subtraction of stresses	180	250	-100	10	75	85
	(position)	(90.0°)	(0.0°)	(67.5°)	(112.5°)	(27.0°/31.5°)	(162.0°)

Table 6 [149] summarizes the results of the stress analysis in the 7075-T6 hourglass samples subjected to a normal and oblique impact and the subsequent rotating bending fatigue test. The applied bending moment was 1.5 Nm. For the axial stresses, the maximum value obtained in the minimum cross section is reported. The maximum total axial stresses reported in the table are the maximum values obtained by adding the bending stresses to the residual ones and the maximum values found by subtracting the moment-induced stresses by the FOD-induced stresses. The values are reported for the section areas investigated: the horizontal axis, the vertical axis, the upper and lower edge of the crater rim and the two areas between the crater and the vertical radius. The angular position in which the values were found is indicated in parentheses.

The stress analysis made it possible to identify the most stressed areas, which are unfavorable from the point of view of fatigue. Cracks can initiate here, if the flaws are homogenously distributed in the sample. In the case of a normal impact, the cracks are expected to nucleate at the angular positions θ~18.0° and θ~162.0°, where the maximum stress of 305 MPa was detected. In these areas, the maximum axial residual stresses are found, 185 MPa. The outer areas at θ~67.5° and θ~112.5° are also critical. In these areas, the total axial stress is 240 MPa, but the relative tangential displacement can contribute to cracking. Since the analyzed problem is symmetrical with respect to the horizontal axis of the section, the areas identified are also symmetrical. The stress field induced by the oblique impact in the minimum cross section is not symmetrical with respect to the horizontal axis of the section even though the angle of impact is very small, 10°. In the upper part of the section, the most stressed area is located closer to the crater, while in the lower part it is located approximately in the same position of the normal impact. Considering only the total stress as the driving force for the nucleation of cracks, it was found that if the specimen is subjected to a rotating bending moment of 1.5 Nm after the oblique impact, the most critical areas are located at θ =27.0°/31.5° and θ=162.0°, where the maximum stress of about 335 MPa is reached. However, the cracks could also nucleate at θ=112.5°, at the lowest point of the crater rim. In this area, the maximum stress over time is 290 MPa but the relative tangential displacement could increase the probability of crack nucleation. Overall, the oblique impact induces higher tensile stresses than the normal one.

Some considerations can also be drawn regarding the magnitude of the stresses. The high tensile stresses induced by the FOD in both impact cases tested induce high total stresses in the fatigue test in some areas. The contribution of the residual stresses on the fatigue strength can be assessed by comparing the maximum stresses reached by the FOD samples with those reached by a smooth specimen when a rotating bending moment of

1.5 Nm is applied. In the latter case, the minimum cross section would be undeformed and the maximum bending stress would be around 120 MPa. The residual stresses would obviously be zero. Therefore, the maximum stresses reached over time by the two FOD specimens analyzed, 305 and 335 MPa, are respectively 2.5 and 2.8 times the maximum stress on the smooth specimen. These increases are attributable to the (residual) stresses induced by the FOD and to the decrease in the moment of inertia of the section, as a consequence of the impact. The maximum total stresses found are very high, if compared both to the UTS of the alloy and to the fatigue strength at very high number of cycles. For the latter, although aluminum alloys have no fatigue limit, a value equal to 0.33 times the UTS can be assumed as endurance limit of the alloy σ_{lim}. The following values were assumed: UTS=650 MPa and σ_{lim}=215 MPa. In the case of normal impact, the maximum total stress over time, 305 MPa is 0.5 times the UTS and 1.4 times the σ_{lim}. In the case of oblique impact, the maximum total stress over time, 335 MPa is 0.5 times the UTS and 1.6 times the σ_{lim}. The specimens can therefore be subjected to small bending moments. In case of high moments, the fatigue life of the specimens is low.

5. Conclusions and Future Developments

This thesis aims to improve the knowledge on the behavior of Ti-6Al-4V and 7075, which are two of the most common light alloys in the high performance sectors. Their strength was studied under quasi-static and fatigue loads in various environments. The effects of damages were also assessed. The characterization was performed by experimental tests, analysis of the fracture surfaces obtained and numerical models.

Quasi-static tests were performed on Ti-6Al-4V samples with various geometries in inert and corrosive environments. The aim was to characterize Ti-6Al-4V not subject to STOA. The lack of this treatment could reduce the cost of the components. The results showed that the presence of notches corresponding to Kt = 8.1 does not affect the strength of the alloy in inert environments. For the considered alloy, the combination of methanol and sharp notches provides detrimental effects, with a noticeable reduction in strength. Contamination of methanol with moisture reduces the aggressiveness of methanol. A macroscopic analysis of the fracture surfaces of the failed samples shows that methanol is responsible for brittle failure near the edges. Methanol and steep stress gradients induce crack initiations at the notches. The analysis pointed out the biphasic nature of the alloy, with an intermediate ductile/brittle behavior. The strength of the alloy was affected by strain rate and time of immersion in the aggressive environments.

A test campaign was conducted on 7075-T6 hourglass specimens, uncoated and coated with DLC. In detail, rotating bending fatigue tests were carried out and a step method was applied to assess the fatigue strength. Deposition of DLC was found to induce a remarkable reduction in fatigue strength in the range $2 \cdot 10^5 - 10^6$ cycles. In the range $2 \cdot 10^6 - 10^7$ cycles, the fatigue strength of the samples with DLC is similar to that of samples without DLC. Two regression models were proposed to fit the results found in the tested range of number of cycles. For specimens without DLC, linear regression might be suitable. Piecewise linear regression is suggested to define the fatigue strength of the DLC-coated samples. However, a high scatter of the experimental outcomes can be noted. Furthermore, as known, aluminum alloys have no fatigue limits and therefore some tests at higher cycles will help to identify the trend of the fatigue behavior for the coated samples in this fatigue regime. The failure mechanism was investigated by observing the fracture surfaces. A single crack initiation was observed in the DLC-coated specimens in the case of failure at low stress amplitudes. Multiple cracks nucleated in the sample failed at high stress amplitude, 290 MPa, and the extent of the overload failure area is almost the entire surface. The fracture surface obtained is typical of failure under stresses of high amplitude. The deposition process induces a residual stress field which is favorable from a fatigue point of view. Indeed, the total stress state on the surface in the fatigue tests is highly compressive. Consequently, crack nucleation is expected below the surface of the DLC-coated specimens, where the highest stresses, tensile in nature, are found. This aspect is confirmed by the observation of the fracture surfaces of the tested specimens. Crack initiation in the uncoated specimens takes place on the surface due to the steep stress gradient associated with the application of a bending load and any flaws introduced in polishing.

The effects of damages on 7075-T6 hourglass samples on their fatigue strength was investigated using numerical models. An hourglass sample was considered because of the type of fatigue test chosen to be performed after the impact and to consider a geometry which is more complex than the planar ones commonly present in the literature. The damage was induced by the impact of a steel sphere at the minimum cross section of the specimen. Two types of impact were studied, one normal and one oblique, with a small angle. The impacts induced a state of residual stresses which overlapped in the axial direction with the stress field generated by a rotating moment of 1.5 Nm. The residual stress field induced by the normal impact was symmetrical with respect to the impact direction, with the most stressed area located between the crater generated by the impact and the direction normal to the direction of the sphere's speed. Even though the angle of impact was small, the oblique impact induced greater stresses than in the normal case. The most stressed areas were still found between the crater and the vertical direction. However, the area in the upper part of the section was closer to the crater. As demonstrated by the superposition of the stresses, these identified areas are critical from a fatigue point of view, for both normal and oblique impact cases. In these areas, indeed, the maximum tensile stresses in the section and over time were reached. Crack nucleation is therefore very likely in these areas. However, also the areas in the section at the extremity of the crater are susceptible to cracking. Crack initiation is driven here by the high stresses found and the relative tangential displacements. The maximum stresses reached are very high and therefore the damage considered is very harmful for the fatigue strength of the specimens subjected to a rotating bending moment of 1.5 Nm.

It would be a great pleasure for the author of this thesis to continue with this stimulating research topic in following years. Several activities could be still carried out in the future.

First of all, the effects of applying coatings by PVD on Ti-6Al-4V without STOA could provide insight into the possibilities for improving the wear and corrosion resistance of the alloy. The contribution of these coatings to the static and fatigue strength should be determined.

Further tests with ultrasonic machines for the determination of high cycle fatigue strength of coated and uncoated 7075-T6 specimens will also reveal whether the strength of the coated specimens is higher than that of the uncoated ones in this fatigue regime, as suggested by the test results described in this thesis. In this case, the deposition of the coating will be able to improve corrosion resistance, tribological properties and fatigue strength at high numbers of cycles.

The FE model created for the study of the FOD can be used for further studies. For instance, it is possible to study the effects of multiple impacts in the same area and of various impact angles. The damage could be caused by the impact of particles of different shapes and materials. The contribution of these aspects is very interesting and will allow to identify which damages can be tolerated. The FE model can be improved to study the effects of FOD on coated samples. A final experimental test campaign would validate the results.

The final goal of the research, that could be achieved in the following years, is to introduce a new geometry of machine components that meets the typical needs of the nautical, aeronautical and racing sectors but can be suitable for all fields of mechanics. The geometry will consist of shells made of light alloys coated with thin hard layers. These innovative components will combine light masses with appreciable performance. The light masses will induce a reduction in fuel and energy consumption introducing eco-friendly components. The good strength of the components will be ensured in any environment, under any load, and in the presence of defects, which unfortunately always exist.

References

[1] Lütjering G., Williams J.C, Titanium, second edition, *Springer*, Berlin, 2007.

[2] Dimah M.K., Devesa Albeza F., Amigó Borrás, V., Igual Muñoz A., Study of the biotribocorrosion behavior of titanium biomedical alloys in simulated body fluids by electrochemical techniques, *Wear*, pp. 294–295, 409–418, 2012.

[3] Donachie M.J., *Titanium and titanium alloys source book*, American Society of Metals, *Metals Park*, 1982.

[4] Sergueeva A.V., Stolyarov V.V., Valiev R.Z., Mukherjee A.K., Superplastic behaviour of ultrafine-grained Ti–6Al–4V alloys, *Materials Science & Engineering A 323*, pp. 318-325, 2002.

[5] Gurrappa I., Characterization of titanium alloy Ti-6Al-4V for chemical, marine and industrial applications, *Materials Characterization 51*, pp. 131– 139, 2003.

[6] Brown B.F., Stress corrosion cracking in high-strength steels and in titanium and aluminum alloys, *Naval Research Laboratory*, Washington, D.C., pp. 147–244, 1972.

[7] Lee E.U., Vasudevan A.K., Sadananda K, Effects of various environments on fatigue crack growth in Laser formed and IM Ti-6AI-4V alloys, *International Journal of Fatigue 27*, pp. 1597-1607, 2005.

[8] Codaro E.N., Nakazato R.Z, Horovistiz A.L., Ribeiro L.M.F., Ribeiro R.B., Hein L.R.O., An image analysis study of pit formation on Ti-6Al-4V, *Materials Science and Engineering A 341*, pp. 202–210, 2003.

[9] Morrissey R.J., Nicholas T., Fatigue strength of Ti–6Al–4V at very long lives, *International Journal of Fatigue 27*, p.1608-1612, 2005.

[10] Lanning D.B., Nicholas T., Haritos G.K., On the use of critical distance theories for the prediction of the high cycle fatigue limit stress in notched Ti–6Al–4V, *International Journal of Fatigue 27*, pp. 45–57, 2005.

[11] Bellows, R.S., Muju, S., Nicholas, T., Validation of the step test method for generating Haigh diagrams for Ti-6Al-4V, *International Journal of Fatigue 21*, pp. 687-697, 1999.

[12] Peters J.O., Boyce B.L., Chen X., McNaney J.M., Hutchinsn J.W., Ritchie R.O., On the application of the Kitagawa–Takahashi diagram to foreign-object damage and high-cycle fatigue, *Engineering Fracture Mechanics 69,* pp. 1425–1446, 2002.

[13] Leuders S., Thöne M., Riemer A., Niendorf T., T. Tröster, H. A Richard, H. J. Maierad, On the mechanical behaviour of titanium alloy TiAl6V4 manufactured by selective laser melting: Fatigue resistance and crack growth performance, *International Journal of Fatigue 48*, pp. 300-307, 2013.

[14] Van Hooreweder B., Boonen R., Moens D., Kruth J.P., Sas P., On the determination of fatigue properties of Ti-6Al-4V produced by selective laser melting, *Collection of Technical Papers - AIAA/ASME/ASCE/AHS/ASC Structures, Structural Dynamics and Materials Conference*, 2012.

[15] Nalla R.K., Campbell J.P., Ritchie R.O., Effects of microstructure on mixed-mode, high-cycle fatigue crack-growth thresholds in Ti-6Al-4V alloy, *Fatigue & Fracture of Engineering Materials & Structures 25*, pp. 587-606, 2002.

[16] Seifi M., Salem A., Satko D., Shaffer J., Lewandowski J.J., Defect distribution and microstructure heterogeneity effects on fracture resistance and fatigue behavior of EBM Ti–6Al–4V, *International Journal of Fatigue 94*, pp. 263-287, 2017.

[17] Wojtaszek M., Sleboda T., Czulak A., Weber G., Hufenbach WA., Quasi-static and dynamic tensile properties of Ti-6Al-4V alloy, *Archives of Metallurgy and Materials 58*, pp. 1261-1265, 2013.

[18] Zhou W., Chew KG., The rate dependent response of a titanium alloy subjected to quasi-static loading in ambient environment, *Journal of Materials Science 37*, pp. 5159-5165, 2002.

[19] Proceedings of Conference – Fundamental aspects on stress corrosion cracking, September 11-15, Ohio (USA), ed. NACE, 1969.

[20] Blackburn MJ, Feeney JA, Beck TR. Stress-corrosion cracking of titanium alloys, In: Advances in Corrosion Science and Technology, vol. 3. New York: Plenum Press, pp. 67-292, 1973.

[21] Barella S., Mapelli C., Venturini R., Investigation about the stress corrosion cracking of Ti-6Al-4V, *Metallurgical Science and Technology 23*, pp. 19-26, 2005.

[22] Bursle A.J., Pugh E.N., An evaluation of current models for the propagation of stress-corrosion cracks, TMS Paper Selection, pp. 18-47, 1977.

[23] Sarioglu F., Doruk M., Elastic-plastic fracture mechanics analysis of SCC in a low strength steel, In: Proceedings of the 7th International Conference on Fracture (ICF7), Houston (Texas,), pp. 259-265, 20–24 March 1989.

[24] Johnston R.L., Johnson R.E., Ecord G.M., Castner W.L., Stress-corrosion cracking of Ti-6al-4V alloy in methanol, *NASA Technical Note TN D-3868*, 1967.

[25] Johnson R.E., NASA Experiences with Ti-6Al-4V in methanol, *DMIC Memorandum 228*, 1967.

[26] Sanderson G., Powell D.T., Scully J.C., The stress-corrosion cracking of Ti alloys in aqueous chloride solutions at room temperature, *Corrosion Science 8*, pp. 473–481, 1968.

[27] Dawson D., Pelloux R. M., Corrosion fatigue crack growth of titanium alloys in aqueous environments, *Metallurgical Transactions 5*, pp. 723-731, 1974.

[28] Lee T.M., Chang E., Yang C.Y., Effect of passivation on the dissolution behavior of Ti6Al4V and vacuum-brazed Ti6Al4V in Hank's ethylene diamine tetra-acetic acid solution Part I Ion release, *Journal of Materials Science: Materials in Medicine 10*, pp. 541-548, 1999.

[29] Gangloff R.P., Crack size effects on the chemical driving force for aqueous corrosion fatigue, *Metallurgical Transactions A 16*, pp. 953-969, 1985.

[30] Wang K., Wang F., Cui W., Hayat T, Ahmad B., Prediction of short fatigue crack growth of Ti-6Al-4V, *Fatigue & Fracture of Engineering Materials & Structures 37*, pp. 1075-1086, 2014.

[31] Anil M., Ahmed S.F., J.W. Yi, Moon M.W., Lee K.R., Kim Y.C., Seok H.K., Han S.H., Tribological Performance of hydrophilic diamond-like carbon coatings on Ti-6Al-4V in biological environment, *Diamond & Related Materials 19*, pp. 300–304, 2010.

[32] Yetim A.F., Celik A., Alsaran A., Improving tribological properties of Ti6Al4V alloy with duplex surface treatment, *Surface and Coatings Technology 205*, pp. 320–324, 2010.

[33] Arslan E., Totik Y., Demirci E.E., Efeoglu I., Wear and adhesion resistance of duplex coatings deposited on Ti6Al4V alloy using MAO and CFUBMS, *Surface and Coatings Technology 214*, pp. 1–7, 2013.

[34] Kao W.H., Su Y.L., Horng J.H., Huang H.C., The tribological performance of surface treated Ti6Al4V as sliding against Si3N4 ball and 316L stainless steel

cylinder, *Journal of Materials Engineering and Performance 25*, pp. 5209-5219, 2016.

[35] Meassick S., Champaign H., Noble metal cathodic arc implantation for corrosion control of Ti-6Al-4V, *Surface & Coatings Technology 93*, pp. 292-296, 1997.

[36] Zhou J., Bahadur S., Erosion-corrosion of Ti-6Al-4V in elevated temperature air environment, *Wear 186-187*, pp. 332-339, 1995.

[37] Arcieri E.V., Baragetti S., Corrosion fatigue behavior of Ti-6Al-4V: chemical and mechanical driving forces, *International Journal of Fatigue 112*, pp. 301-307, 2018.

[38] Baragetti S., Gerosa R., Villa F., Quasi-static behavior of notched Ti-6Al-4V specimens in water-methanol solution, *Corrosion Reviews 33*, pp. 477-485, 2015.

[39] Baragetti S., Villa F., Corrosion fatigue of high-strength titanium alloys under different stress gradients, *The Journal of the Minerals, Metals & Materials Society 67*, pp. 1154-1161, 2015.

[40] Baragetti S, Villa F., SCC and corrosion fatigue characterization of a Ti-6Al-4V alloy in a corrosive environment - experiments and numerical models, *Frattura ed Integrità Strutturale 8*, pp. 84-94, 2014.

[41] Baragetti S, Villa F., Crack propagation models: numerical and experimental results on Ti-6Al-4V notched specimens, *Fatigue & Fracture of Engineering Materials & Structures 40*, pp. 1276-83, 2016.

[42] Frost N. E., Dugdale D. S., Fatigue tests on notched mild steel plates with measurements of fatigue cracks, *Journal of the Mechanics and Physics of Solids 5*, pp. 182-192, 1957.

[43] Hirsch J. R., Aluminium in innovative light-weight car design, *Materials Transactions 52*, pp. 818-24, 2011.

[44] Lomolino S., Tovo R., dos Santos J., On the fatigue behaviour and design curves of friction stir butt-welded Al alloys, *International Journal of Fatigue 27*, pp-305-316, 2005.

[45] Baragetti S., D'Urso G., Aluminum 6060-T6 friction stir welded butt joints: fatigue resistance with different tools and feed rates, *Journal of Mechanical Science and Technology 28*, pp. 867-77, 2014.

[46] Kumar M., Sotirov N., Chimani C.M., Investigations on warm forming of AW-7020-T6 alloy sheet, *Journal of Materials Processing Technology 214*, pp. 1769-76, 2014.

[47] Starke E.A., Staley J.T., Application of modern aluminium alloys to aircraft, *Progress in Aerospace Sciences 32*, pp. 131–172, 1996.

[48] Aissani M., Gachi S., Boubenider F., Benkedda Y., Design and optimization of friction stir welding tool, *Materials and Manufacturing Processes 25*, pp. 1199–1205, 2010.

[49] Bahemmat P., Haghpanahi M., Besharati Givi M., Reshad Seighalani K., Study on dissimilar friction stir butt welding of AA7075-O and AA2024-T4 considering the manufacturing limitation, *The International Journal of Advanced Manufacturing Technology 59*, pp. 939–953, 2012.

[50] Singh R., Sharma C., Dwivedi D., Mehta N., Kumar P., The microstructure and mechanical properties of friction stir welded Al–Zn–Mg alloy in as welded and heat treated conditions, *Materials and Design 32*, pp. 682–687, 2011.

[51] Panigrahi S.K., Jayaganthan R., Effect of ageing on microstructure and mechanical properties of bulk, cryorolled, and room temperature rolled Al 7075 alloy, *Journal of Alloys and Compounds 509*, pp. 9609–9616, 2011.

[52] Leng L., Zhang Z.J., Duan Q.Q., Zhang P., Zhang Z.F., Improving the fatigue strength of 7075 alloy through aging, *Materials Science and Engineering A 73*8, pp. 24-30, 2018.

[53] Chan K.S., Roles of microstructure in fatigue crack initiation, *International Journal of Fatigue* 32, pp. 1428–1447, 2010.

[54] Chan K.S., Jones P., Wang Q.G., Fatigue crack growth and fracture paths in sand cast B319 and A356 aluminum alloys, *Materials Science & Engineering A 341*, pp. 18–34, 2003.

[55] ASM International, ASM Handbook.

[56] Wu S.D., Cheng W.Y., Yang J.H.C., Yang C.H., Liao S.Y., The corrosion protection study on inner surface from welding of aluminum alloy 7075-T6 hydrogen storage bottle*, International Journal of Hydrogen Energy 41*, pp. 570-596, 2016.

[57] Silva G., Rivolta B., Gerosa R., Derudi U., Study of the SCC behavior of 7075 aluminum alloy after one-step aging at 163 °C, *Journal of Materials Engineering and Performance 22*, pp. 210–214, 2013.

[58] Sankaran K. K., Perez R., Jata K. V., Effects of pitting corrosion on the fatigue behavior of aluminum alloy 7075-T6: modeling and experimental studies, *Materials Science and Engineering A 297,* pp. 223–229, 2001.

[59] Zupanc U., Grum J., Effect of pitting corrosion on fatigue performance of shot-peened aluminium alloy 7075-T651, *Journal of Materials Processing Technology 210*, pp. 1197-1202, 2010.

[60] Savas T.P., Earthman J.C., Fatigue crack nucleation studies on sulfuric acid anodized 7075-T73 aluminum, *Journal of Materials Engineering and Performance 23*, pp. 2131–2138, 2014.

[61] Baragetti S., Srinivasan N., Bhaskar L.K., Kumar R., Influence of Environment, Residual stresses on the fatigue behavior of 7075-T6 aluminum alloy, *Key Engineering Materials 754*, pp. 3-6, 2017.

[62] Baragetti S., Gerosa R., Villa F., Physical vapour deposition of diamond like carbon coatings on a 7075-T6 substrate for corrosion protection at long and short fatigue lives, *International Journal of Structural Integrity 8*, pp. 576-584, 2017.

[63] Rahmat M.A., Oskouei R.H., Ibrahim R.N., Raman R.K.S., The effect of electroless Ni–P coatings on the fatigue life of Al 7075-T6 fastener holes with symmetrical slits, *International Journal of Fatigue 52*, pp. 30–38, 2013.

[64] Oskouei R.H., Ibrahim R.N., Barati M.R., An experimental study on the characteristics and delamination of TiN coatings deposited on Al 7075-T6 under fatigue cycling, *Thin Solid Films 526*, pp. 155–162, 2012.

[65] Puchi-Cabrera E.S., Staia M.H., Lesage J., Gil L., Villalobos-Gutiérrez C, La Barbera-Sosa J, Ochoa-Pérez EA, Le Bourhis E., Fatigue behavior of AA7075-T6 aluminum alloy coated with ZrN by PVD, *International Journal of Fatigue 30*, pp. 1220–1230, 2008.

[66] Oskouei R.H., Ibrahim R.N., Restoring the tensile properties of PVD-TiN coated Al 7075-T6 using a post heat treatment, *Surface and Coatings Technology 205,* pp. 3967–3973, 2011.

[67] Creus J., Mazille H., Idrissi H., Porosity evaluation of protective coatings onto steel, through electrochemical techniques, *Surface and Coatings Technology 130*, pp. 224–232, 2000.

[68] Liu C., Leyland A., Bi Q., Matthews A., Corrosion resistance of multi-layered plasma-assisted physical vapour deposition TiN and CrN coatings, *Surface and Coatings Technology 141*, pp. 164–173, 2001.

[69] Ahn S.H., Yoo J.H., Choi Y.S., Kim J.G., Han J.G., Corrosion behavior of PVD-grown WC–(Ti1−xAlx)N films in a 3.5% NaCl solution, *Surface and Coatings Technology 162*, pp. 212–221, 2003.

[70] Håkansson G., Sundgren J.-E., McIntyre D., Greene J., Münz W.-D, Microstructure and physical properties of polycrystalline metastable Ti0.5Al0.5N alloys grown by dc magnetron sputter deposition, *Thin Solid Films 153*, pp. 55–65, 1987.

[71] McIntyre D., Greene J., Håkansson G., Sundgren J.E., Münz W.D., Oxidation of metastable single-phase polycrystalline Ti0.5Al0.5N films: kinetics and mechanisms, *Journal of Applied Physics 67*, pp. 1542–1553, 1990.

[72] Bashir M.I., Shafiq M., Naeem M., Zaka-ul-Islam M., Díaz-Guillén J.C., Lopez-Badillo C.M., Zakaullah M., Enhanced surface properties of aluminum by PVD-TiN coating combined with cathodic cage plasma nitriding, *Surface & Coatings Technology 327*, pp. 59-65, 2017.

[73] Erdemir A., Donnet C., Tribology of diamond-like carbon films: recent progress and future prospects, *Journal of Physics D Applied Physics 39*, R311–R327, 2006.

[74] Grill A., Review of the tribology of diamond-like carbon, *Wear 168*, pp. 143-153, 1993.

[75] Robertson J., Diamond-like amorphous carbon, *Materials Science and Engineering: R 37*, pp. 129-281, 2002.

[76] Hauert R., An overview on the tribological behavior of diamond-like carbon in technical and medical applications, *Tribology International 37*, pp. 991-1003, 2004.

[77] Kim J.D., Kang Y.H., High-spend machining of aluminium using diamond endmills, *International Journal of Machine Tools and Manufacture 37*, pp. 1155-1165, 1997.

[78] Gåhlin R., Larsson M., Hedenqvist P., ME-C:H coatings in motor vehicles, *Wear 249*, pp. 302-309, 2001.

[79] Coldwell H.L., Dewes R.C., Aspinwall D.K., Renevier N.M., Teer D.G., The use of soft/lubricating coatings when dry drilling BS L168 aluminium alloy, *Surface and Coatings Technology 177-178*, pp. 716-726, 2004.

[80] Fukui H., Okida J., Omori N., Moriguchi H., Tsuda K., Cutting performance of DLC coated tools in dry machining aluminum alloys, *Surface & Coatings Technology 187*, pp. 70-76, 2004.

[81] Li F., Zhang S., Kong J., Zhang Y., Hang W., Multilayer DLC coatings via alternating bias during magnetron sputtering, *Thin Solid Films 519*, pp. 4910–4916, 2011.

[82] Sheeja D., Tay B.K., Lau S.P., Shi X., Ding X., Structural and tribological characterization of multilayer ta-C films prepared by filtered cathodic vacuum arc with substrate pulse biasing, *Surface & Coatings Technology 132,* pp. 228-232, 2000.

[83] Benchikh N., Garrelie F., Donnet C., Bouchet-Fabre B., Wolski K., Rogemond F., Loir A.S., Subtil J.L., Nickel-incorporated amorphous carbon film deposited by femtosecond pulsed laser ablation, *Thin Solid Films 482*, pp. 287–292, 2005.

[84] Wang A.Y., Lee K.R., Ahn J.P., Han J.H., Structure and mechanical properties of W incorporated diamond-like carbon films prepared by a hybrid ion beam deposition technique, *Carbon 44*, pp. 1826–1832, 2006.

[85] Singh S.V., Zaharia T., Creatore M., Groenen R., Van Hege K., Van de Sanden M.C.M., Hard graphitelike hydrogenated amorphous carbon grown at high rates by a remote plasma, *Journal of Applied Physics 107*, pp. 013305–013314, 2010.

[86] Ilyuschenko A.Ph., Feldshtein E.E., Lisovskaya Y.O., Markova L.V., Andreyev M.A., Lewandowski A., On the properties of PVD coating based on nanodiamond and molybdenum disulfide nanolayers and its efficiency when drilling of aluminum alloy, *Surface and Coatings Technology 270*, pp. 190-195, 2015.

[87] Bouzakis K.-D., Michailidis N., Skordaris G., Bouzakis E., Biermann D., M'Saoubi R., Cutting with coated tools: Coating technologies, characterization methods and performance optimization, *Manufacturing Technology 61*, pp. 703–723, 2012.

[88] Gredelj S., Kumar S., Gerson A.R., Cavallaro G.P., Radio frequency plasma nitriding of aluminium at higher power levels, *Thin Solid Films 515*, pp. 1480–1485, 2006.

[89] Hetzner H., Schmid C., Tremmel S., Durst K., Wartzack S., Empirical-statistical study on the relationship between deposition parameters, process variables, deposition rate and mechanical properties of a-C: H: W coatings, *Coatings 4*, pp. 772-795, 2014.

[90] Su Y.L., Kao W.H., Optimum Me-DLC coatings and hard coatings for tribological performance, *Journal of Materials Engineering and Performance 9*, pp. 38-50, 2000.

[91] Qi Y., Konca E., Alpas A. T., Atmospheric effects on the adhesion and friction between non-hydrogenated diamond-like carbon (DLC) coating and aluminum – A first principles investigation, *Surface Science 600*, pp. 2955-2965, 2006.

[92] Donnet C., Recent progress on the tribology of doped diamond-like and carbon alloy coatings: a review, *Surface and Coatings Technology 100–101*, pp. 180-186, 1998.

[93] Donnet C., Fontaine J., Grill A., Le Mogne T., The role of hydrogen on the friction mechanism of diamond-like carbon films, *Tribology Letters 9*, pp. 137-142, 2001.

[94] Oliver W.C., Pharr G.M., An improved technique for determining hardness and elastic modulus using load and displacement sensing indentation experiments, *Journal of Materials Research 7*, pp. 1564-1583, 1992.

[95] Qi Y., Hector L. G., Hydrogen effect on adhesion and adhesive transfer at aluminum/diamond interfaces, *Physical Review B 68,* 201403(R), 2003.

[96] Li X., Sun L., Guo P., Ke P., Wang A., Structure and residual stress evolution of Ti/Al, Cr/Al or W/Al co-doped amorphous carbon nanocomposite films: Insights from ab initio calculations, *Materials and Design 89*, pp. 1123–1129, 2016.

[97] Strondl C., Carvalho N.M., De Hosson J.Th.M., van der Kolka G.J., Investigation on the formation of tungsten carbide in tungsten-containing diamond like carbon coatings, *Surface & Coatings Technology 162*, pp. 288-293, 2003.

[98] Wang D.-Y., Chang W.-Y. Ho C.-L., Oxidation behavior of diamond-like carbon films, *Surface and Coatings Technology 120-121*, pp. 138-144, 1999.

[99] Yang W.J., Choa Y.-H., Sekino T., Shim K.B., Niihara K., Auh K. H., Thermal stability evaluation of diamond-like nanocomposite coatings, *Thin Solid Films 476*, pp. 49-54, 2003.

[100] Azzi M., Paquette M., Szpunar J.A., Klemberg-Sapieha J.E., Martinu L., Tribocorrosion behaviour of DLC-coated 316L stainless steel, *Wear 267*, pp. 860–866, 2009.

[101] Zhao G., Aune R.E., Espallargas N., Tribocorrosion studies of metallic biomaterials: the effect of plasma nitriding and DLC surface modifications, *Journal of the Mechanical Behavior of Biomedical Materials 63*, pp. 100–114, 2016.

[102] Pu J., Wang J., He D., Wan S., Corrosion and tribocorrosion behaviour of superthick diamond-like carbon films deposited on stainless steel in NaCl solution, *Surface and Interface Analysis 48*, pp. 360–367, 2016.

[103] Bayon R., Igartua A., Gonzalez J.J., Ruiz de Gopegui U., Influence of the carbon content on the corrosion and tribocorrosion performance of Ti-DLC coatings for biomedical alloys, Tribology International 88, pp. 115–125, 2015.

[104] Zeng A., Liu E., Zhang S., Tan S.N., Hing P., Annergren I.F., Gao J., Impedance study on electrochemical characteristics of sputtered DLC films, *Thin Solid Films 426*, pp. 258-264, 2003.

[105] Depner U., Ellermeier J., Troßmann T., Berger C., Oechsner M., The effect of layer structure on corrosion and erosion resistance of thin PVD multilayer films, *International Journal of Materials Research 08*, pp. 1014-1020, 2011.

[106] Kim H.-G., Ahn S.-H., Kim J.-G., Park S.J., K.-R. Lee, Electrochemical behavior of diamond-like carbon films for biomedical applications, *Thin Solid Films 475*, pp. 291-297, 2005.

[107] Uematsu Y., Tokaji K., Takekawa H., Effect of thick DLC coating on fatigue behaviour of magnesium alloy in laboratory air and demineralised water, *Fatigue & Fracture of Engineering Materials & Structures 33*, pp. 607-616, 2010.

[108] Bobzin K., Bagcivan N., Theiß S., Weiß R., Depner-Miller U., Troßmann T., Ellermeier J., Oechsner M., Behavior of DLC coated low-alloy steel under tribological and corrosive load: Effect of top layer and interlayer variation, *Surface and Coatings Technology 215*, pp. 110-118, 2013.

[109] Srinivasan N., Bhaskar L.K., Kumar R., Baragetti S., Residual stress gradient and relaxation upon fatigue deformation of diamond-like carbon coated aluminum alloy in air and methanol environments, *Materials & Design 160*, pp. 303-312, 2018.

[110] Schaufler J., Durst K., Haas T., Nolte R., Höppel H.W., Göken M., The influence of hydrogenated amorphous carbon coatings (a-C:H) on the fatigue life of coated steel specimens, *International Journal of Fatigue 37*, pp-1-7, 2012.

[111] Liu E., Li L., Blanpain B., Celis J. P., Residual stresses of diamond and diamond-like carbon films, *Journal of Applied Physics 98*, 073515, 2005.

[112] Nicholas T., High Cycle Fatigue, Elsevier Science Ltd (Oxford), 2006.

[113] Lin B., Zabeen S., Tong J., Preuss M., Whiters P. J., Residual stresses due to foreign object damage in laser-shock peened aerofoils: Simulation and measurement, *Mechanics of Materials 82*, pp. 78-90, 2015.

[114] Peters J. O., Ritchie R.O., Influence of foreign-object damage on crack initiation and early crack growth during high-cycle fatigue of Ti–6Al–4V, *Engineering Fracture Mechanics 67*, pp. 193-207, 2000.

[115] Ding J., Hall R. F., Byrne J., Tong J., Fatigue crack growth from foreign object damage under combined low and high cycle loading. Part I: Experimental studies, *International Journal of Fatigue 29*, pp. 1339-1349, 2007.

[116] Martinez C.M., Eylon D., Nicholas T., Thompson S.R., Ruschau J.J., Birkbeck J., Porter W.J., Effects of ballistic impact damage on fatigue crack initiation in Ti–6Al–4V simulated engine blades, *Materials Science and Engineering A 325*, pp. 465-477, 2002.

[117] Chen X., Foreign object damage on the leading edge of a thin blade, *Mechanics of Materials 37*, pp. 447–57, 2005.

[118] Frankel P.G., Withers P.J., Preuss M., Wang H.T., Tong J., Rugg D., Residual stress fields after FOD impact on flat and aerofoil-shaped leading edges 55, *Mechanics of Materials 55*, pp. 130-145, 2012.

[119] Boyce B. L., Chen X., Hutchinson J. W., Ritchie R. O., The residual stress state due to a spherical hard-body impact, *Mechanics of Materials 33*, pp. 441-454, 2001.

[120] Ruschau J., Thompson S.R., Nicholas T., High cycle fatigue limit stresses for airfoils subjected to foreign object damage, *International Journal of Fatigue 25*, pp. 955-962, 2003.

[121] Arcieri E.V., Baragetti S., Borzini E., Transition from small to large cracks in Ti-6Al-4V specimens, In: Engineering Conferences International, Stress-Assisted Corrosion Damage V, Hernstein (Austria), 15-20 July 2018.

[122] Baragetti S., Borzini E., Božic Ž., Arcieri E.V., Quasi-static tests on Ti-6Al-4V in inert environments and methanol, In: International Conference on Intregrity and Structural Durability, Dubrovnik (Croatia), 2-5 October 2018.

[123] Baragetti S., Borzini E., Arcieri E. V., Effects of environment and stress concentration factor on Ti-6Al-4V specimens subjected to quasi-static loading, *Procedia Structural Integrity 12*, pp. 173-182, 2018.

[124] Baragetti S., Borzini E., Arcieri E. V., Quasi-static crack propagation in Ti-6Al-4V in inert and aggressive media, *Corrosion Reviews* 37, pp. 533-538, 2019.

[125] Baragetti S., Borzini E., Božić Ž., Arcieri E.V., Fracture surfaces of Ti-6Al-4V specimens under quasi-static loading in inert and aggressive environments, *Engineering Failure Analysis 103*, pp. 132-143, 2019.

[126] Baragetti S., Borzini E., Arcieri E.V., Fracture surface of a Ti-6Al-4V specimen with EDM notches tested under quasi-static loading in methanol, *Key Engineering Materials 827*, pp. 79-84, 2019.

[127] Veiga C., J.P. Davim, Loureiro A.J.R., Review on machinability of titanium alloys: The process perspective, *Reviews on Advanced Materials Science 34*, pp. 148-164, 2013.

[128] Dassault, Abaqus Manual.

[129] Baragetti S.; Borzini E.; Božic Ž.; Arcieri E.V., Influence of PVD DLC coatings on 7075-T6 aluminum alloy fatigue strength, In: 2nd International Conference on Structural Integrity and Durability, 2-5 October 2018.

[130] Baragetti S.; Borzini E.; Božic Ž., Arcieri E.V., Fracture surfaces of 7075-T6 specimens tested in rotating bending fatigue tests and evaluation of the centrifugal force contribution, In: 3rd International Conference on Structural Integrity and Durability, 4-7 June 2019.

[131] Baragetti S.; Borzini E., Arcieri E.V., Rotating bending fatigue tests on uncoated and DLC coated 7075-T6 aluminum alloy, In: 8th International Conference mechanics and materials in design, Bologna (Italy), 4-6 September 2019.

[132] Arcieri E.V., Baragetti S., Borzini E., Bending fatigue behavior of 7075-alluminm alloy, *Key Engineering Materials 774*, pp. 1-6, 2018.

[133] Baragetti S., Borzini E., Božic Ž., Arcieri E.V., On the fatigue strength of uncoated and DLC coated 7075-T6 aluminum alloy, *Engineering Failure Analysis 102*, pp. 219-225, 2019.

[134] Baragetti S, Božic Ž., Arcieri E.V, Stress and fracture surface analysis of uncoated and coated 7075-T6 specimens under the rotating bending fatigue loading, *Engineering Failure Analysis 112*, 104512, 2020.

[135] Baragetti S., Arcieri E.V., Effects of thin hard film deposition on fatigue strength of AA7075-T6, *Proceedings of the Institution of Mechanical Engineers, Part C: Journal of Mechanical Engineering Science* (online), 2020.

[136] www.matweb.com.

[137] ISO 1143:2010 Standard. Metallic materials — Rotating bar bending fatigue testing, 2010.

[138] Lafer S.p.A., www.lafer.eu.

[139] Baragetti S., Gerosa R., Villa F., Step loading corrosion fatigue testing of 7075-T6 WC/C coated specimens in air and methanol, *Engineering Fracture Mechanics 164*, pp. 106-116, 2016.

[140] Nicholas T., Step loading for very high cycle fatigue, *Fatigue & Fracture of Engineering Materials & Structures 25*, pp. 861-869, 2002.

[141] Baragetti S., Gerosa R., Villa F., Effects of PVD DLC coating on 7075-T6 fatigue strength at high and low number of cycles, *Key Engineering Materials 713*, pp. 50-53, 2016.

[142] Baragetti S., Gerosa R., Villa F., Fatigue behaviour of thin coated Al 7075 alloy with low temperature PVD coatings, *Key Engineering Materials 577-578*, pp. 221-224, 2013.

[143] ISO 12107:2012 Standard. Metallic materials — Fatigue testing — Statistical planning and analysis of data.

[144] Milella P.P., Fatigue and corrosion in metals, *Springer*, 2013.

[145] http://slideplayer.it/slide/2353788/.

[146] Baragetti S., La Vecchia G.M., Terranova A., Fatigue behavior and FEM modeling of thin-coated components, *International Journal of Fatigue 25*, pp. 1229–1238, 2003.

[147] Baragetti S., Gerosa R., Villa F., Fatigue behaviour of DLC coated Al 7075-T6 alloy in an aggressive mixture, *Key Engineering Materials 627*, pp. 81–84, 2015.

[148] Arcieri E.V., Baragetti S., Božić Ž, Stress distribution in 7075-T6 hourglass samples subject to FOD, In: 4th International Conference on Structural Integrity and Durability, Dubrovnik (Croatia), 15-18 September 2020.

[149] Arcieri E.V., Baragetti S., Lavella M., Effects of FOD on fatigue strength of 7075-T6 hourglass specimens, IOP Conference Series: Materials Science and Engineering (submitted).

[150] Arcieri E.V., Baragetti S., Fustinoni M., Lanzini S., Papalia R., Study and modelling of the passenger safety devices of an electric vehicle by finite elements, *Procedia Structural Integrity 8*, pp. 212-219, 2018.

[151] Baragetti S., Arcieri E.V., A new mobile anti-ramming system, ASME International Mechanical Engineering Congress and Exposition, Proceedings (IMECE) 14, Salt Lake City (Utah), 11-14 November 2019.

[152] Baragetti S., Arcieri E.V., Study on a new mobile anti-terror barrier, *Procedia Structural Integrity 24*, pp. 91-100, 2019.

[153] Baragetti S., Arcieri E.V., Study of impact phenomena for the design of a mobile anti-terror barrier: Experiments and finite element analyses, *Engineering Failure Analysis 113*, 104564, 2020.

[154] Johnson K.L., Contact mechanics (Cambridge University Press), 1985.

[155] Lavella M., Partial-gross slip fretting transition of martensitic stainless steels, *Tribology International 146*, 106163, 2020.

[156] Lavella M., Botto D., Fretting fatigue analysis of additively manufactured blade root made of intermetallic Ti-48Al-2Cr-2Nb alloy at high temperature, *Materials 11*, pp. 1052-1063, 2018.

[157] Botto D., Lavella M., A numerical method to solve the normal and tangential contact problem of elastic bodie, *Wear 330-331*, pp. 629-635, 2015.